Study of the dynamics of barred early type galaxies via numerical simulations

Pierre-Yves Lablanche

Université Claude Bernard Lyon 1

Thèse de doctorat

Spécialité : Astrophysique

pour obtenir le titre de

Docteur ès sciences

de l'Université Claude Bernard Lyon 1

Présentée par

Lablanche Pierre-Yves

Study of the dynamics of barred early type galaxies via numerical simulations

Soutenue publiquement le 4 Avril 2012

Jury :

President :	Roland BACON	Observatoire de Lyon
Reviewers :	Daniel PFENNIGER	Observatoire de Genève
	Hervé WOZNIAK	Obs. Astronomique de Strasbourg
Examiners :	Frédéric BOURNAUD	CEA (Saclay)
	Thomas BUCHERT	Observatoire de Lyon
Advisor :	Eric EMSELLEM	Obs. de Lyon & ESO (Garching bei München)

Résumé

Depuis la célèbre classification d'Edwin Hubble dans les années 30, il est coutume de définir une galaxie comme appartenant soit au groupe des galaxies dites de type *tardif* (late-type galaxies abrégé LTGs) soit à celui des galaxies dites de type *précoce* (early-type galaxies ou ETGs). La famille des LTGs est principalement composée de galaxies spirales (S) quand la famille des ETGs regroupe les galaxies lenticulaires (S0) et elliptiques (E). L'étude morphologique de ces galaxies a révélé qu'environ 60% des LTGs et 45% des S0 présentent une barre. Par ailleurs, il a été montré que dans l'Univers local les galaxies pouvaient être séparées en deux grands ensembles : le *nuage bleu* composé majoritairement de LTGs et la *séquence rouge* peuplée principalement par les ETGs. Plusieurs mécanismes sont à l'origine de cette distribution et l'évolution séculaire en est évidemment un point majeur. Un nombre important de recherches ont montré l'importance des barres sur la dynamique et l'évolution d'une galaxie. Le but de ma thèse est d'étudier à quel point la formation d'une barre et l'évolution qui s'ensuit influe sur l'évolution des ETGs. Pour ce faire j'ai réalisé des simulations à N-corps de galaxies barrées (et non barrées) qui m'a permis détudier les points suivants.

Je me suis tout d'abord penché sur l'impact de la présence d'une barre dans une galaxie sur une modélisation de cette dernière par un modèle supposant une ditribution de masse axisymmétrique. Ce genre de modélisation permettant de déterminer le rapport masse/luminosité M/L et donc la masse d'une galaxie observée mais également son inclinaison et son anisotropie, il est important d'estimer l'impact de la présence d'une barre sur ces paramètres. J'ai donc montré qu'en fonction de l'inclinaison de la galaxie et de la position de la barre par rapport à l'observateur, le rapport M/L était très souvent surestimé avec des erreurs allant jusqu'à 25%. La taille et la force de la barre sont également apparus comme des facteurs importants mais une étude plus approfondie s'imposerait afin de quantifier ce résultat.

D'autre part, je me suis intéressé à l'impact d'une barre sur la distribution de masse et de métaux dans une galaxie lenticulaire. J'ai tout d'abord confirmé que la présence d'une barre, de part son influence sur la dynamique d'un système, applatissait les gradients de métallicité. De plus j'ai montré que le degrés d'aplatissement ainsi que la position des zones affectées peuvent être directement mis en relation avec la structure de la barre et notament avec la localisation des résonances dynamiques. Néanmoins l'influence purement dynamique d'une barre n'explique pas à elle seule les gradients d'âges et de métallicité observés. L'étude de l'influence d'un potentiel gravitationnel barré sur la dynamique du gaz et donc sur la formation stellaire est donc également à prendre un compte. Cela fait l'objet des dernières simulations produites qui permettront de mieux comprendre l'influence global d'une barre sur l'évolution séculaire des galaxies de type précoce.

Abstract

Since the 30's and Edwin Hubble's famous classification, galaxies are usually separated in two groups : the late-type galaxies (LTGs) and the early-type galaxies (ETGs). The LTGs family is mainly made of spiral galaxies (S) while the ETGs family is composed of elliptical (E) and lenticular (S0) galaxies. A morphological study of all these galaxies revealed that around 60% of LTGs and 45% of S0 present a bar. It has also been shown that, in the local Universe, galaxies fall into two big groups : the *blue cloud* mostly populated by LTGs and the *red sequence* mainly made of ETGs. Several mechanisms are responsible for this distribution and the secular evolution is obviously an important one to examine, sepcially in the context of bars, as an important number of studies showed the importance of bars in the dynamics and evolution of a galaxy.

The goal of my thesis is to study the importance of the formation and ensued bar-driven evolution influence on ETGs evolution. In that context, I have performed N-body simulations of barred (and unbarred) galaxies in order to investigate the following issues.

First of all, I focused on the influence of a bar in a galaxy when modelling it with a dynamical model assuming an axisymmetric mass distribution. As these kinds of models allow to determine the mass-to-light ratio M/L, thus the dynamical mass of an observed galaxy, but also its inclination and its anisotropy, it is important to evalute the consequence of the presence of a bar on these parameters. I have shown that, depending on the galaxy inclination and the bar position angle, M/L is most of the time biased and overestimated, and this can be up to 25%. The size and strength of the bar also seem to be important factors but a deeper study has to be done to quantify this preliminary result.

In a second step, I have studied the role of bars on the mass and metallicity redistributions in a lenticular galaxy. I confirmed that the presence of a bar, due to its influence on its host system dynamics, flattens pre-existing metallicity gradients. Moreover, I showed that the degree of flattening and the position of affected regions are directly correlated with the bar structure and the location of the dynamical resonances. Nonetheless, this dynamical effect cannot explain the variety of observed ages and metallicity gradients. The consequences of a barred gravitational potential on the gas dynamics and the stellar formation should therefore be investigated. This is the topic of the last set of numerical simulations produced which will allow to better understand the global influence a bar has on the secular evolution of ETGs.

Contents

Chapter 1

Introduction

1.1 Context

1.1.1 Galaxies

In 1755, Immanuel Kant, in his book named *General History of Nature and Theory of the Heavens* (*Allgemeine Naturgeschichte und Theorie des Himmels*), laid out the hypothesis of the existence of vast systems composed of stars rotating under the influence of the gravitational force much bigger than the solar system. He named them *Island Universes* and suggested that it could be these diffuse object named *nebulae* one can see on the celestial vault. Kant also claimed that the Milky Way is one of these *Island Universe* seen from inside. Nineteen years later, in 1774, Charles Messier (with his assistant Mechain) built a catalog of 45 *nebulae* present in the night sky (extended to 103 in 1781) in order not to mistake them for comets. But the resolution of his instrument did not allow him to distinguish galaxies from diffuse nebulae, planetary nebulae or globular clusters. With his superior telescope William Herschel observed many more diffuse objects but separated star clusters and *nebulae*. He found about 2500 new objects published in three deep-sky catalogs (see Herschel, 1786, 1789, 1802).

The continuous progress of technology, with e.g. the creation of more powerful observational facilities like the Hooker telescope allowed Edwin Hubble from 1924 to measure the distance of these *nebulae* and to conclude that they are mostly extragalactic objects much further away than the known limits of the Milky Way (Hubble, 1926). Based on the one-color images of the objects he studied Hubble also set up in 1936 a classification of galaxies (Hubble, 1936), the well known Hubble Tuning Fork (see figure 1.1).

In the Hubble classification, galaxies fall into two categories :

- Elliptical galaxies (E): spheroidal systems which are optically red system, contains little or no gas, and are assumed to be made of old stars.

- Spiral Galaxies (S): showing a bulge and disc structure with an important amount of gas and dust. They most of the time host an important star formation activity giving an optical blue color to the system. These galaxies can also host a bar in their inner regions (noted SB in this case).

Lenticular galaxies (S0) are positioned in this classification in-between the two aforementioned categories and are sometimes considered as *dead spirals* because they generally present a bulge+disc

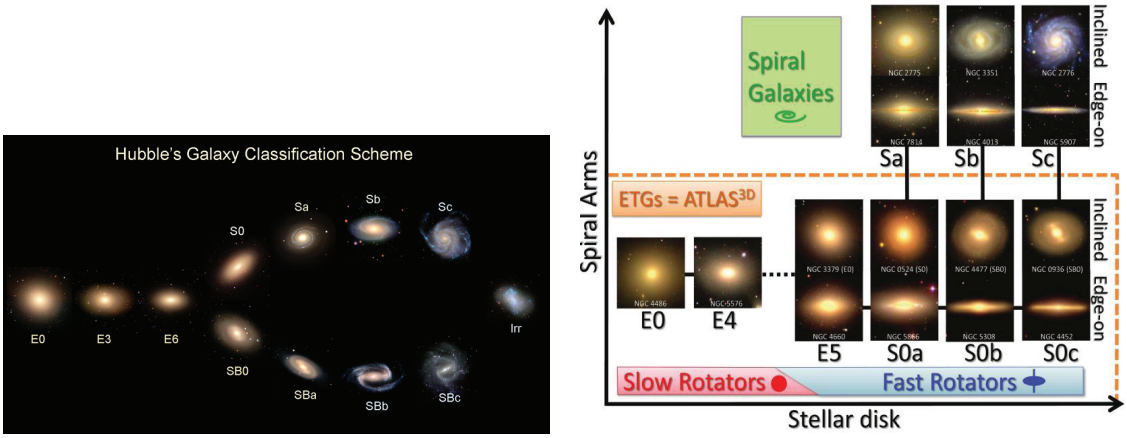

Figure 1.1: The Hubble classification (left) and the classification introduced in Cappellari et al. (2011b) (right). Hubble only classified galaxies according to their appearance while the second classification uses the specific angular momentum λ_R (Emsellem et al., 2007) to revised the classification of ETGs. This latter category is then separated in fast and slow rotators if $\lambda_{Re} > 0.31\sqrt{\epsilon}$ or $\lambda_{Re} < 0.31\sqrt{\epsilon}$ respectively, with ϵ the ellipticity at Re.

structure but without spiral arms and little or no gas and most of the time no star formation. Like spiral galaxies, lenticulars can have a stellar bar in their inner regions (denoted S0B). The Hubble system as we know it nowadays was detailed in Sandage (1961).
Since Hubble, other classifications have been proposed using different criteria (e.g. de Vaucouleurs, 1959; van den Bergh, 1960; Kormendy & Bender, 1999; Cappellari et al., 2011b).

Some decades ago, it was thought that galaxies naturally evolve from elliptical to spiral which led to label ellipticals and lenticulars as *early-type* galaxies (hereafter ETGs) and spirals as *late-type* galaxies (hereafter LTGs). Nevertheless, studies over the last decades demonstrated that galaxies formation and evolution is much more complex, and it is more than ever a matter of debate. Actually the evolution of a galaxy can be influenced by many different processes.

The stellar formation is obviously an important internal factor of a galaxy evolution as it designs its stellar content. Through recycling it also dictates the chemical evolution of a galaxy. The star formation rate and location in a system is strongly driven by the dynamics of the system. See Bruce G. Elmegreen lectures (Elmegreen, 2011a,b,c,d,e) and references therein for a good review on star formation in local galaxies.
Interactions or mergers are also important process in any galaxy evolution history. The structure of a merger remnant is mainly driven by the mass ratio between the progenitors. From major mergers which are expected to produce massive elliptical galaxies (Naab & Burkert, 2003; Bournaud et al., 2005a; Naab et al., 2006; Cox et al., 2006a) to minor mergers which only disrupt the structure of the main progenitor (Villalobos & Helmi, 2008; Moster et al., 2010).
Apart from these external processes a galaxy has a *secular* evolution. Naturally, an isolated galaxy would consume its gas by creating stars, young ones "painting" the galaxy in blue. At this stage the galaxy falls in the late-type category. Then massive blue stars die and only an old red population remains, bringing the galaxy toward the early-type category. In the meantime a bar can form because of instabilities in the disk. But due to gas inflows along the bar and the growth of the

central mass concentration (CMC) the bar can be weaken or destroyed. Then if there is enough gas left or accreted the disk can experience another bar instability period. All previous bar-related phenomena mentioned are detailed in the next section. Bar is a very important motor of secular evolution (see e.g. Knapen, 2010; Combes, 2008, 2011).
It has also been suggested that evolution of galaxies is dominated by external processes at early times and by secular evolution later on (Kormendy & Kennicutt, 2004, which also gives a review on internal secular evolution processes).

To summarize, galaxies are not expected during their life to only move from one side of the Hubble classification to the other.
Their path through any galaxy classification depends on their dynamics and environment and is more chomplex than originally suggested.

1.1.2 Using galaxies in the local Universe as *fossil records*

All the processes previously mentioned lead to the variety of galaxies we can see in the nearby universe. That is why galaxies in the local universe can be viewed as *fossil records*. Nowadays, state-of-the-art observing facilities, such as the HST or the VLT for instance, allow to probe in details galaxies properties up to redshift $z \sim 1$. Beyond this redshift, instruments are unable to reveal any structural and dynamical details. All observations can be viewed as clues to understand the formation and evolution history of galaxies. Listing all projects built over the last decades to collect data at various wavelengths for a galaxy or a sample of galaxies would need much more than just a thesis. Such studies have already allowed to constrain scenarios about the formation and evolution of galaxies. For instance , the emergence of integral field spectrographs, such as *SAURON* (Bacon et al., 2001), have allowed to probe the dynamics of nearby galaxies. Combined with observations at other wavelengths the *SAURON* project reviewed the classical view of ETGs (de Zeeuw et al., 2002).

In addition to the enormous observational work, computational facilities have opened a new approach in astrophysics. Indeed, instead of trying to infer what happened solely from observational clues, we can nowadays simulate the formation and/or evolution of many different structures at very different scales (from a piece of the Universe to dust in planetary disks). I strongly wish to highlight here the full complementarity of these two approaches. Observations allow to set up constraints in simulations in terms of implemented physical processes (e.g. star formation) or initial conditions. These simulations can then be used to better understand underlaying mechanisms in our universe and sometimes provide guidelines for observers. Although the work presented here is based on N-body simulations of galaxies, this statement of complementarity has been a driver all along my thesis.

1.1.3 Blue cloud, red sequence and green valley - the ATLAS^{3D}project

Recently, the advent of large surveys observation campaigns allowed the investigation of morphology-color relations. In Strateva et al. (2001) and Baldry et al. (2004a) the authors showed that when placing observed galaxies in a color-magnitude diagram a clear bimodal distribution takes shape (see Figure 1.2). In the latter figure we can distinguish two concentrations of galaxies named the *blue cloud* and the *red sequence* and an under-populated region in between called the *green valley*. It has been shown that the *blue cloud* is mostly composed of LTGs while the *red sequence* is mostly

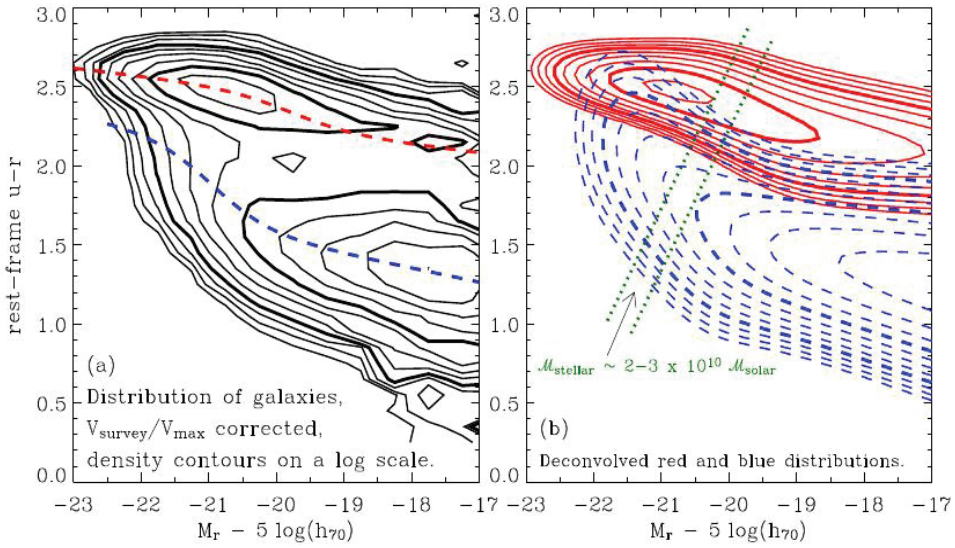

Figure 1.2: The Bimodal distribution of local galaxies in a color (U-R) magnitude diagram as presented in Baldry et al. (2004b). The left panel present the global distribution of galaxies, the solid lines representing isodensities logarithmically spaced and the dashed ones the color-magnitude relation of the red and blue sequence. The right panel shows the decomposition in two distinct populations of the distribution of galaxies. The green dot lines give an indication of the location of the 2.10^{10} to 3.10^{10} solar masses galaxies.

made of ETGs. Studies from Bell et al. (2004) and Faber et al. (2007) showed that this dichotomous distribution can be traced up to redshift unity.

Baldry et al. (2004b) conclude from this bimodal distribution that the two populations were built from two different processes. Moreover, galaxies must move quickly from one population to the other. The fact that most massive galaxies are in the *red sequence* led to the conclusion that galactic mergers can be a key mechanism in the building of the bimodal distribution. Further investigations are obviously needed to fully understand all processes responsible for this observation.

The ATLAS^{3D}project was designed as produce a significant effort towards the understanding of the building of the *red sequence* (see Cappellari et al., 2011a). This is meant to be done by gathering high quality data at various wavelengths and theoretical studies including state of the art cosmological simulations, semi-analytical model and N-body simulations. This project is the natural continuation of the *SAURON* project previously mentioned. The present thesis and work are fully part of the ATLAS^{3D}project and focus on the influence of bars on the dynamics of early-type galaxies.

1.2 Bars in galaxies

1.2.1 Bars are common features

It is observed that at redshift $z = 0$ up to $\sim 60\%$ of LTGs are barred (Eskridge et al., 2000; Menéndez-Delmestre et al., 2007; Marinova & Jogee, 2007) and this fraction seems to be constant at least up to redshift unity (Jogee et al., 2004). Some recent studies have found that this fraction is little or not affected by the environment (Aguerri et al., 2009; Barazza et al., 2009; Li et al., 2009). In the ATLAS^{3D}sample, 65 galaxies out of the 260 present clear photometric evidence of a bar structure, which represents $\sim 30\%$ of the full sample (Krajnović et al., 2011). Actually if in this sample we consider galaxies with a de Vaucouleurs type between -3 and 0 the fraction of barred S0 increases up to $\sim 45\%$ which is in good agreement with recent near-infrared surveys (Laurikainen et al., 2009). These 65 barred ETGs are divided in 35 bar and 30 bar+ring galaxies.

A full range of bars shape and strength can be observed, from oval distortions to major features. It is then more a matter of choice to determine whether a galaxy is barred or not. The fact that bars are so common is not surprising considering previous studies on bar instabilities in disk galaxies. Work based on N-body simulations found that stellar disks are easily subject to large-scale instabilities such as bar-forming ones (e.g. Miller et al., 1970; Hohl, 1971; Zang & Hohl, 1978; Combes & Sanders, 1981; Sellwood, 1981; Athanassoula & Sellwood, 1986; Khoperskov et al., 2007; Dubinski et al., 2009) and this is confirmed by linear stability analysis (e.g. Kalnajs, 1978; Aoki et al., 1979; Toomre, 1981; Sawamura, 1988; Vauterin & Dejonghe, 1996; Pichon & Cannon, 1997; Korchagin et al., 2005; Polyachenko, 2005; Jalali, 2007).

The classic view is that galactic bars form from instability in a disk. The most probable mechanism for the bar instability is based on the *density waves theory* (Lin & Shu, 1964, 1966; Toomre, 1981).

1.2.2 The nature of bars

The density waves theory

Once astronomers were able to observe galaxy morphology they were striked by the amount of galaxies presenting spiral arms (more than 60% as reported in the previous section). The first suggested explanations were a rigid rotation or a differential rotation (such as the one observe when milk is added to cup of tea and the liquid is stired). The rigid rotation hypothesis was quickly discarded because it is in contradiction with observations and laws of physics. The differential rotation, though tempting, would dissolve spiral arms in only a few rotations and therefore can not explain the number of spiral galaxies observed. This issue is also known as the *winding problem*. For a while spiral arms were also thought to arise from the interaction of interstellar gas and a magnetic field. However, interstellar magnetic fields are too weak (Beck et al., 1996) to play a role in the formation of spiral arms although it may help the formation of structures at smaller scales such as cloud complexes (Basu et al., 1997), spurs (Kim & Ostriker, 2002) and nuclear rings (Beck et al., 1999).

During the 60's Lindblad suggested that spiral arms are *density waves*, meaning that they are regions of enhanced density such as waves propagating over the ocean. Lin & Shu (1964) and Lin & Shu (1966) developed this idea which is nowadays commonly accepted (see Pasha, 2004a,b, for a more detailed review on the history of this theory). Although they first thought that the spiral is stationary with a very well-defined *pattern speed* Ω_p (this assumption was later proved not accurate)

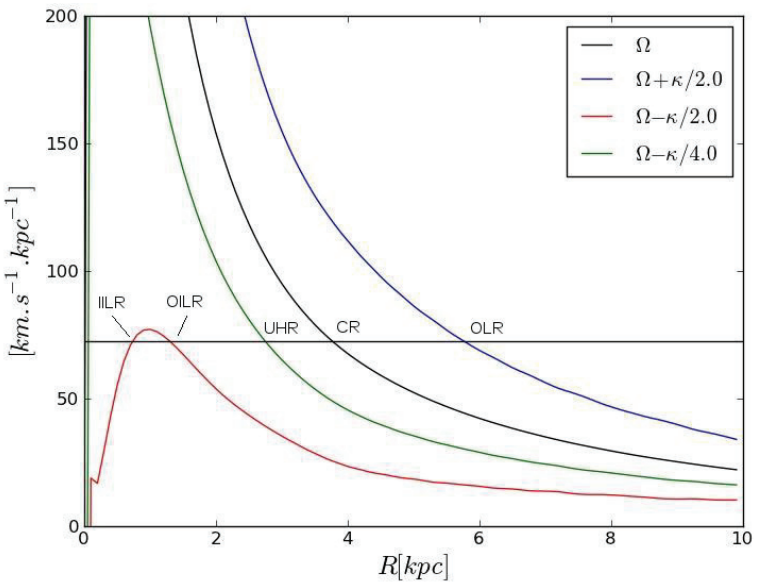

Figure 1.3: Example of the location of Lindblad resonances computed from a model of barred galaxy. The horizontal black line represent the pattern speed of the bar Ω_p. The x axis gives the distance from the galaxy center.

they introduced a new frame which led to predictions successfully compared to observations. Independently from this study spiral arms fall into two categories:

- Leading arm : The arm point in the direction of the rotation of the stars in the galaxy
- Trailing arm : The arm point in the direction opposite to the rotation of the stars in the galaxy

Toomre (1981) suggested that bars are the result of the superposition of a trailing and a leading density waves according to the following mechanism : *A leading disturbance unwinds and is swing amplified into a short trailing disturbance, which propagates through the disk center and emerges as a short leading disturbance, which then unwinds and is amplified further* (Binney & Tremaine, 2008). An important point is that unlike spiral arms, bars do have a well defined pattern peed Ω_p.

Lindblad resonances

At zeroth order, the trajectories of stars in a disk plane can be considered as circular, with the circular frequency $\Omega^2(r) = \frac{1}{r}\frac{\partial \Phi}{\partial r}$ where $\Phi(R, z)$ is the potential in cylindrical coordinates. To first approximation we can assume that orbits are deviations from circular orbits. The movement of a star is then defined by the superposition to the circular trajectory of two independent oscillation movements defined by the epicyclic horizontal and vertical frequencies, κ and ν respectively. This is the *epicyclic approximation*, with κ is given by :

$$\kappa^2 = r\frac{\mathrm{d}\Omega^2}{\mathrm{d}r} + 4\Omega^2 \tag{1.1}$$

Generally the resulting trajectories draw a dense rosette in the equatorial plane except when $\kappa/\Omega = m$ with m an integer. In this latter case orbits are closed. The presence of spiral arms or a bar with a well defined pattern speed Ω_p can be considered as a disturbance on the axisymmetric potential. In a rotating frame with angular frequency Ω_p the angular frequency of orbits is $\Omega - \Omega_p$ and their morphology is then described by $\kappa/(\Omega - \Omega_p)$. Then regions of *resonances* exist between the natural frequencies of the system and the frequency of the perturbation where $\kappa/(\Omega - \Omega_p) = m$. These are the **Lindblad resonances** when $m = \pm 2$.
The main resonances regions are the following :

- $\Omega_p = \Omega - \kappa/2$: **Inner Lindblad Resonance** (ILR). Depending on Ω_p it can exist 0,1 or 2 ILR. In the latter case we distinguish the Inner Inner Lindblad Resonance (IILR) and the Outer Inner Lindblad Resonance (OILR) (see Fig 1.3).
- $\Omega_p = \Omega - \kappa/4$: **Ultra Harmonic Resonance** (UHR).
- $\Omega_p = \Omega$: **Corotation** (CR).
- $\Omega_p = \Omega + \kappa/2$: **Outer Lindblad Resonance** (OLR).

An example of the location of Lindblad resonances computed from a model of a barred galaxy is given in Fig 1.3 The presence of these resonances play an important role in the evolution of a barred galaxy. They strongly influence the dynamics of the system and the location of star formation is sensitive to the presence of such resonances.

Orbits in a bar

Although bars are typically triaxial 3D systems, their structure can be more easily understood in a 2D in-plane view. The effective gravitational potential in the rotating frame of the bar is given by :

$$\Phi_{eff} = \Phi - \frac{1}{2}\Omega_p^2 r^2 \tag{1.2}$$

where Φ is the potential in an inertial frame. The energy of a particle in this frame is given by the *Jacobi integral*:

$$E_J = \frac{1}{2}v^2 + \Phi_{eff} = \frac{1}{2}v^2 + \Phi - \frac{1}{2}\Omega_p^2 r^2 \tag{1.3}$$

Fig 1.4 shows the equipotential in the rotating frame of a bar. In this potential there are five stationary Lagrangian points. L_3 is the central minimum, L_4 and L_5 are maxima (and the only stable points) and L_1 and L_2 are saddle points. The points L_1, L_2, L_4 and L_5 define an annular zone named the corotation zone as it corresponds to the CR resonance.

Inside this potential the orbits of bars can be derived analytically (Contopoulos & Papayannopoulos, 1980). The main periodic orbit families are :

- x_1 orbits family. They are orbits elongated parallel to the bar major-axis and therefore constitute its "backbone". They are located inside the CR or between the ILR and the CR.
- x_2 orbits family. They are located only between IILR and OILR. Contrarily to x_1 orbits they are elongated perpendicular to the bar major-axis and thus their presence tends to weaken or destroy the bar. Nonetheless the existence of two ILRs does not necessarily mean that x_2 orbits are present.

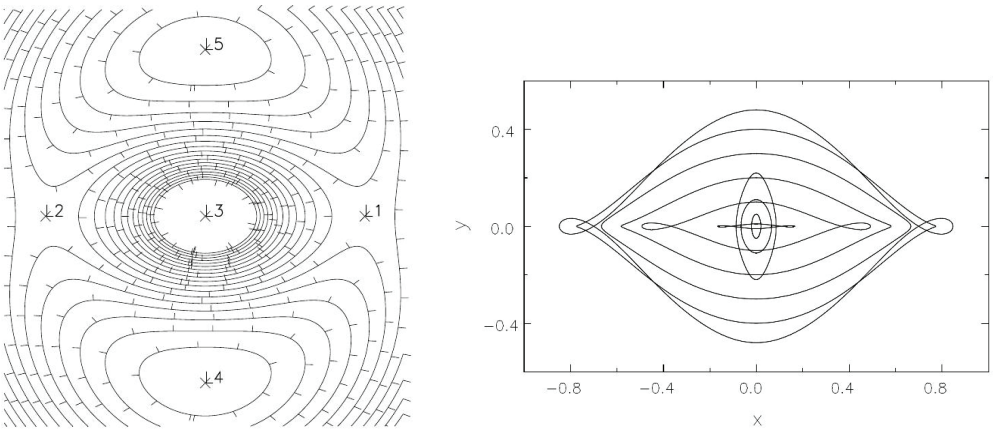

Figure 1.4: Logarithmic equipotential of a barred potential (left) and the x_1 and x_2 families of orbits inside this potential (right). The bar is oriented horizontally in both figures. (The left figure is extracted from Herve Wozniak DEA course while the left one is extracted from Sellwood (2010))

- outside CR : inside OLR orbits are perpendicular to the bar major axis and parallel again outside OLR. These orbits are important for the formation of rings at the OLR.

This brief overview of orbits in bars gives some clues to understand the orbital structure of bars. The fact that stars also have a vertical oscillation introduce the existence of other orbit families with their specific vertical resonances (see Pfenniger & Friedli, 1991; Skokos et al., 2002). These orbits are the building block of boxy or peanut-shape bulge structures (Combes & Sanders, 1981; Pfenniger, 1984; Combes et al., 1990; Patsis et al., 2002; Wozniak & Michel-Dansac, 2009).

1.2.3 Past studies on bars

A huge amount of observational, theoretical and numerical studies of galactic bars have been done over the last decades and it is nowadays admitted that they have an important role in disk galaxy evolution (see Sellwood & Wilkinson, 1993; Kormendy & Kennicutt, 2004; Sellwood, 2010, for reviews).

Theoretical (e.g. Binney & Tremaine, 2008; Sellwood & Wilkinson, 1993; Lynden-Bell, 1979, 1996) and numerical studies (e.g. Sellwood, 1981; Sparke & Sellwood, 1987; Pfenniger & Friedli, 1991; Athanassoula, 2003) show that bars can efficiently redistribute mass and angular momentum in a disk (see Binney, 2012, for a review on the dynamics of secular evolution). This transfer tends to grow bars as the orbits get more elongated. Subsequently the pattern speed decrease as the bar lengthens.

The radial mixing and diffusion processes in a barred galaxy have been less extensively studied (e.g. Pfenniger, 1986; Sellwood & Binney, 2002; Brunetti et al., 2011) although such non axisymmetric feature influence the diffusion especially at the corotation region.

Several studies (both observational and numerical) have been designed to investigate the mutual influence between bars and gas and star formation activity (e.g. Schwarz, 1981; Friedli et al., 1994; Ellison et al., 2011). It is admitted that bars tend to efficiently drive gas towards the most inner hundred parsecs triggering star formation (Friedli et al., 1994). The presence of a bar is expected to

globaly increase the star formation rate (see e.g. Hummel et al., 1990; Hawarden et al., 1996; Huang et al., 1996). However, the exchange of angular momentum tends to weaken the bar (sometimes to its destruction) and over a Hubble time a galaxy may have experimented several bar episodes (see Bournaud & Combes, 2002). The feeding of some central starbusts by this gas inflow have already been observed (Hunt & Malkan, 1999; Jogee et al., 2005; Hao et al., 2009).

Subsequent metallicity enrichment and distribution have been also studied and it has been found that abundance gradient are often flatter in barred galaxies (e.g. Vila-Costas & Edmunds, 1992; Friedli et al., 1994). Nonetheless some observational studies have found an important variety of metallicity gradients within bars (e.g. Oey & Kennicutt, 1993; Considère et al., 2000; Sánchez-Blázquez et al., 2011).

Many other studied than the ones previously cited have been done on bars. Here I only focused on those related to the work presented in this thesis.

1.3 This Thesis

The purpose of the present thesis is to investigate the impact of a bar driven evolution on the structure and dynamics of galaxies observed in the *red sequence* at $z = 0$. I focused on the study of the evolution of isolated barred early-type galaxies and the signature that one can find in various observations by simulating S0B (and S0) with N-body models.

In chapter 2, I present the different simulation codes used during my thesis. I give details on their main characteristics and their pros and cons. A description of the simulation strategy is also given.

Chapter 3 deals with the modeling of barred ETGs with axisymmetric modeling method. We investigate how the presence of a bar influence the recovery of dynamical parameters through such modeling method. We show that a systematic error is made on the recovered M/L depending on the inclination of the galaxy and the position angle of the bar. Moreover the length of the bar appears to be an important factor even though a deeper study is required to clearly answer this question.

In chapter 4, I detail the study done on the bar driven evolution of isolated galaxies and its consequence on mass and metallicity redistribution, star formation and the possible signatures in observations. We first confirm that a bar efficiently flattens a metallicity gradient just by modifying the dynamics of a galaxy. In addition we have found that the degree of flattening and the positions of affected regions can be correlated with the dynamical resonances. Nonetheless, a bar-driven dynamical evolution does not seem to be able to explain the diversity of gradients observed and thus we also investigated the influence of a bar on the location and history of star formation. This last point would require further developements to reach a better understanding of the global bar influence on secular evolution.

Conclusion and clues for future work are given in chapter 5.

Chapter 2

Numerical simulations

2.1 Introduction

The light-bulb experiment of Holmberg (1941) can be considered as the first N-body simulation of gravitational systems. In this laboratory experiment Holmberg used 74 light-bulbs to represent mass elements, the light intensity of each ligh-bulb was proportional to mass. The gravitation was replaced by light and gravitational forces were calculated according to the total light received by an element. In 1960, von Hoerner (1960) performed the first computer calculation in which a system was modelled with $N = 16$ particles. A few years later, Aarseth (1963) increased the number of particles in his simulations of clusters up to $N = 100$. Since these pioneering works the number of particles has increased every two years by nearly a factor two. The latest simulations have reached the impressive number of $N \backsimeq 10^{10}$ particles (Springel et al., 2005; Teyssier et al., 2009).

The advent of this powerful tool, significantly improved our knowledge in many fields of astrophysics. It has been widely used from cosmological to planetary scales and many computational techniques and dedicated codes have been developped over the last decades.
In the present thesis, the sudy is focused on the secular evolution of isolated galaxies which can be considered as collisionless gravitational systems. N-body models were run with three different codes during my thesis : **PMSPH**, **GADGET-2** and a **PM - sticky particle** simulation code.

Section 2.2 describes the basic equations governing collisionless simulations codes and the main existing computation methods. In a second section (2.3), I describe the specifics of *PMSPH*, *GADGET-2* and the *PM - sticky particle* codes. The simulation strategy adopted during the thesis is given in section 2.4.

2.2 Generality

2.2.1 Fundamental equations of gravitational systems

In a system of typical size R made of N particles of radius r the cross section of a direct collision between 2 particles is $\sigma = 4\pi r^2$. Assuming the mean density to be $n = 3N/(4\pi R^3)$ the mean free path can then be expressed as :

$$L \approx \frac{1}{n\sigma} = \frac{4\pi R^3}{3N4\pi r^2} \tag{2.1}$$

Early-type galaxies are roughly made of 10^{10} to 10^{12} stars (let me assume $N = 10^{11}$ for the following computations) and have a typical radius $R \sim 10$kpc. Stars can be assumed to all have the

same solar radius $r = R_\odot \approx 2.2.10^{-11}$ kpc. This give $L \sim 5.10^{11} \cdot R$. The mean free path is then much bigger than the system typical size, in other words direct collisions occured on average every 500 billion crossing.
Now considering the *crossing time* $t_{cross} \sim R/v$, with v the typical speed of a particle in the system (we can assume $v \sim 100$ km.s^{-1} or $v \sim 100$ kpc.Gyr^{-1} in our case), the collision time is given by $t_{coll} = L.t_{cross}/R \approx 5.10^{19}$ years. As the universe is estimated to be 10^{10} years, direct encounters happen every 5.10^9 times the age of the universe.
In addition to the previous calculation it is important to estimate the *relaxation time* which represents the time after which the deviation from the original kinetic energy of a test particle due to two-body encounters is of the order of its initial kinetic energy. In mathematical words t_{relax} is the time after which $\Delta v^2 \sim v^2$ for a particle. Details of the computation of Δv^2 can be found in section 1.2.1 of Binney & Tremaine (2008). In a gravitational field it is shown that :

$$\frac{\Delta v^2}{v^2} \approx \frac{8\ln(N)}{N} \tag{2.2}$$

Every crossings v^2 deviates by Δv^2. Then if n_{relax} is the number of crossings to change the kinetic energy by the order of itself then :

$$n_{relax} = \frac{v^2}{\Delta v^2} = \frac{N}{8\ln(N)} \tag{2.3}$$

The *relaxation time* can be defined as $t_{relax} = n_{relax}.t_{cross}$ and then can be written as

$$t_{relax} \simeq \frac{0.1N}{\ln(N)}.t_{cross} \tag{2.4}$$

A quick calculation gives for $N = 10^{11}$, $t_{relax} = t_{cross}.10^9 \simeq 1.10^{17}$ years, which is much larger than the Hubble time.

The consequence of the previous calculations is that a galaxy can be considered as a collisionless system in which a particle can be viewed as a point-mass in a smooth gravity field $\Phi(\mathbf{x}, t)$ with $\mathbf{x}$ the position of the particle. The state of such systems is fully described in the phase-space $\{\mathbf{x}, \dot{\mathbf{x}}\}$ by the *distribution function* (DF) $f(\mathbf{x}, \dot{\mathbf{x}}, t)$. This function represents the star density in phase-space and satisfy the *collisionless Boltzmann equation* :

$$\frac{\mathrm{d}f}{\mathrm{d}t} = \frac{\partial f}{\partial t} + \dot{\mathbf{x}} \cdot \frac{\partial f}{\partial \mathbf{x}} - \frac{\partial \Phi}{\partial \mathbf{x}} \cdot \frac{\partial f}{\partial \dot{\mathbf{x}}} = 0 \tag{2.5}$$

This means that the fluid is incompressible in phase-space. The spatial density of the system $\rho(\mathbf{x}, t)$ can be obtained with a simple integration of the DF over $\dot{\mathbf{x}}$

$$\rho(\mathbf{x}, t) = \int f(\mathbf{x}, \dot{\mathbf{x}}, t)\mathrm{d}\dot{\mathbf{x}} \tag{2.6}$$

and the gravitational potential is linked to the spatial density according to the well known *Poisson's equation*

$$\Delta\Phi(\mathbf{x}, t) = 4\pi G\rho(\mathbf{x}, t) \tag{2.7}$$

with G the gravitational constant.

To summarize, galaxies can be viewed as collisionless systems which evolution is governed by

the collisionless Boltzmann equation and the Poisson's equation. So far computers do not allow to model each single star in a galaxy and the number of particles used is lower than the number of stars by several orders of magnitudes. In other words we need computational methods to correctly model the distribution function by N points and reproduce the continuous aspect of gravitational systems.

2.2.2 Computational methods

The aim of N-body simulations is to reproduce the behavior of a gravitational system as accurately as possible. The question is then : how can we reproduce the dynamic of a gravitational system such as a galaxy with fewer particles than its number of stars? Some numerical techniques has been developed to answer this issue. I present here only the main ones.

To compute the evolution of N particles in a system we need to determine the forces applied to each particle. So, as a first approach, a N-body simulation consists of a very simple loop:

- Step 1 : to derive the gravitational force applied on each particle from their current position using a *Poisson solver*.
- Step 2 : to compute the new position of particles after a small time step and go back to step 1.

A brute force approach to compute the gravitational forces in a N-body system, would be to do a direct summation of all the forces applied to a particle. Simulations code based on this direct technique are named PP codes for Particle-Particle computation. The advantage is that this method is accurate, but for a system with N particles this implies to compute $N(N-1)/2$ forces every time step. Then the main issue is that the computational time increases very quickly with N in N^2. So far this method can be reasonably suitable for systems up to $N \sim 10^4$ particles. When modeling larger systems such as galaxies, the computational cost becomes too high and a different method must be adopted.

Besides this direct method, collisionless simulation codes can be divided in two main categories according to the way of computing the gravitational forces : Particle-mesh codes or tree codes. For these two methods the computational cost only increases in $N\ln(N)$ and must therefore be prefered to the PP method when modelling system with $N > 10^5$.

Particle-Mesh codes

In Particle-Mesh (PM) codes the computation of the gravitational forces is done on a grid.
The first step is the **mass assignment**. It consists in assigning the mass of each particle to one or more nearby adjacent grid nodes. Different algorithm exist but an efficient one is the "cloud-in-cell" (CIC) method (see Hockney & Eastwood, 1981). Using this method the mass of a particle is assigned to its 2^D nearest nodes with D the number of dimensions of the grid.
Once the mass has been assigned, the field potential is computed from the mesh-density by applying the *Poisson's equation* in the frequency space using a *Fast Fourier Transform* (FFT). Then forces applied to each particle are extrapolated from this field and the new position and velocities of the particle are computed.

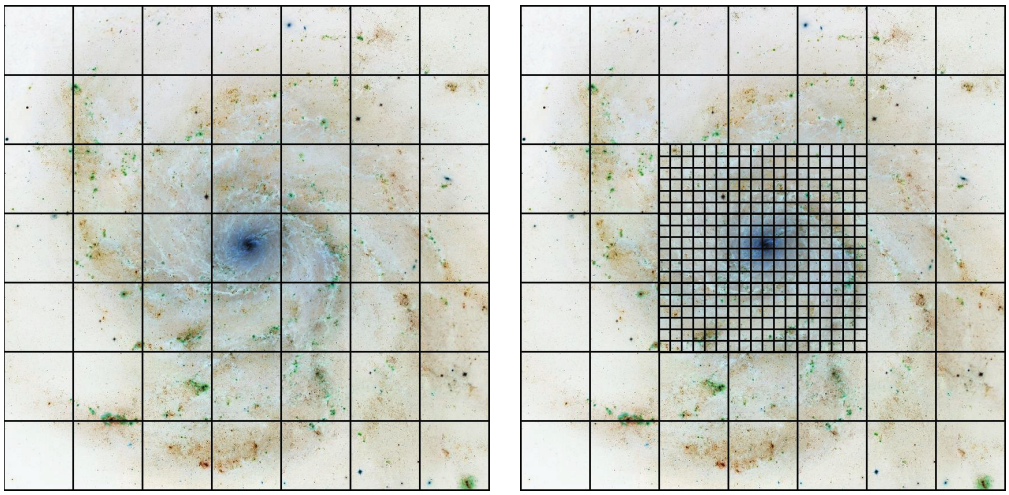

Figure 2.1: These two figure illustrate the grid of a PM simulations code. The left picture represent a fixed single resolution grid while the right one a multi-refinement grid.

PM codes allow to reach a high efficiency in terms of numbers of steps per CPU time step. On the other hand, the resolution level (and the computational speed) is fixed by the grid used and therefore a balance has to be found between the computational cost and the resolution. To overcome this issue some codes using an adaptive multi refinement grid (AMR) have been developed (e.g. Teyssier, 2002) or sometimes with a fixed multi-refinement grid (such as the *PM-sticky particle* code I have used) as shown in Fig 2.1.
Mainly, PM codes are suitable to model the evolution of isolated galaxies although they are also used to study galaxy mergers.

Tree codes

The computation of gravitational forces in a tree code is done with a direct summation for closest particles and by averaging the potential at longer distances. This tree can be set according to the **oct-tree** method introduced by Barnes & Hut (1986). It divides a *root* cube in eight equal cubes with side half of the divided cube. Any sub-division containing more than one particle is again divided in eight cubes. When computing the gravitational force the closest tree region is explored in detail while more distant regions are considered as pseudo-particles gathering groups of particles (see Fig 2.2).
Contrary to PM codes, tree codes do not suffer from the resolution limit in the highest density region but are limited by the softening length. This makes this kind of codes more suitable for high contrast environment simulations (cosmological simulations for instance) or systems without any specific geometry. At the same time, PM codes are expected to be faster than tree codes for the same number of particles.

A number of codes using hybrid computational methods have been developed. For instance Particle-Particle/Particle-Mesh codes (P^3M) (Efstathiou et al., 1985) or tree-code/Particle-Mesh codes (Bode & Ostriker, 2003).

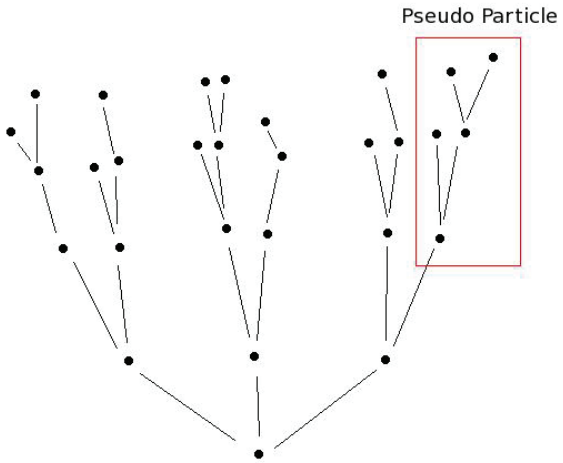

Figure 2.2: Scheme of the tree code computational method. The red box gives an example of what can be considered as a pseudo particle, inside this box particle to particle interactions are not computed. The contribution to the gravitational potential of this pseudo particle is an average of its components contribution.

The time integration of the equation of motion (in both PM and Tree codes) can be done with the *leap-frog* method or the *Runge-Kutta* method.

- Leap-frog : Hut et al. (1995) describe the leap-frog method as a "standard way of integrating the equations of motion of interacting particles whose interactions have no explicit velocity dependence". It is actually simple and efficient. The new position and velocities of a particle after a time-step Δt are given by :

$$\mathbf{x}_{i+1} = \mathbf{x}_i + \dot{\mathbf{x}}_i.\Delta t + \frac{1}{2}\ddot{\mathbf{x}}_i.\Delta t^2 \tag{2.8}$$

$$\dot{\mathbf{x}}_{i+1} = \dot{\mathbf{x}}_i + \frac{1}{2}(\ddot{\mathbf{x}}_i + \ddot{\mathbf{x}}_{i+1}).\Delta t \tag{2.9}$$

  From $\mathbf{x}_i, \dot{\mathbf{x}}_i, \ddot{\mathbf{x}}_i$, using the previous equation, one first has to compute $\mathbf{x}_{i+1}$, then extrapolate $\ddot{\mathbf{x}}_{i+1}$ and finally $\dot{\mathbf{x}}_{i+1}$

- Runge-Kutta : This method is meant to solve problems of the form :

$$\dot{\mathbf{x}} = f(t, \mathbf{x}) \tag{2.10}$$

$$\mathbf{x}(t_0) = \mathbf{x}_0 \tag{2.11}$$

  The numerical approximation of the solution takes the form :

$$\mathbf{x}_{i+1} = \mathbf{x}_i + h\sum_{j=1}^{s} b_j k_j \tag{2.12}$$

$$k_j = f(t_i + c_j h, \mathbf{x}_i + h\sum_{l=1}^{s} a_{jl} k_l) \tag{2.13}$$

The order of the Runge-Kutta method used is given by s. The most common is the fourth order techniques often named RK4.

Both previous integration methods can have fixed or have adaptive time-step.

In the following section we introduce technical specificities of the three simulation codes I have used to perform simulations.

2.3 Simulation codes

2.3.1 GADGET-2

This tree code is fully described in Springel (2005). It is based on the hierarchical multipole expansion method *oct-tree* for the computation of the gravitational forces. The time integration of the equation is done using the leapfrog algorithm. This code is fully parallelized, thus reducing significantly the computational time when using multiple CPUs.
A gas component can be added and is treated using the *Smooth Particles Hydrodynamics* (SPH) method (introduced by Lucy, 1977; Gingold & Monaghan, 1977). This numerical technique mimics the equations of fluids dynamics with a limited number of particles. This can be done by using a kernel estimation technique. Basically the interpolation of a quantity A is given by :

$$A_I(\mathbf{x}) = \int A(\mathbf{x}')W(\mathbf{x}-\mathbf{x}',h)\mathrm{d}\mathbf{x}' \tag{2.14}$$

where W is a given kernel. A *spline* kernel is the most common and is used here :

$$W(x,h) = \frac{8}{\pi h^3}\begin{cases} 1-6(\frac{x}{h})^2+6(\frac{x}{h})^3 & 0 \leqslant \frac{x}{h} \leqslant \frac{1}{2} \\ 2(1-\frac{x}{h})^3 & \frac{1}{2} < \frac{x}{h} \leqslant 1 \\ 0 & \frac{x}{h} > 1 \end{cases} \tag{2.15}$$

Then for instance, for a particle at position $\mathbf{x}_i$, velocities $\mathbf{v}_i$ and mass m_i, the density estimate is given by :

$$\rho_i = \sum_{j=1}^{N} m_j W(|\mathbf{x}_{ij}|, h_i) \tag{2.16}$$

where $\mathbf{x}_{ij} = \mathbf{x}_i - \mathbf{x}_j$.
The smoothing length h is often set such that $W = 0$ at a distance $2h$. In *GADGET-2* h_i is defined for each particle such that :

$$\frac{4\pi}{3}h_i^3\rho_i = N_{sph}\overline{m} \tag{2.17}$$

where ρ_i is the estimated density, N_{sph} is the typical number of smoothing neighbours and $\overline{m}$ is an average particle mass. In other words h_i is chosen such that the mass inside the kernel volume is constant for a given ρ_i. SPH methods fits the global tree-code method and has the same advantage of concentrating computation where the matter is. For an exhaustive review of the method see Monaghan (2005).
The version of the code used in the present work did not include a treatment of the star formation from a gas component. This latter point restricts the use of this code to gas-less simulations in our

case.

Its characteristics made *GADGET-2* very popular code for cosmological simulations but it was also used to study galaxy mergers. An important number of studies has been done with this code (e.g. Springel et al., 2005; Croton et al., 2006; Cox et al., 2006a,b; Hopkins et al., 2006; Naab et al., 2007; Kereš et al., 2009; Hopkins et al., 2009; Navarro et al., 2010).

2.3.2 PMSPH

The Particle-Mesh Smooth Particle Hydrodynamics (*PMSPH*) code detailed in Pfenniger & Friedli (1993), is a PM code based on a fixed polar grid. This code has been written to mainly study the secular evolution of isolated galaxies. In this code the gravitational forces are computed on a polar grid (R, Θ, z) with a cylindrical central cell. The other cells are linearly spaced in Θ and logarithmically spaced in R. This geometry allows to naturally reach a higher resolution in the central region of the grid where high numbers of stars are expected to lie. Contrarily to cartesian grids, it also implies to regularly recenter the galaxy in the grid if one wants to keep the advantage previously mentioned.

Once particles are placed in the three dimension grid their mass are assigned to the nearest eight mesh points by using the Cloud-in-Cell method. Originally the integration of the equation of motion was done using the leapfrog algorithm. Our version of the code adopted the Runge-Kutta-Fehlberg method. This method (also denoted RK45) allows an adaptive time step.

As in *GADGET-2* gas can be added and is also treated through the SPH method. *PMSPH* used the kernel name W_4 in Monaghan & Lattanzio (1985) which has an interaction length of $2h$.

Contrarily to *GADGET-2*, our version of *PMSPH* includes a star formation treatment. Any region of the galaxy will be subject to star formation if the following two conditions are met (Friedli & Benz, 1995):

$$Q_i^g = \frac{s_i \kappa_i}{\pi G \Sigma_i^g} \leqslant \lambda \tag{2.18}$$

$$T_i = T_{cut} \tag{2.19}$$

where s_i is the local sound speed, κ_i is the generalised epicyclic frequency, Σ_i^g is the gas surface density, T_i is the particle temperature, T_{cut} is a cut-off temperature and $\lambda \approx 1$ is a free parameter. The first condition relies on Toomre's instability criterion for which $\lambda \approx 1.4$ (with $s_i = 6$ km.s^{-1}) but the authors of the code have preferred to keep it as a free parameter. The second criterion is just a condition on the temperature as star formation is expected to occur in cold regions.

The basic version of *PMSPH* have been used in many studies of isolated galaxy evolution e.g. Friedli et al. (1994); Friedli & Benz (1995); Friedli (1996); Martin & Friedli (1997); Wozniak et al. (2003). The revised version of the code we used includes a chemodynamical evolution of the system and has been developed by Michel-Dansac & Wozniak (2004) and applied in e.g. Hernandez et al. (2005); Emsellem et al. (2006); Michel-Dansac & Wozniak (2006); Wozniak & Champavert (2006); Wozniak (2007); Wozniak & Michel-Dansac (2007, 2009). Nonetheless we did not used the chemodynamic evolution module.

Although this code is clearly meant to study secular evolution of an isolated galaxy, some specific issues arose when simulating barred galaxies. In some rare cases we have observed a resonance between the bar pattern speed and the re-centering frequency of the code, resulting in an unrealistic behavior of the bar. Indeed it happened for a few runs that the bar leaves the center of the

galaxy and waltz around it. In these specific cases we just moved to *GADGET-2*. Another issue is that *PMPSH* is mono-core (meaning that it cannot use several CPUs) and therefore run somewhat slower on multi CPUs systems than *GADGET-2*.

2.3.3 PM/sticky particle

This code described in Bournaud & Combes (2002) is based on a fixed multi-refinement cartesian grid. More precisely, the grid offers two levels of refinement from a primary grid. As for *PMSPH* the mass assignment is done with a cloud-in-cell method but the time integration is done with the leap-frog method.
This *PM/sticky particle* code is compiled on a vectorised machine and takes full advantage of this architecture. In other words, a simulation that would have lasted for months with a mono-core code can be done in tens of hours on a vectorised computer.
A sticky-particle numerical method has been implemented to treat a gas component. This method models the inelasticity of cloud-cloud collisions when a fraction of the kinetic energy is lost in heating the gas. This energy is then re-radiated around resulting in the decrease of the relative velocity of the neighboring gas particles. The sticky particle technique allows to treat from 10 to 100 more particles than SPH for the same computational time.
In the present code the star formation mechanism follows Jungwiert et al. (2001). It is assumed to follow the Schmidt law (Schmidt, 1959) : locally the star formation rate (SFR) is proportional to a power of the surface density of gas Σ_g^n:

$$SFR \propto \Sigma_g^n \text{ with } 1 < n < 2 \tag{2.20}$$

In the code n is fixed to 1.4 based on the observational study of Kennicutt (1998).

Examples of studies based on this code can be found in e.g. Bournaud & Combes (2003); Bournaud et al. (2003); Duc et al. (2004); Bournaud et al. (2005a,b,c, 2007b); Duc & Bournaud (2008); Martig et al. (2009a,b); Bois et al. (2010, 2011) and Lablanche et al. (submitted). The availability of this *PM/sticky particle* code allowed to run high resolution simulations of barred lenticulars with several millions of particles.

2.4 Discussion

2.4.1 Simulation Strategy

The computational cost difference between all the three aforementionned codes have been well exceeded by material constraints.
First, the effective speed of each code obviously depends on the host machine. *PMSPH* and *GADGET-2* are installed on a quad-core machine located at the *Centre de Recherche Astrophysique de Lyon* (CRAL) while the *PM-sticky particle* code is compiled on a much more powerful machine at a CNRS computing center at IDRIS. Thus, for the same number of particles, it was faster to run the simulation with the latter code. At the same time, the computational time is limited for the *PM-sticky particle* code but not for the two other simulation codes. Moreover the machine in Lyon is straight available while job requests are stacked in a waiting queue at IDRIS. Consequently tests simulations with a relatively small number of particles were run with **PMSPH** and **GADGET-2** while "big" simulations with up to 7.10^6 particles were performed at IDRIS.

Code	T_{bar} $[Myr]$	L_{bar} $[kpc]$	axis ratio	Ω_p $[km.s^{-1}.kpc^{-1}]$
GADGET-2	70	1.2	~ 2.8	81.2
PMSPH	75	1.4	~ 3	86.7
PM/sticky	75	1.3	~ 3	85.5

Table 2.1: Table summarizing the properties of the bar model with each simulation code. T_{bar} gives the time of formation of the bar. In the third column L_{bar} is the size of the semi major-axis of the bar and the fourth column gives the axis ratio. Ω_p is the bar pattern speed at T=1Gyr.

To ensure that the dynamics of any model is not significantly affected by the codes used here, I have run simulations on each code with the same initial conditions. These initial conditions consisted in a model of an axisymmetric lenticular galaxy subject to bar instability. The simulated time of evolution was set to 1Gyr and the number of particles to 5.10^5. I have checked that the time necessary for the formation of the bar is roughly the same in every run and that main properties of the bar (semi major-axis length, axis ratio and pattern speed) are comparable. Table 2.1 summarizes the values of these parameters for each simulation code. The bar semi major-axis length L_{bar} and its axis ratio (length of the major-axis / length of the minor-axis) were determined by a simple ellipse fitting of the isophotes. The pattern speed of the bar Ω_p was computed using the Tremaine-Weinberg method (Tremaine & Weinberg, 1984).

These quick tests show that no significant difference can be found between the three different codes when using the same initial conditions.

Every subsequent simulations aimed at testing the validity of initial conditions and/or the formation of bar-like structure during the simulated evolution time were run with *PMSPH* and *GADGET-2*. Bigger simulations with a high number of particles requesting big memory allocation could then safely be run with the *PM/sticky particle* code without wasting computational time.
In a second stage when adding a gas component and star formation to models, only *PMSPH* was used for test simulations. Indeed, as previously mentioned in section 2.3.1, our version of *GADGET-2* did not allow for a treatment of the star formation process.

This strategy only aimed at runing several simulations in a short time scale because of the time constraint intrinsic to a three years PhD thesis.

2.4.2 Important comment

The computation node at IDRIS dedicated to the *PM/sticky particle* code has been recently shut down. Thus, future simulations representing the continuation of present work would (probably) have to be run with the powerful adaptive mesh refinement code `RAMSES` initially developed by Romain Teyssier (see Teyssier, 2002).

Chapter 3

Dynamical modelling of barred systems

3.1 Introduction

The determination of the masses (or equivalently mass-to-light ratios) of gas-poor galaxies has been an important issue since the discovery that galaxies are stellar systems like the Milky Way, with mass being a strong driver of many of their properties. Dynamical modelling methods of increased sophistication have been developed over the past decades, all based on the assumption that galaxies can be described as stationary systems. The first attempt at measuring dynamical masses of galaxies were based on the spherical virial equations (Poveda, 1958; Spitzer, 1969). These methods have the disadvantage that, for accurate results, they need to assume self-similarity in the galaxy light and mass distribution. More accurate methods allow for axisymmetry and take the galaxy light distribution into account. The first detailed axisymmetric models of real galaxies were based on the Jeans (1922) equations and assumed a distribution function that depends on two (out of three) integrals of motion (e.g Binney et al., 1990; van der Marel et al., 1990; Emsellem et al., 1994b), but special classes of three-integral models were also used. Axisymmetric methods were developed to allow for a general orbital distribution, based on Schwarzschild (1979) numerical orbital superposition method (e.g. Cretton et al., 1999; van der Marel et al., 1998; Gebhardt et al., 2003; Thomas et al., 2004; Cappellari et al., 2006). Currently the most general available models assume galaxies can be approximated by a stationary triaxial shape (e.g. de Lorenzi et al., 2007; van den Bosch et al., 2008).

The above modelling techniques were developed under the assumption that gas-poor galaxies can be well described by stationary axisymmetric or triaxial spheroidal systems. However a key initial result of the ATLAS^{3D} survey (Cappellari et al., 2011a, hereafter Paper I) is the fact that nearby gas-poor galaxies are actually dominated (86 per cent of them) by fast rotators (Krajnović et al., 2011; Emsellem et al., 2011, hereafter Paper II and Paper III), often with significant disk components and resembling spiral galaxies with the dust removed (Cappellari et al., 2011b), 30% of which at least are barred. The presence of these bars is a difficult problem for all modelling methods and therefore motivates the present study.

Bars are density waves which results in a tumbling potential: this figure rotation is often ignored in the popular dynamical modelling methods described above. Dynamical models of barred galaxies have been constructed in the past (e.g. Pfenniger, 1984; Häfner et al., 2000; Zhao, 1996), however

their application to the mass determination of external galaxies is not the solution to the problem. The reasons for this is the presence of intrinsic degeneracies in the dynamical modelling problem. In fact even the full amount of information one can obtain today for external galaxies, namely the full line-of-sight velocity distribution (LOSVD) at every position on the sky, is not sufficient to uniquely constrain the two free parameters (M/L and inclination) of a simple self-consistent axisymmetric model (Valluri et al., 2004; Krajnović et al., 2005; Cappellari et al., 2006; van den Bosch & van de Ven, 2009). A barred model requires at least two extra parameters (the Position Angle (PA) and pattern speed of the bar) and dramatically increases the complexity of the orbital structure and the associated degeneracy of the problem, instead of improving the accuracy of the mass estimate: a broad range of parameters space may well fit the data equally well. Moreover, assuming a galaxy is barred also increases the degeneracy in the mass deprojection problem (e.g. Gerhard, 1996), which is already mathematically non unique in the simple axisymmetric case (Rybicki, 1987). The application of sophisticated barred models to large samples would be computationally challenging, but feasible exploiting the trivial parallelism of the problem. However, this brute-force approach does not remove the intrinsic degeneracies so it is not expected to increase the accuracy of the mass determinations, and for this reason does not seem justified.

An alternative approach consists of using some a priori information on the galaxy structure and make empirically-motivated restrictive assumption on the models. This is the approach we are using in the systematic determination of the masses of the 260 early-type galaxies of the ATLAS^{3D} survey (Cappellari et al., 2010). We are applying the Multi-Gaussian Expansion (MGE) technique (Emsellem et al., 1994a) to accurately describe the photometry of all galaxies in the survey (Scott et al. in prep) and use the Jeans Anisotropic MGE (JAM) modelling method (Cappellari, 2008) to measure masses. The JAM method is based on a simple and very efficient solution of the Jeans equations which allows for orbital anisotropy $\beta_z = 1 - (\sigma_z/\sigma_R)^2$. This approach provides good descriptions of the integral-field kinematics of the fast rotator early-type galaxies (Cappellari, 2008; Scott et al., 2009, Cappellari et al. in prep.), which constitute the large majority of the ATLAS^{3D} sample (see Paper II and Paper III). A key motivation for our use of the JAM method is that it was shown, using 25 real galaxies (Cappellari et al., 2006; Cappellari, 2008), to agree well within the model uncertainties in the mass determination obtained with the more general axisymmetric Schwarzschild approach.

The use of an axisymmetric dynamical modelling method to measure the mass of barred galaxies raises the obvious question of what errors in the mass determination are introduced by the approach. Answering this question is the goal of this paper. Our work is in its spirit an extension of the work by Thomas et al. (2007) to barred disk galaxies, which explored the biases introduced by the use of axisymmetric models, when extracting masses of triaxial and prolate simulated spheroidal galaxy remnants.

The paper is structured as follows: in Section 3.2 we briefly describe the Multi-Gaussian Expansion parametrization from Emsellem et al. (1994a), the semi-isotropic Jeans equations and the method used to create the N-body galaxy models. In Section 3.4, we give an overview of the input models used for the JAM modeling in our investigation, and in Section 3.5 we compare the original and recovered values of the corresponding dynamical parameters. Section 3.6 summarizes all results.

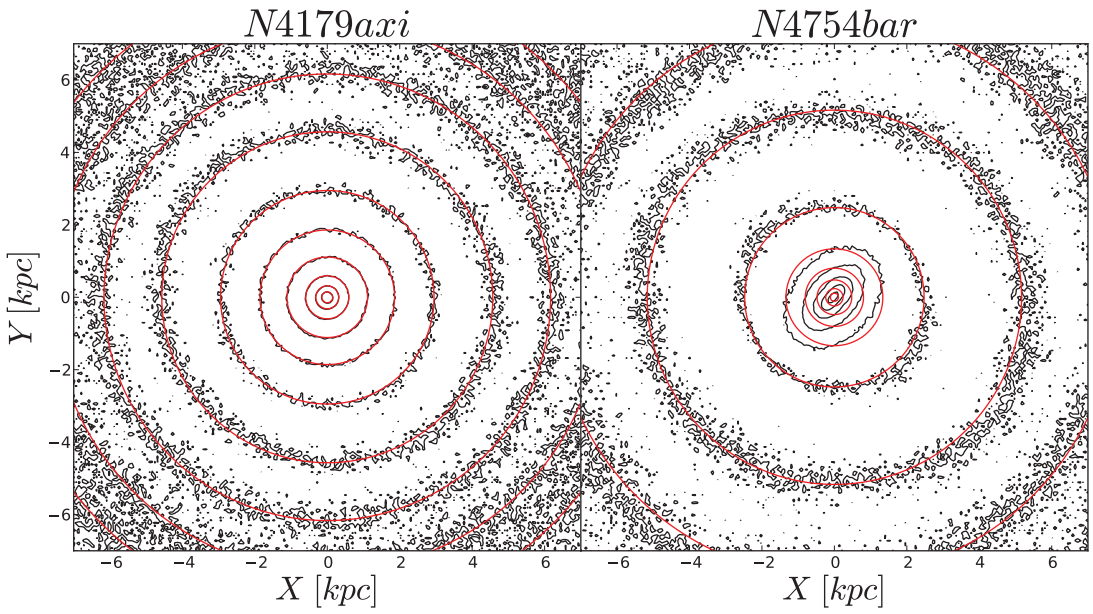

Figure 3.1: Examples of MGE fits to two model galaxies with a projection angle of $i = 25°$. The left panel shows the MGE fit to simulated galaxy N4179axi, an axisymmetric object. On the right we show the fit to N4754bar with $\mathrm{PA_{bar}} = 60°$, where the bar was excluded from the fit.

3.2 Mass modeling

3.2.1 Multi-Gaussian Expansion method

We use in our study the Multi-Gaussian Expansion method described in Emsellem et al. (1994a) and Cappellari (2002). The technique basically consists of decomposing the luminosity into a number of concentric two-dimensional (2D) Gaussians. By fitting the detailed surface brightness distribution, the MGE formalism provides a description of the intrinsic luminosity density, which converts to the mass distribution via the assumed constant M/L. From galaxy images this formalism allows us to generate realistic initial conditions for our N-body simulations using the method explained in Sec 3.3. The MGE parametrization is also the first and crucial step of the JAM modeling. Thus, a rigorous and robust approach is needed when producing the MGE model of a galaxy, as the predicted kinematics may significantly depend on the obtained mass distribution (see Sec 3.2.3). The method and software[1] we adopt in our study to produce MGE parametrization is fully described in Cappellari (2002).

Once the best fit has been found, we have a description of the galaxy surface brightness distribution given as a sum of two-dimensional Gaussians which we can attempt to deproject. The deprojection of a galaxy surface brightness distribution is formally non-unique for all but edge-on cases, and the degeneracy can become severe at low inclinations (Rybicki, 1987). The MGE method provides just *one* solution for the deprojection, in terms of a sum of three-dimensional Gaussians.

[1] available from http://purl.org/cappellari/idl

This method has been intensively used and usually provides luminosity distributions consistent with observed photometry of existing galaxies, but the MGE method obviously does not remove the existing intrinsic degeneracy.

The deprojection of an MGE model can be done analytically once the viewing angles are known (see Monnet et al., 1992). When the system is assumed to be axisymmetric, only one viewing angle, the inclination i ($i = 90^\circ$ for an edge-on system), is sufficient to retrieve the full three-dimensional luminosity distribution ν (if the galaxy is not face-on).

In a coordinate system (x', y', z') centered on the galaxy nucleus with z' pointing toward us and (x', y') being the plane of the sky, the MGE surface brightness can be written as:

$$\Sigma(x', y') = \sum_{k=1}^{N} \frac{L_k}{2\pi\sigma_k'^2 q_k'} \exp\left[-\frac{1}{2\sigma_k'^2}\left(x_r'^2 + \frac{y_r'^2}{q_k'^2}\right)\right] \tag{3.1}$$

where N is the number of adopted gaussian components, each having an integrated luminosity L_k, an observed axial ratio $0 \leqslant q_k' \leqslant 1$, a dispersion σ_k' along the major axis, and a position angle (PA) ψ_k measured counter-clockwise from y' to the major-axis of the Gaussian, with (x_r', y_r') being the associated rotated coordinate system.

The MGE parameters are fixed by minimizing the non-linear function of Eq. 3.2 restricted to selected pixels of a galaxy image:

$$\chi^2 = \sum_{ij} \left[\frac{C_{ij} - \Sigma(x_i', y_j')}{\Delta_{ij}}\right]^2, \tag{3.2}$$

where C_{ij} are selected pixel counts and Δ_{ij} are corresponding weight factors (e.g., measurement errors). The deprojection of an MGE model can be done analytically once the viewing angles are known (**?**). When the system is assumed axisymmetric, only one viewing angle, the inclination i ($i = 0$ for a face-on system), is sufficient to retrieve the full three-dimensional luminosity distribution ν (if the galaxy is not face-on).

The deprojected MGE luminosity distribution in cylindrical coordinates can be expressed as:

$$\nu(R, z) = \sum_{k=1}^{N} \frac{L_k}{(\sqrt{2\pi}\sigma_k)^3 q_k} \exp\left[-\frac{1}{2\sigma_k^2}\left(R^2 + \frac{z^2}{q_k^2}\right)\right] \tag{3.3}$$

where the k-th gaussian has the total luminosity L_k, intrinsic axial ratio q_k and dispersion σ_k. The intrinsic axial ratio q_k can then be written as

$$q_k^2 = \frac{q_k'^2 - \cos^2 i}{\sin^2 i}, \quad \text{for } i \neq 0 \tag{3.4}$$

where i is the galaxy inclination.

3.2.2 MGE modeling of barred and unbarred S0 galaxies

The fitting of the MGE to the photometry follows the procedure applied by Scott et al. (2009) (see their Fig. 2) to deal with the presence of bars. This same approach is being applied to the MGE fits of the ATLAS^{3D} sample (Scott et al. in preparation). The procedure allows to find the best fit to the photometry while maximizing the minimum q_k' and minimizing the maximum q_k'. For near face-on cases, a small deviation in the observed axis ratios implies an important change in the

flatness (or roundness) of the mass distribution. As the previous procedure frequently ends with very similar lower and upper limits for q'_k, we force a common axis ratio for all Gaussians for such cases to keep an acceptable global shape for our MGE model.

When the bar clearly affects the projected photometry of our models (i.e., when it is easily detected), the method adopted for the MGE parametrization consists in forcing the lower and upper limit of the gaussian axis ratios. In this context, a bar can be considered as a perturbation of a disk structure. Bars, if fully fitted by MGE components, appear as Gaussians elongated along the apparent long axis of the bar. The presence of a bar tends to significantly affect the q'_k values of a few Gaussians depending on its position angle, strength and length (the position angle of the bar $\mathrm{PA_{bar}}$ being measured counter-clockwise from the projected major-axis of the galaxy). The resulting q'_k could thus make the system look flatter (or rounder) than the corresponding axisymmetric case if the bar is seen end-on (resp. side-on). Previous tests made in Scott et al. (2009) showed that the best fitting MGE parametrization of a barred galaxy is usually not the one which allows the best fit to the observed kinematics (using JAM models). The kinematic fit is significantly improved when the Gaussians have constrained axial ratios such that the systems is forced to an axisymmetric "bar-less" MGE parametrization. As bars often only affect the photometry within a restricted radial range, we use the outer disk of each galaxy to constrain the imposed value of the flattening and inclination. Figure 3.1 gives two examples of the resulting MGE fits for an axisymmetric simulation and a barred simulation.

3.2.3 Jeans Anisotropic MGE Modeling

The JAM method is a powerful approach to model the stellar kinematics of early-type galaxies, providing a good description of the first two stellar velocity moments (V, $V_{\rm rms}$) of a stellar system. This technique can be used to probe the dynamical structure of ETGs and does in principle allow the recovery of the inclination and the dynamical mass-to-light M/L ratio. The JAM technique allows for a different M/L and anisotropy for each individual MGE Gaussian component. However, the measurement of a global mass for real galaxies does not seem to require this extra generality, at least within $1R_e$, where good quality integral-field data are available (Emsellem et al., 2004, and Paper I). For this reason the models we use make the following simple assumptions (a full description of JAM is provided in Cappellari, 2008):

1. An axisymmetric distribution of the mass.
2. A constant mass-to-light M/L ratio.
3. A constant anisotropy described by the classic anisotropy parameter $\beta_z = 1 - \overline{v_z^2}/\overline{v_R^2}$ with $\beta_z \gtrsim 0$.

Starting from the parametric description of the stellar density distribution from the MGE model, we use an anisotropic generalization of the semi-isotropic axisymmetric Jeans equation in cylindrical coordinates (R, z, ϕ) to derive the corresponding spatial velocity moments:

$$\frac{b\nu\overline{v_z^2} - \nu\overline{v_\phi^2}}{R} + \frac{\partial b\nu\overline{v_z^2}}{\partial R} = -\nu\frac{\partial\Phi}{\partial R} \tag{3.5}$$

$$\frac{\partial\nu\overline{v_z^2}}{\partial z} = -\nu\frac{\partial\Phi}{\partial z}, \tag{3.6}$$

Model	Galaxy/Model	Distance (Mpc)	N_*	β_{zi}	β_{zf}	σ_ϕ/σ_R	time(Gyr)	bar
N4179axi	NGC4179	16.5	4e6	$\beta(\varepsilon)$	0.106	1.8	1.5	no
N4570axi	NGC4570	17.1	4e6	0.0	0.145	1.0	1.5	no
N4442bar	NGC4442	15.3	4e6	$\beta(\varepsilon)$	0.344	1.8	1.5	yes
N4754bar	NGC4754	16.1	4e6	$\beta(\varepsilon)$	0.343	1.8	1.5	yes

Table 3.1: Table providing a list of simulations with their labels and their specifications. Distances are set according to Paper I. N_* is the number of particles. β_{zi} gives the anisotropy of the initial conditions as described in Section 3.3.1. β_{zf} is the global anisotropy computed for the final state of our simulations. σ_ϕ/σ_R gives the second relation for the geometry of the velocity dispersion ellipsoid for the initial conditions. The time given in the eighth column correponds to the simulated time of evolution. The last column indicates whether a bar appeared or not in our simulations.

where $b = \overline{v_R^2}/\overline{v_z^2}$, and with the notation

$$\nu\overline{v_k v_j} \equiv \int v_k v_j f d^3\mathbf{v} \tag{3.7}$$

The anisotropy parameter can be expressed as $\beta_z = 1 - 1/b$, such that $\beta_z = 0$ corresponds to isotropy. With the additional boundary condition $\nu\overline{v_z^2} = 0$ as $z \to \infty$ the solution is

$$\nu\overline{v_z^2}(R,z) = \int_z^\infty \nu\frac{\partial\Phi}{\partial z}dz \tag{3.8}$$

$$\nu\overline{v_\phi^2}(R,z) = b\left[R\frac{\partial(\nu\overline{v_z^2})}{\partial R} + \nu\overline{v_z^2}\right] + R\nu\frac{\partial\Phi}{\partial R}dz. \tag{3.9}$$

When the mass distribution is represented via an MGE parametrization (see Sect. 3.2 above), the Jeans equations can be easily integrated along the line-of-sight as shown by Emsellem et al. (1994a) in the semi-isotropic case ($\sigma_z = \sigma_R \neq \sigma_\phi$) and by Cappellari (2008) in the anisotropic generalization ($\sigma_z \neq \sigma_R \neq \sigma_\phi$). Here we use the anisotropic formulas (equations 28 and 38 of Cappellari (2008)) to derive the projected first and second velocity moments (V and $V_{\rm rms}$) given a set of input parameters (MGE mass model, mass-to-light ratio M/L, anisotropy β), and thus find the best fitting values within a sampled predefined solution space (e.g., $\beta \geq 0$)

Such a JAM method has been systemically applied to `SAURON` integral-field stellar kinematics of all 260 early-type galaxies of the ATLAS^{3D} sample. In the present study, we rely on mock observations computed from N-body simulations of galaxies, and we chose to build JAM models from artificial maps to mimic the procedure used in the course of the ATLAS^{3D} survey. We also exclude the central few arcseconds during the fitting process, which e.g., avoids biases due to the effect of the seeing. We also re-bin all maps before fitting by using the Voronoi tessellation as described in Cappellari & Copin (2003): this allows a guaranteed minimum signal-to-noise ratio in each bin, and reduces the scatter in the outer parts of the kinematic maps.

Model	Galaxy/Model	Distance (Mpc)	N_*	β_{zi}	σ_ϕ/σ_R
Hern01	Hernquist	10.0	2e6	0.0	1.0
Hern02	Hernquist	10.0	2e6	0.2	1.0
Hern03*	Hernquist(flat)	10.0	2e6	0.0	1.0
Hern04*	Hernquist(flat)	10.0	2e6	0.2	1.0
N4754ini	NGC4754	16.1	4e6	0.2	1.0

Table 3.2: Table providing a list of the tests simulations (static models) with their labels and their specifications. Distance of $N4754ini$ was set according to Cappellari (2011), while for Hernquist models it was set arbitrary. N_* is the number of particles. β_{zi} gives the anisotropy of the initial conditions as described in Section 3.3.1. σ_ϕ/σ_R gives the second relation for the geometry of the velocity dispersion ellipsoid for the initial conditions.

3.3 N-body simulations of regular-rotator galaxies

As the main motivation of our study is to find the influence of a bar on the recovery of basic dynamical parameters with the JAM method, we chose to use an N-body approach to generate simulations of barred early-type galaxies: knowing the exact input dynamics for these simulations, we can then compare the key parameters with those determined via the JAM modeling. We also made static realizations of a few (Hernquist and one typical axisymmetric lenticular) mass models, and thus only used the initial realization of the N-body distribution. These models are detailed in Table 3.2, while details for evolved simulations are summarized in Table 3.1. The method to build the initial conditions for our simulations (to be evolved, or not) is detailed below.

3.3.1 Particle positions

Starting from the MGE parametrization of a mass distribution (after taking into account the mass-to-light ratio M/L), the initial positions of the particles can be computed easily. Each Gaussian represents a fraction of the total mass, so that given a total number of particles per component we can determine N_k, the number of particles of that k-th Gaussian. All components are truncated at a chosen radius. To set up the position of each particle, we use a standard realization method with a random generator via the cumulative function of a (truncated) Gaussian function, scaling each spatial dimension with the corresponding spatial dispersion.

Dynamical structure

Given the particle position, we compute the velocity dispersion components σ_R, σ_ϕ and σ_z solving Jeans' Equations (Jeans, 1922) equations, within the MGE formalism of Emsellem et al. (1994a). For this work we use the anisotropic generalization of the method (equations 19–21 and 34 of Cappellari (2008)), which allows one to set arbitrary ratios σ_z/σ_R and σ_ϕ/σ_R for the axes of the velocity ellipsoid, which is assumed to be cylindrically oriented. Values for these ratios can be set individually for each gaussian component, but in this study all Gaussians share the same geometry of its velocity dispersion ellipsoid. For some of the simulations initial conditions, we used the following (so-called $\beta - \epsilon$, with ϵ the intrinsic galaxy ellipticity) relation to fix σ_R/σ_z:

$$\beta_z = 1 - \left(\frac{\sigma_z}{\sigma_R}\right)^2 = 0.6 \times \epsilon \tag{3.10}$$

This a purely empirical relation which seems to describe the general trend in the anisotropy of real fast rotator galaxies (Cappellari et al., 2007).

3.3.2 Simulation code

The numerical simulations are performed with a particle-mesh N-body code (Bournaud et al., 2007a). The density is computed with a Cloud-in-Cell interpolation, and an FFT-based Poisson solver is used to compute the gravitational potential, with a spatial resolution and softening of 48 pc. Particle motions are integrated with a leap-frog algorithm and a time-step of 0.1 Myr. The number of particles and the time evolution of each model are given in Table 3.1.

3.4 Inputs for JAM models

3.4.1 Unbarred simulations

We first built four simple simulations based on the analytic Hernquist (1990) mass distribution

$$\rho(r) = \frac{M}{2\pi}\frac{a}{r}\frac{1}{(r+a)^3} \tag{3.11}$$

where M is the total mass and a is a scale length. These simulations allowed us to quickly check and confirm the accuracy of the JAM modeling method for spherical isotropic ($Hern01$), spherical anisotropic ($Hern02$), flat isotropic ($Hern03$) and flat anisotropic ($Hern04$) particle realizations. For all these simulations the inclination was recovered within an error of less than 2°, the global anisotropy was accurately recovered within an error of ± 0.025 and the error on M/L never exceeded 1.5%

We then considered a more realistic numerical test, using the MGE parametrization of the SDSS r-band image of the real galaxy NGC4754 and a constant anisotropy and we label this model $N4754ini$. When computing the particle velocities, we forced $\beta_z = 0.2$ for all Gaussians. In contrast to the above-mentioned Hernquist models, $N4754ini$ represents a complex multi-component object in terms of its mass distribution and kinematics, and is therefore expected to be more challenging for the JAM modeling method.

We also built two simulations, respectively based on the MGE parametrizations of NGC4570 and NGC4179, which were evolved via N-body simulations during 1.5Gyr. These two simulations can be considered as fully relaxed, and contrarily to $N4754ini$ and the Hernquist models, the resulting β_z is measured not to be constant with radius. One important difference between $N4570axi$ and $N4179axi$ is that, while the initial conditions for $N4570axi$ were fixed as isotropic ($\beta_z = 0$), the ones for $N4179axi$ were those of a dynamically cold disk as described in Table 3.1. No bar formed either for $N4179axi$ or $N4570axi$.

Projected velocity and velocity dispersion maps of our two axisymmetric simulations with variable β_z are presented in Figure 3.2. The second velocity moment is dominated by the dispersion in the central region, and by the velocity in the outer parts. The profile of $V_{\rm rms}$ also shows a central depletion.

Figure 3.3 present the local anisotropy β_z as measured in the meridional plane and the equatorial plane, computed on a cylindrical grid with linearly spaced cells in R, in z and in angle ϕ where (R,ϕ,z) are the standard cylindrical coordinates, including a central cylindrical cell with a radius of $R_c = 0.01$kpc. This highlights the fact the anisotropy is not constant in our axisymmetric

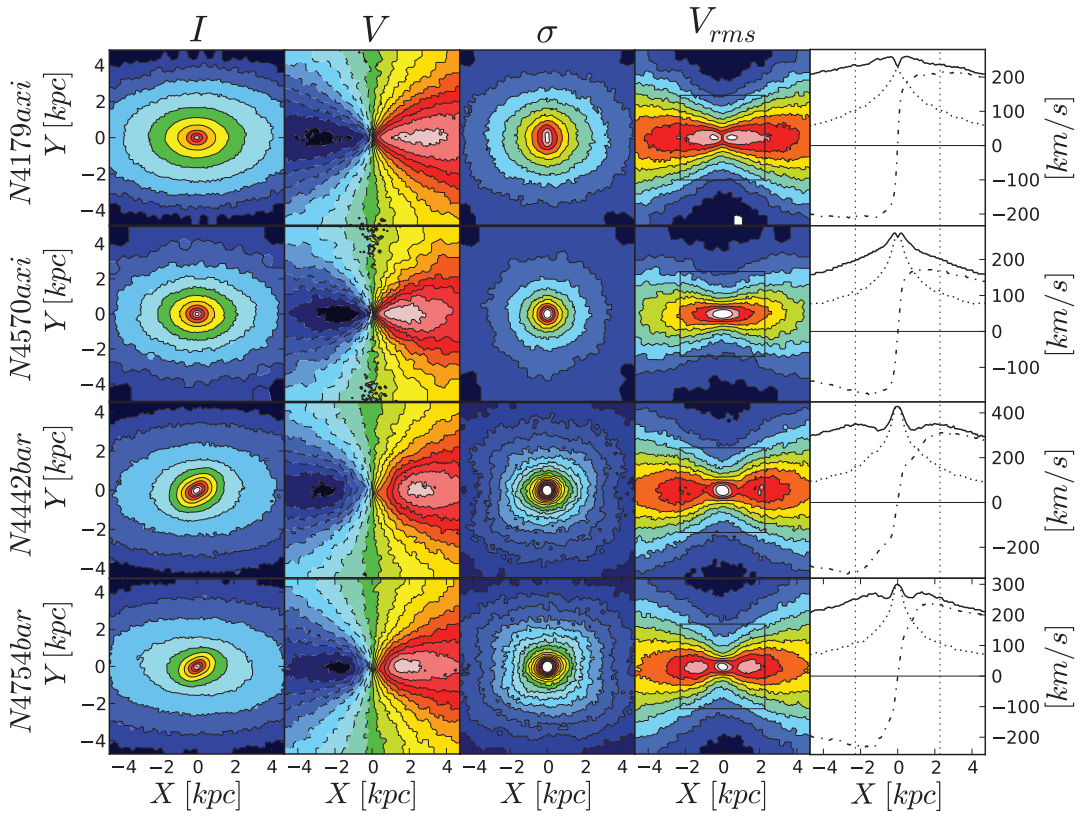

Figure 3.2: Binned map of the projections of the final state of our simulations with an inclination $i = 60°$ and $\mathrm{PA_{bar}} = 60°$ for barred simulations. From left to right : total projected luminosity I ; mean velocity along the line-of-sight V_{LOS} ; velocity dispersion along line-of-sight σ_{LOS} ; projected second velocity moment $V_{\mathrm{rms}} = \sqrt{V_{\mathrm{LOS}}^2 + \sigma_{\mathrm{LOS}}^2}$; profiles of V_{LOS} (dot line), σ_{LOS} (dash-dot line) and V_{rms} (solid line) along the galaxy major axis. From top to bottom : $N4179axi$; $N4570axi$; $N4442bar$; $N4754bar$.The square box in the V_{rms} map and the vertical dot lines in the profiles represent the typical field of view used in our study.

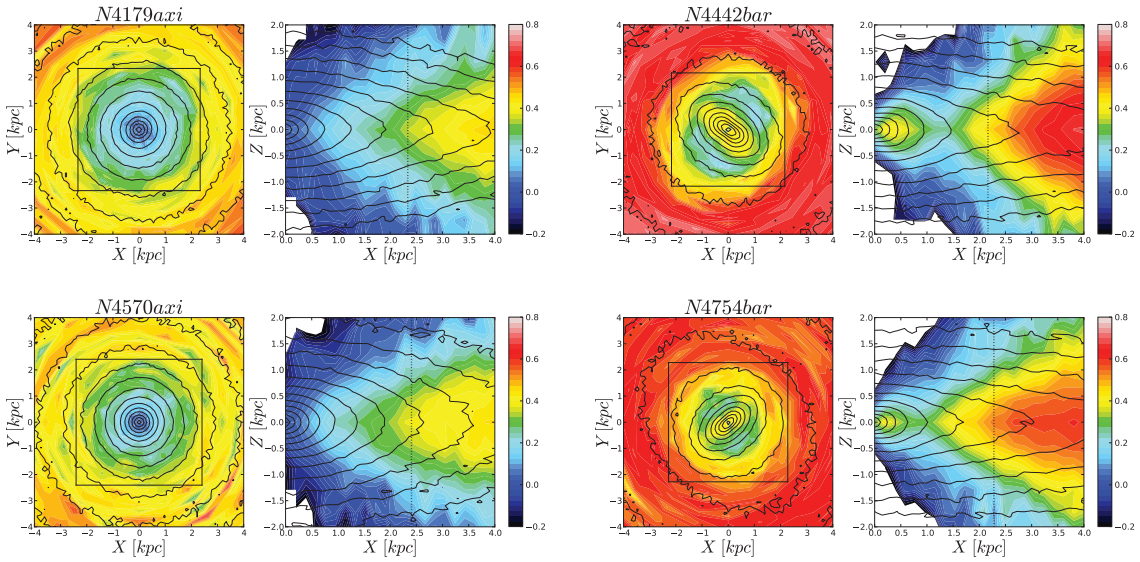

Figure 3.3: Maps of the local values of the anisotropy β_z in the equatorial plane and in the meridional plane of $N4179axi$ (upper left), $N4570axi$ (bottom left), $N4442bar$ (upper right) and $N4754bar$ (bottom right). Colour gradients for the anisotropy go from $\beta_z = -0.2$ (i.e. $\sigma_z > \sigma_R$) to $\beta_z = 0.8$ (i.e. $\sigma_z < \sigma_R$). The field of view used in our study is represented by the solid square for the equatorial plane and by the vertical dot line for the meridional plane.

.

simulations and that the central parts are more isotropic than the outer regions. In Figure 3.4, we show that the radial anisotropy profile (which is simply the azimuthal average of the equatorial computation) generally increases outwards for these axisymmetric simulations.

3.4.2 Barred simulations

We also developed bar simulations, $N4442bar$, and $N4754bar$, based on the initial MGE parametrizations of NGC4442 and NGC4754, respectively: these are the final state of two N-body simulations after 1.5 Gyr of evolution. To generate a bar, we artificially force a cold dynamical structure in the initial particle realisations by setting in the initial conditions $\sigma_\phi < \sigma_R$. The radial velocity dispersion σ_R was set using the $\beta(\varepsilon)$ function described in Eq. 3.10. With these conditions, a bar appears in each of these simulations after only a few rotation period, namely between about 25 Myr and 50 Myr of simulated evolution. As mentioned, we let the galaxy evolve for 1.5 Gyr, to make sure that the bar is well settled.

$N4442bar$ presents the biggest bar (in size) of our simulations: we estimate a semi-major axis of 3.0 kpc. The size of the bar is determined using the radial flattening ($q_{isophote} = 1 - \epsilon_{isophote}$) and the position angle ($PA_{\rm isophote}$) of isophotes as done in Michel-Dansac & Wozniak (2006). Basically the end of the bar corresponds to a radius where isophotes are nearly round ($q_{isophote} > 0.9$) combined with an important change in the position angle. Using the same method we determine the semi-major axis of the bar for $N4754bar$ to be 2.2 kpc. Outside of the bar regions, our two simulations are characterized by a rotation pattern consistent with an axisymmetric disk-like system.

The velocity fields of our barred simulations are shown in the two lower panels of Figure 3.2.

As for the axisymmetric cases, the $V_{\rm rms}$ maps are dominated by velocity dispersion in the central parts and by the mean velocity in the outer parts. But in contrast to the $N4179axi$ and $N4754ini$ simulations, the barred simulations all show a peak in the center of the $V_{\rm rms}$ maps. This apparent difference between the barred and unbarred cases has important consequences, since this will condition the fit of the projected second velocity moment via a JAM model.

Figure 3.3 and Figure 3.4 show that the local anisotropy starts from a central value of 0.3, reaching a minimum of nearly 0.2 close to the end of the bar, then increasing in the outer parts of the model up to 0.7. The derivation of β_z in the equatorial plane confirms the presence of a drop in β_z in the outer parts of the bar.

3.4.3 Mock observations

As input for the JAM modeling, we simulated observations by projecting our simulations first with four different inclinations: $i = 25°$; $i = 45°$; $i = 60°$ and $i = 87°$, ($i = 0°$ corresponding to the face-on projection, and $i = 90°$ to the edge-on projection). The choice of a near edge-on projection instead of an exact edge-on projection was motivated by the goal of checking the accuracy of the inclination recovery. Indeed the edge-on projection does not allow an overestimation of i and then limits the range of possible uncertainty. When a bar is present, we also used four different position angles for the bar, and this for each value of the inclination: $\mathrm{PA_{bar}} = 18°$; $\mathrm{PA_{bar}} = 45°$; $\mathrm{PA_{bar}} = 60°$ and $\mathrm{PA_{bar}} = 87°$. The position angle of the bar is measured counter-clockwise from the galaxy projected major-axis to the bar major-axis, so that $\mathrm{PA_{bar}} = 87°$ is close to having the bar end-on and $\mathrm{PA_{bar}} = 18°$ close to side-on. We also simulated the SAURON pixels size of 0”8 assuming a distance for each model as given in Table 3.1 typical of ATLAS$^{\rm 3D}$ objects.

For real galaxies the photometry is available over a much larger field of view than the kinematics. For each projection, the MGE parametrization was achieved using a rather wide field of view of 401×401 pixels corresponding to 320.8 arcsec, and including the full model. Then, the JAM modeling was done on a 73×73 pixels map (58.4 arcsec) of the second velocity moment with the simulated galaxy centered on its nucleus, as this roughly corresponds to the setup for a single SAURON exposure.

3.5 Recovery of parameters

The recovery of i, β_z and M/L with JAM is done on $V_{\rm rms}$ maps only. The prediction of V and σ require an extra assumption on the constancy of the tangential anisotropy of the JAM models. This assumption may not be well verified in the simulations, especially in barred ones. However the accuracy in the determination of the above parameters is only dependent on the ability of JAM to reproduce the $V_{\rm rms}$, and not the V and σ fields separately. Details of the method to calculate V and σ can be found in Cappellari (2008).

3.5.1 Recovery of β_z and inclination

As shown in Figure 3.4 the anisotropy varies significantly when going from the inner to the outer parts of our simulations.

The JAM modelling method allows for a different anisotropy β_z for every individual MGE Gaussian. However here we limit ourselves to the simple case where β_z is constant for the whole model. Tests using 25 real galaxies (Cappellari et al., 2006; Cappellari, 2008) have shown that

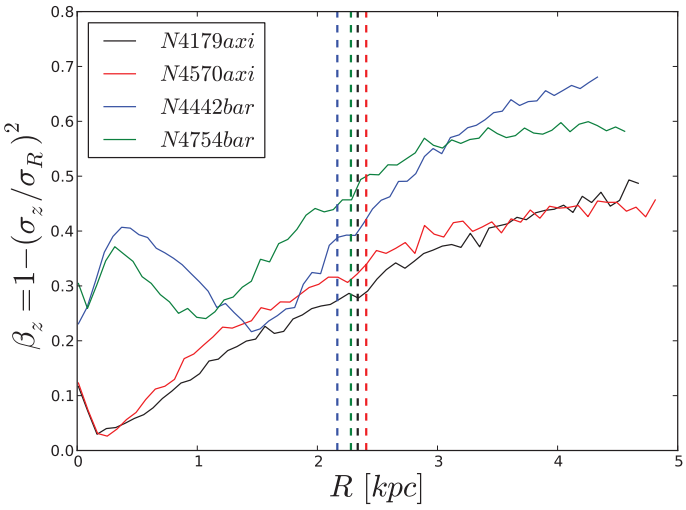

Figure 3.4: Azymuthally averaged profile of the anisotropy computed in an equatorial plane ($-0.5kpc < z < 0.5kpc$) for axisymmetric simulations ($N4179axi$ and $N4570axi$) and barred simulations ($N4442bar$ and $N4754bar$). The vertical dash-dot lines correspond to the field of view used for the JAM models and therefore the region in which we derived the global anisotropy.

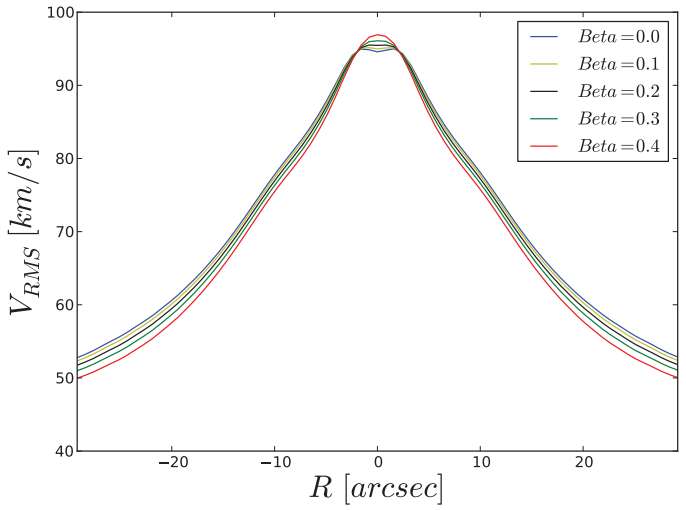

Figure 3.5: Effect of the anisotropy parameter β_z on the observed $V_{\rm rms}$ profile along major axis at an inclination of $i = 18°$. The difference between all profiles is too small to allow a good recovery of β_z at such low inclination.

even with constant anisotropy the recovered M/L agrees with the one derived with Schwarzschild models, which allow for a general anisotropy distribution. The extra generality of JAM is therefore not required in this case. Thus, for comparison, we compute a global anisotropy for our simulations by doing a luminosity-weighted average of the local anisotropy for all of our simulations. In the following we discuss the issue of the inclination-anisotropy degeneracy intrinsic to galaxy dynamics and also the important influence of the MGE parametrization on the recovery of the global anisotropy. The global anisotropy recovered with the JAM modeling method is noted $\beta_z^{\rm JAM}$ and the one computed directly from the simulation $\beta_z^{\rm SIM}$.

Anisotropy-inclination degeneracy

As shown in Krajnović et al. (2005) and with more galaxies in Cappellari et al. (2006) there is an intrinsic degeneracy in the dynamical problem between the recovery of the inclination and the anisotropy: given the observed photometry, the observed kinematics can be reproduced in detail for a wide range of inclinations, by varying the orbital make up of the models. This degeneracy persists even in the restricted case in which the anisotropy is assumed to be constant for the whole galaxy (Cappellari, 2008). The degeneracy can only be broken by making empirically-motivated assumptions on the anisotropy. This was the approach adopted by Cappellari (2008), who showed using a small sample of galaxies that, if β_z is assumed to be positive, as determined using general models on large samples of galaxies (Cappellari et al., 2007; Thomas et al., 2009), the correct inclination can be recovered from the observed integral-field kinematics.

Here we test the inclination recovery via JAM using N-body simulations of both unbarred (i.e. $N4179axi$ and $N4570axi$) and in particular barred galaxies (i.e. $N4442bar$ and $N4754bar$), for which the inclination is known. We confirm the fact that, despite the inclination-anisotropy degeneracy the inclination can be recovered in axisymmetric simulations, and we additionally find that the inclination can be recovered even in barred simulations. The influence of i on the second velocity moment map is important at low inclination. A slight change in the inclination implies a significant change in $V_{\rm rms}$ (which is more directly related to the change in the axis ratio), and then allows a good recovery of the inclination value i. At higher inclination, the change in ellipticity is milder and $V_{\rm rms}$ is less influenced by small variations. In all cases, the uncertainty never exceeds a few degrees, even when the fit can be considered difficult due to the presence of non-axisymmetric features such as a bar. We also confirm that at low inclinations there is a degeneracy in anisotropy in the $V_{\rm rms}$ fit, essentially preventing any information on the anisotropy from being extracted from the data in that case. As shown in Figure 3.5, changes induced by the anisotropy parameter on the $V_{\rm rms}$ profiles are not significant for $i = 18°$. This is due to the fact that at low inclination, maps of the second velocity moment are dominated by σ_z. Therefore, to avoid a too strong degeneracy, $i = 25°$ is the lowest inclination we will consider in this study. For lower values, the degeneracy prevents β_z from being usefully recovered.

To summarize, the higher the inclination, the larger the effect of the global anisotropy on the projected $V_{\rm rms}$. For the non-barred simulations we find errors in average of 2 degrees in the tests we performed on eight different projections. For the barred simulations (32 determinations: 2 galaxies projected at 4 inclinations and 4 $\rm PA_{bar}$) the maximum error in the recovered inclination is 6 degrees. The maximum error happens only for $\rm PA_{bar} \sim 90°$, when the bar is seen side-on and it is incorrectly modelled as a thin disk. The error on $\beta_z^{\rm JAM}$ is important at low inclination and decreases from face-on to edge-on projections.

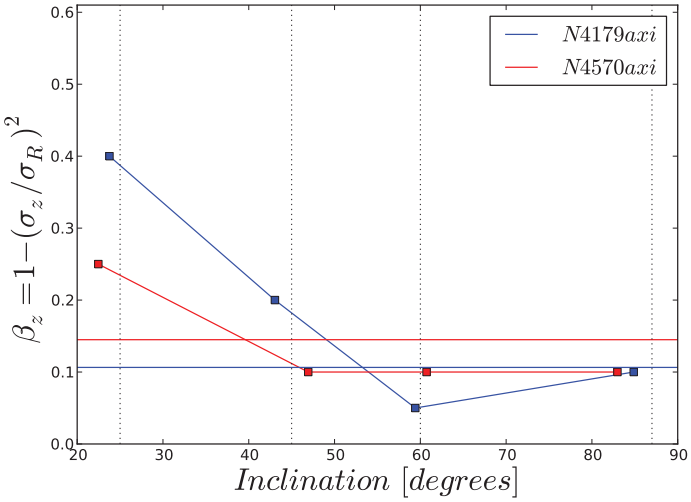

Figure 3.6: Recovered values of the global anisotropy for non-barred simulations as a function of the projection inclination for $N4179axi$ and $N4570axi$. The horizontal lines represent the global anisotropy computed from the particle realization $\beta_z^{\rm SIM}$ (blue for $N4179axi$ and red for $N4570axi$). Vertical lines give the inclination of projections.

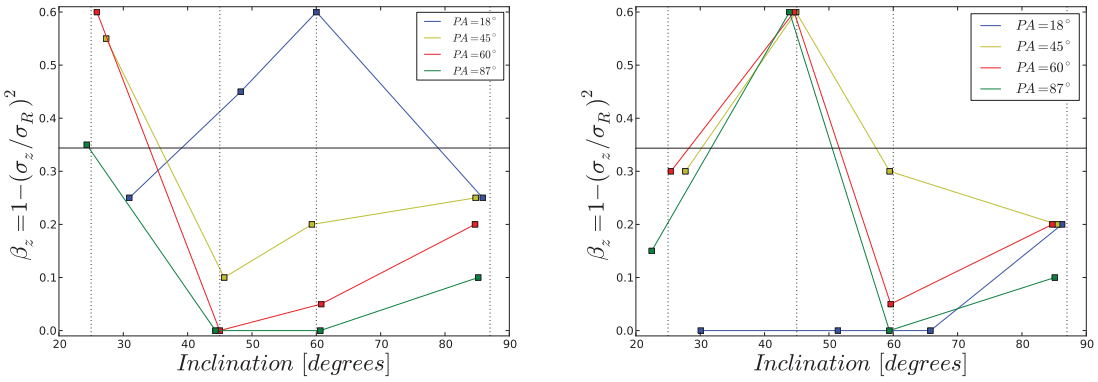

Figure 3.7: Recovered value of the global anisotropy for barred simulations as a function of the projection inclination for $N4442bar$ (left) and $N4754bar$ (right) for different $\mathrm{PA_{bar}}$. The horizontal black solid line represent the value of $\beta_z^{\rm SIM}$ and the vertical lines shows the inclinations of projection.

Influence of the mass deprojection

While the inclination-anisotropy degeneracy is intrinsic to the galaxy dynamics and determines the uncertainties for the recovered global anisotropy and the inclination, $\beta_z^{\rm JAM}$ is also influenced by the mass deprojection. For regular axisymmetric simulations such as $N4179axi$ and $N4570axi$, the MGE parametrization is relatively robust, and $\beta_z^{\rm JAM}$ is generally very close to the known intrinsic value $\beta_z^{\rm SIM}$ (see Figure 3.6). The small deviations are due to the residual degeneracy in the mass deprojection previously explained.

For the barred simulations $N4442bar$ and $N4754bar$, the presence of the bar implies that axisymmetric models cannor reproduce the true stellar density distribution. This means that our MGE parametrization can only provide an approximation. The results presented in Figure 3.7 are obtained by applying the same method used on observations. The axis ratios of the Gaussians were only forced when the bar is clearly seen in the photometry. We can see that the global anisotropy is never well recovered. This is explained by the fact that the presence of the bar will tend to flatten or round the Gaussians in the MGE parametrization if it is seen respectively side-on ($\rm PA_{bar} = 18°$) or end-on ($\rm PA_{bar} = 87°$). It is important to note that this degeneracy, being due mainly to the mass deprojection, is not specific to the adopted dynamical modelling method, but is expected to affect more general method like Schwarzschild's orbit-superposition method. Moreover the anisotropy is formally not a well defined quantity in a barred galaxy, as it is expected to vary with the azimuthal location on the galaxy disks.

To further investigate the impact of the ellipticity ϵ on $\beta_z^{\rm JAM}$, we computed the positions of our mock observations in the $(V/\sigma, \epsilon)$ diagram (Binney, 2005). (V/σ) and ϵ are computed in an ellipse of area $A = \pi R_e^2$ where R_e is the radius of a cylinder enclosing half of the galaxy light. In Figure 3.8 we present the result for near edge-on projections with R going from $0.5 \times R_e$ to $5.0 \times R_e$. We only consider the edge-on case in this figure as all our models follow the inclination law (see Sec. 4.3 of Binney & Tremaine, 1987). For comparison additional simple models were also constructed and projected edge-on. The first one (named Test01) is based on a MGE parametrization with constant $\epsilon = 1 - q$ and isotropic kinematics (black solid line on the Figure 3.8). The second one (Test02) is also isotropic but with a non constant ellipticity in the mass distribution, ϵ increasing with radii (black dashed line).

These two test models highlight the fact that when the considered area A is increased (V/σ) increases as to roughly follow the constant anisotropy lines. The axisymmetric model $N4179axi$ also lay on a constant anisotropy line although its dynamical structure presents a β_z gradient. Barred simulations present a different behavior depending on $\rm PA_{bar}$. With broad field of view (FOV) the only effect of the bar is seen through (V/σ) which decreases when $\rm PA_{bar}$ increases. But when the size of the FOV is of the order of the bar size, ϵ is affected by $\rm PA_{bar}$ and then the projections spread over a wide range of anisotropy. The intrinsic ellipticity of the MGE parametrization plays here an important role for the anisotropy recovery.

We made a second test to better understand the effect of the MGE parametrization on a model of barred object. From the same projection we created two different MGE models : the first one is a "free" model with gaussian axis ratios left unconstrained ; for the second one we forced the maximum and the minimum axis ratio as we do know the intrinsic mass distribution. We did not include here the case $\rm PA_{bar} = 45°$ for which the MGE parametrization is forced to be neither flatter nor rounder than the axisymmetric case. As expected, when we forced the axis ratio during the MGE parametrization, the global anisotropy $\beta_z^{\rm JAM}$ recovered was found to be much closer to $\beta_z^{\rm SIM}$

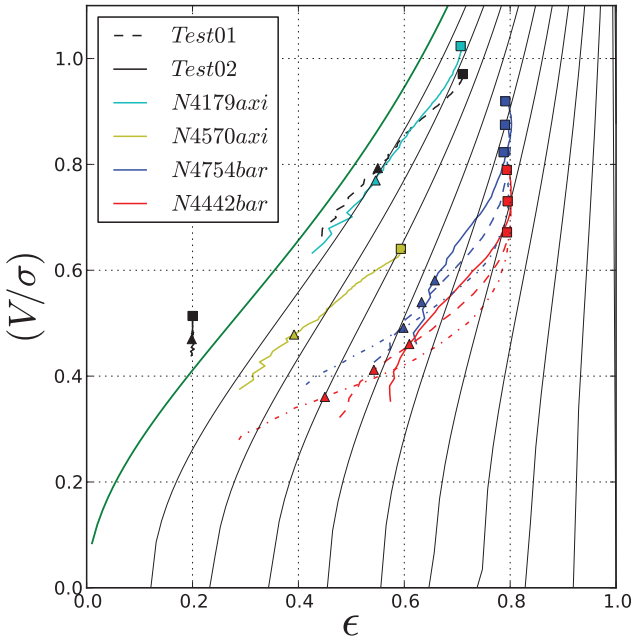

Figure 3.8: Positions of edge-on projections of all models in the $(V/\sigma,\ \epsilon)$ diagram. The two tests models described in Section 3.5.1 are in black. The green line and the thin black solid lines correspond to isotropy and constant anisotropy in the diagram with a step of 0.1 from left to right. The cyan line correponds to $N4179axi$; the yellow one to $N4570axi$; the blue ones to $N4754bar$ and the red ones to $N4442bar$. For barred simulations the solid line refers to $\mathrm{PA_{bar}} = 18°$; the dashed one to $\mathrm{PA_{bar}} = 45°$ and the dash-doted one to $\mathrm{PA_{bar}} = 87°$ (we removed the case $\mathrm{PA_{bar}} = 60°$ for better legibility). The wider FOV is represented by a square and our reference FOV in the present study by a triangle.

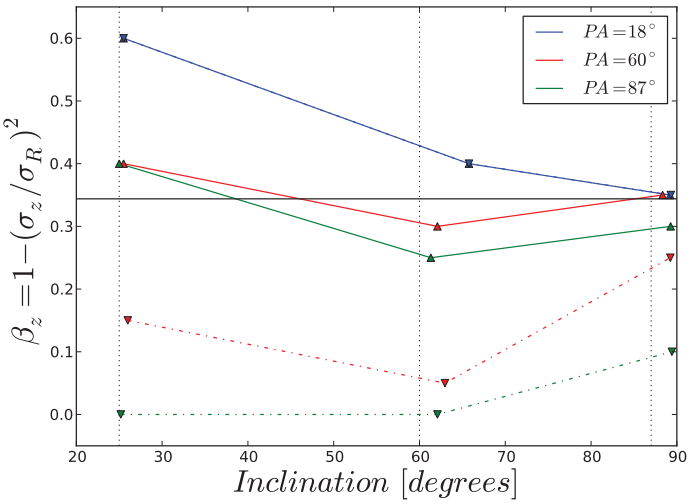

Figure 3.9: Recovered values of the global anisotropy as a function of the projection inclination for two different MGE parametrization of the same model. The color solid lines are the values recovered with a model with forced axis ratio for the MGE parametrization and the dash-dot lines are for a free MGE parametrization (see Section 3.5.1). Note that the blue solid line and the blue dash-dot line are overlaping. The horizontal black line is the value $\beta_z^{\rm SIM}$ computed from the model.

as shown in Fig 3.9. We can then assume that the accuracy in the recovery of the global anisotropy is mainly biased by the MGE parametrization of the photometry.

Unfortunately, we cannot always objectively choose the best deprojected model when we apply the JAM modeling method to real observations. And for barred galaxies the accuracy on β_z will only be improved if we can really see the bar or have strong evidence for its presence.

3.5.2 Recovery of M/L

The Mass-to-Light ratio M/L is the third parameter (after the inclination i and the global anisotropy β_z) computed with the JAM modeling method.

When using the initial conditions, we simply compare the recovered M/L with the input ones. For evolved galaxies we used instead, as our reference, the M/L computed from the direct application of the virial relation $2K + W = 0$ to the simulation particles, where K is the total kinetic energy and W is the total potential energy of our simulations.The relation makes no other assumption that a steady state, and thus provides the natural benchmark against which to compare stationary dynamical models. In general one expects simulations and real galaxies to satisfy the relation quite accurately, so that the virial $M/L_{\rm vir}$ will agree with the input one $M/L_{\rm SIM}$ and no distinction needs to be made. However Thomas et al. (2007) found that $M/L_{\rm vir}$ can differ from the input one at the 5% level, due to non stationarity, and our results agree with theirs. As we are not interested on investigating the stationarity of the model, but only the biases of the modelling method, for maximum accuracy we use as reference $M/L_{\rm vir}$ in all the comparisons which follow.

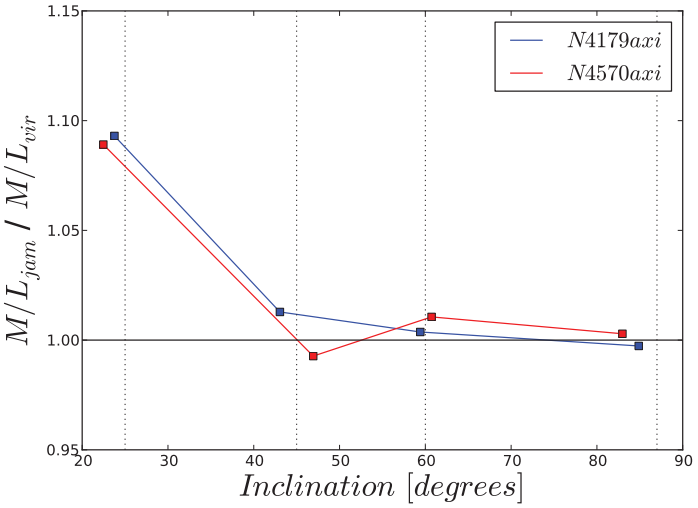

Figure 3.10: Recovered value of M/L for non barred simulations $N4179axi$ and $N4570axi$ as a function of the inclination of projection. In these regular axisymmetric simulations we find an error of 1.5% on M/L (excluding the near face-on projection).

To probe the robustness of our method we applied it to the four Hernquist particle realizations created from the analytic formula of Hernquist (1990). The results both in the recovery of the global anisotropy and the M/L were excellent, with an accurate recovery of β_z and errors on M/L of less than 1.5%. Whilst these simulations are basic and do not reproduce the complexity of a real galaxy, this is a reassuring test of our machinery.

An intermediate case between simple analytic simulations and real galaxies, is the $N4754ini$ model which is just a regular axisymmetric rotating galaxy with a constant anisotropy. Its mass distribution corresponds to a real galaxy but its intrinsic dynamics are simple, as the velocity anisotropy is set to be constant throughout the galaxy. The global anisotropy is well recovered within 0.025 and the mass-to-light ratio is recovered with an error of less than 1.5%. Although unrealistic, this case helps isolate the influence of a variable anisotropy on the results of the JAM modeling method.

We then used the JAM modeling method on $N4179axi$ and $N4570axi$ to explore any systematic bias that may be present *without* the presence of a bar. Results are shown in Figure 3.10 and JAM fitting in Fig. B.1 and Fig. B.2. Figure 3.10 emphasizes that one can expect significant overestimations of M/L up to $\sim 10\%$, when the galaxy is close to face-on. This important fact is illustrated with an analytic test in Fig. 4 of Cappellari et al. (2006) and with the galaxy NGC0524 in Fig. A1 there. Here we confirm it with the present simulations. In what follows we will focus on the higher inclinations. However, one should keep in mind that the M/L of nearly face-on galaxies has to be treated with caution. For $i = 45^\circ$; $i = 60^\circ$ and $i = 87^\circ$ then, we find that in regular axisymmetric cases M/L is recovered with a negligible median bias, and a maximum error of just 1.5%.

Figure 3.11 presents the results of JAM modeling of $N4754bar$ and $N4442bar$. As for axisymmetric cases, we only consider here inclination projections with $i \geq 45^\circ$. For high inclination projections the M/L is recovered within 3% for a $\mathrm{PA_{bar}} = 45^\circ$, which represents the average for

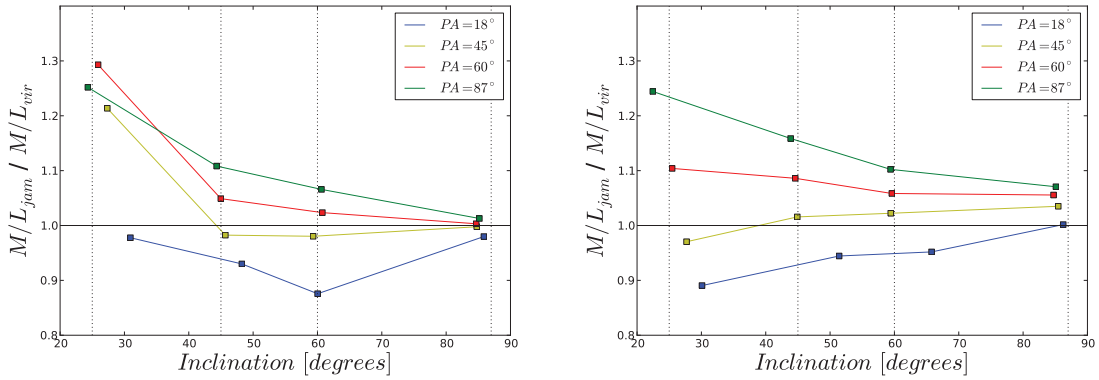

Figure 3.11: Recovered value of M/L for $N4754bar$ and $N4442bar$ as a function of the projection inclination for different values of $\mathrm{PA_{bar}}$.

random orientations. However the bias in the recovery can reach up to 15% in our tests cases. But the main point is that the recovered M/L is correlated with the position angle of the bar, $\mathrm{PA_{bar}}$. The more the bar is seen end-on, the larger the overestimation, due to the larger velocities of the stars moving along the bar, and towards the line-of-sight, with respect to the other directions in the disk plane. The reason is that the presence of a bar produces a peak in the V_{rms} maps which is not present in the purely axisymmetric case (see Figure 3.2). In order to fit this peak, the JAM model tend to larger M/L values. Moreover, the amplitude of the peak increases with $\mathrm{PA_{bar}}$, which explains why the value of M/L_{JAM} also increases with the position angle of the bar. The exclusion of the central regions helps to reduce the bias introduced by the bar in M/L_{JAM}, but in cases where the bar dominates the whole field of view, we cannot expect to get rid of its influence.

The case when the bar is seen side-on ($\mathrm{PA_{bar}} = 18°$) for $i = 45°$; $i = 60°$ and $i = 87°$ is a special configuration for JAM. As the flat bar is deprojected as a flattened disk, following the axisymmetric assumption, the JAM model is unable to reproduce the global shape of the V_{rms} map (see Fig B.4- B.6, Fig B.8- B.10 top left panel). The error on the recovered mass-to-light ratio can be up to $\sim 10\%$. In fact the global shape of the V_{rms} map is dictated by the global anisotropy. The mass-to-light ratio essentially adjusts the fit to the global level of the second velocity moment.

The position of the bar $\mathrm{PA_{bar}} = 45°$ is a useful reference, as it represents the average value for random orientations. As previously mentioned in this case the MGE parametrization is hardly affected by $\mathrm{PA_{bar}}$. In this configuration the error on M/L does not exceed 3%, although the V_{rms} map is not reproduced. Basically for projections with $\mathrm{PA_{bar}} < 45°$ M/L is expected to be underestimated while for projections with $\mathrm{PA_{bar}} > 45°$ it is overestimated.

Then for $\mathrm{PA_{bar}} = 60°$ and $\mathrm{PA_{bar}} = 87°$, the bar produces a vertically elongated structure in projection and an artificially round bulge when deprojected as an axisymmetric system. However the reproduction of the V_{rms} shape is still a hard task for the JAM model (see Fig B.4- B.6, Fig B.8- B.10 right column). A brief investigation pertaining to the influence of the MGE parametrization on M/L_{JAM}, illustrated by Figure 3.12, shows that forcing the flattening of the mass distribution in the JAM model does not really affect M/L_{JAM}, except for $\mathrm{PA_{bar}} = 87°$. For this bar position the accuracy in M/L_{JAM} is increased, but at the same time, as previously mentioned in Section 3.5.1, the accuracy on the recovered global anisotropy is decreased. The prediction of the V and σ fields, are however significantly improved, when forcing q_k, is as already shown in figure 3 of Scott et al.

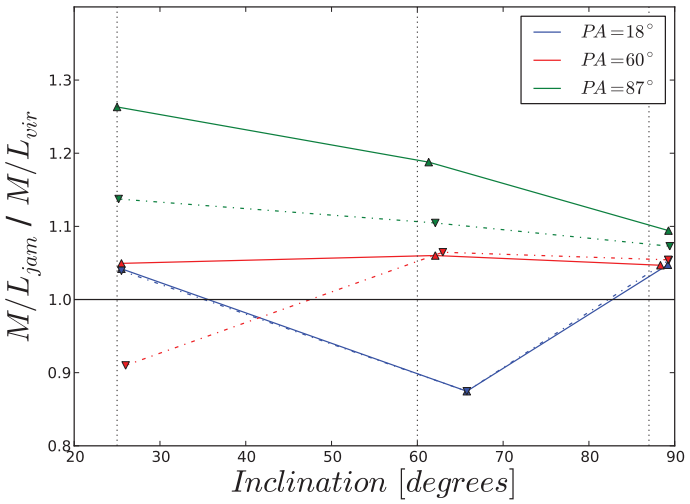

Figure 3.12: Recovered value of the mass-to-light ratio as a function of the projection inclination. The color solid lines are the values recovered with a model with forced axis ratio for the MGE parametrization and the dash-dot lines are for a free MGE parametrization.

(2009).

To sum up, when a bar is present the M/L overestimation with the JAM modeling method is clearly due to the dynamics of the bar and its effect in the projected velocity moments.

To reduce the effect of the bar, one possible solution is to fit the JAM model only to regions where the bar has little or no influence. We therefore investigated the effect of the size of the field of view (FOV) on $M/L_{\rm JAM}$. One could expect that when increasing the FOV further we could minimize the effect of the bar on the fit and thus reach a better accuracy in the recovering operation. To test this, we increased the FOV of our mock data and repeated the JAM fitting procedure (the MGE parametrization was not affected as it is anyway done on a projection of the simulations with a very large field of view). Figure 3.13 illustrates $M/L_{\rm JAM}$ as a function of the size of one side of the FOV normalized by the size of the bar for $N4754bar$. We find that, as expected, the FOV plays a role in the recovered values. When the size of the FOV exceeds the bar size $\Delta M/L$ decreases and seems to tend to a limit value. This is expected as we cannot totally get rid of the effect of the bar in the $V_{\rm rms}$ maps. In our study, the typical fitted field of view is quite comparable to the size of the bar itself, meaning that our previous results are close to the worst case scenario. The relative size of the bar with respect to the size of the field of view is an important ingredient for the recovery of the mass-to-light ratio.

To conclude, when modeling a barred galaxy assuming an axisymmetric mass distribution, the M/L is on average (at $\rm PA_{bar} = 45°$) still well recovered. It can,however, be overestimated, when the bar is parallel to the line-of-sight, or overestimated, when the bar is orthogonal to the line-of-sight, by up to 15% (in our tests). The amplitude of these errors mainly depend on the position angle of the bar $\rm PA_{bar}$, but also on the size of the FOV. Excluding the most central parts and increasing the FOV would naturally tend to reduce the influence of the bar without removing the error on M/L entirely.

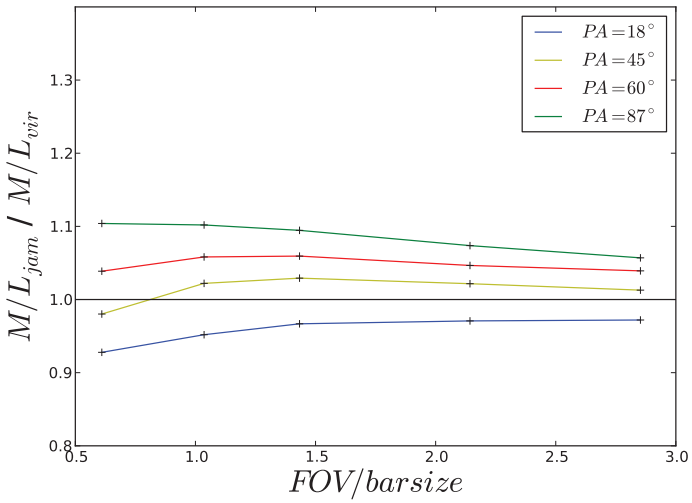

Figure 3.13: Effect of the FOV on the accuracy of the recovered M/L of $N4754bar$ projected with $i = 60°$. The $x - axis$ correspond to the size of the side of the field of view normalized by the size of the major axis of the bar determined in Section 3.4.2.

3.6 Conclusion

This paper focuses on the study of the possible biases in the M/L and anisotropy determination for barred simulations, when using axisymmetric dynamical models. We also extend previous studies (Thomas et al., 2007) for axisymmetric simulated galaxies that better resemble observed fast early-type rotators which constitute the large majority of the gas-poor population in the nearby Universe (see Paper II and Paper III). We do this by generating N-body simulations of objects with properties similar to observed galaxies, both with and without bars. These are projected at various viewing angles and used to generate mock observations that closely resemble real data. These data are then fed into the JAM modeling machinery as for real data, the difference being that the intrinsic values of the free JAM model parameters (i, β, M/L) are known for the simulated data set.

The errors in the recovered inclination increase with inclination due to the fact that, as previously noticed, the models predictions change gradually with the intrinsic axial ratio of the MGE models. This implies that for nearly face-on inclinations, where the intrinsic axial ratio of the models change rapidly, the inclination is formally constrained to a fraction of a degree. This formal accuracy is, however, compensated by a broader degeneracy in the mass deprojection, leading to a small *negative* bias in the inclination. In practice, for the four simulations we constructed, the errors never exceeded 5°.

We confirm previous results that the M/L can be recovered within a few percent when the simulated galaxies are nearly axisymmetric, except for nearly face-on view, for which the M/L can be significantly overestimated. The global anisotropy β_z can be difficult to recover, especially at low inclination (near face-on) due to the inclination-anisotropy degeneracy. This degeneracy implies a significant uncertainty on β_z at low inclination, but a smaller error at high inclination. The global anisotropy is primarily influenced by the flattening (or the roundness) of the MGE parametrization of the projected luminosity. In the case of regular axisymmetric objects, the main issue is the

intrinsic mathematical degeneracy of the luminosity deprojection incurred during the MGE fitting step of the method. This results in small deviations of the recovered global anisotropy from the value computed from the numerical simulations: β_z is well recovered.

When a bar is present, the mass deprojection becomes the main uncertainty in the models. The deprojected axisymmetric model will be naturally different from the true non-axisymmetric barred distribution and will change as a function of the observed PA. Consequently the predicted $V_{\rm rms}$ of the models, as well as the corresponding best fitting β_z will change as a function of the PA and can be quite different from the true axially-averaged value.

The mass-to-light ratio is less sensitive to the MGE parametrization than the global anisotropy, but it is biased due to the intrinsic dynamics of the system we want to model. We find that M/L is mainly influenced by the position of the bar and the size of the field of view. The error depends upon the position angle of the bar $\rm PA_{bar}$ and can be up to 15%. Including only regions far from the bar allows a reduction of the error, but cannot generally avoid it completely.

Our study provides an estimate of the M/L error that can affect the determination of dynamical M/L via axisymmetric models, and in particular using the JAM method. The large variety of possible shapes, sizes and orientations of bars in galaxies, each with specific dynamics, prevents us from quantifying the exact errors made for individual galaxies. One should also keep in mind that our study is done on simulations of relatively weak bars. Therefore, the error on the estimated M/L when modelling galaxies exhibiting stronger bars is expected to be larger. The objects studied here are still representative ATLAS$^{\rm 3D}$ fast rotators, this study therefore providing clear guidelines when applying axisymmetric modelling to such large samples.

Chapter 4

Secular bar driven evolution of ETGs

4.1 Introduction

It is recognized that bars are an important motor of galaxy secular evolution (see Chapter 1). Their presence implies an important redistribution of angular momentum and matter in the host. Subsequent modifications in the stellar and gas dynamics strongly drive the evolution of the galaxy.

Bars are known to efficiently redistribute mass and angular momentum. Both theory (e.g. Binney & Tremaine, 2008; Sellwood & Wilkinson, 1993; Lynden-Bell, 1979, 1996) and N-body simulations (e.g. Sellwood, 1981; Sparke & Sellwood, 1987; Pfenniger & Friedli, 1991; Athanassoula, 2003) show that bars transfer angular momentum to the outer disk. Due to their orbital structure their presence lead to an important radial mixing. Brunetti et al. (2011) for example shows that the radial diffusion is more important close to corotation, but did not examine its impact on a subsequent metallicity or age redistribution.

Numerical studies have also shown that a bar naturally flattens pre-existing metallicity gradients via its dynamical influence on the system (Friedli et al., 1994). More advanced studies used chemodynamical simulations to analyze the age distribution of stellar populations and dynamical secular evolution of barred galaxies (Michel-Dansac & Wozniak, 2004; Wozniak, 2007). It has been found that the end of the bar close to the corotation and the central part represent location of low-age regions.

Recent observational studies (Pérez et al., 2009; Pérez & Sánchez-Blázquez, 2011; Sánchez-Blázquez et al., 2011) have investigated "*the influence of bars in the formation of ETGs through the analysis of ages and metallicities derived from stellar absorption line-strength indices*". In these studies it is shown that bars fall in three different categories : (i) bar with negative metallicity gradients made of a mean young/intermediate population (<2Gyr), (ii) Bar with null metallicity gradients in agreement with Wozniak (2007), (iii) bar with a positive metallicity gradient composed of older mean ages stellar population. No significant correlation between the gradient characteristics and bar properties were found in these observational studies. Moreover, so far, only the second family has actually been reproduced in detail with numerical simulations.

We present here a preliminary study of the influence of a bar-driven evolution on the mass and metallicity distribution in barred ETGs. We aim at quantifying the impact of a bar on the mass distribution and also on metallicity and ages gradients. We have performed high resolution N-body simulations covering a variety of mass distributions, bar lengths and strengths with and without

gas and star formation in order to correlate bar properties with subsequent effects.
We first present the specifics of the simulation code and the method adopted to build up a coherent sample for this study. Properties of barred and unbarred models performed are also given in this section. Then we investigate the mass and metallicity redistribution due to the presence of a bar in these simulations. In agreement with previous studies we show how a bar flattens a pre-existing gradient. Correlations between the radial mixing, the metallicity redistribution and the bar properties are presented here. In the last section we explain the need to include star formation recipes to explain the variety of gradients that are actually observed.

4.2 Goal and strategy

Our goal is to understand the effect of a bar driven evolution of an isolated early-type galaxy on metallicity and ages gradients. To investigate this issue we have performed a number of high resolution N-body simulations. We have created a sample of numerical models covering a variety of mass distributions (from axisymmetric to barred systems) with or without gas. The method applied to build this sample is described hereafter.

4.2.1 Selection

The initial mass distribution of our numerical models is meant to mimic the complexe structure of observed galaxies. We therefore chose to use the Multi Gaussian Expansion parametrization (MGE) (see Emsellem et al., 1994a; Cappellari, 2002) of a few galaxies picked among the 260 ETGs of the ATLAS^{3D}sample (see Cappellari et al., 2011a).
As we want to model barred galaxies, we focused on well classified lenticular galaxies (S0) resulting in a subsample of 175 targets. In a second step, we made a selection based on the SDSS pictures of the galaxies used to create MGE models. Every galaxy with some dust lanes or blue rings, a bright star on the foreground or any unusual feature (e.g. CCD defect were excluded). These first criteria ensured that we chose MGE parametrization based on clean pictures of S0 and S0B presenting no specific obstacle for the MGE procedure. We also decided to exclude galaxies with small apparent Re (compared to the field-of-view) in order to have well sampled photometry. This last point was more of an extra precaution than a real issue (only a few galaxies were excluded).
The MGE parametrization of the remaining 15 galaxies were kindly provided by Nicholas Scott. Details on the fitting method can be found in Scott et al. (2009) (see also Chapter 3). The models are all based on SDSS r-band images.
The four galaxies used in Chapter 3 (i.e. NGC4179, NGC4442, NGC4570 and NGC4754) are included in this sample of 15 candidates for N-body simulations. Colour images of these selected galaxies are shown in Fig 4.1

We checked the distribution in mass for this sample of our MGE parametrization but also their position in a Mass-Re diagram (see Fig 4.2). In this latter figure all 260 ATLAS^{3D}galaxies are provided for comparison. We can see that our sample of models span a reasonable range of mass and Re within the ATLAS^{3D}distribution.

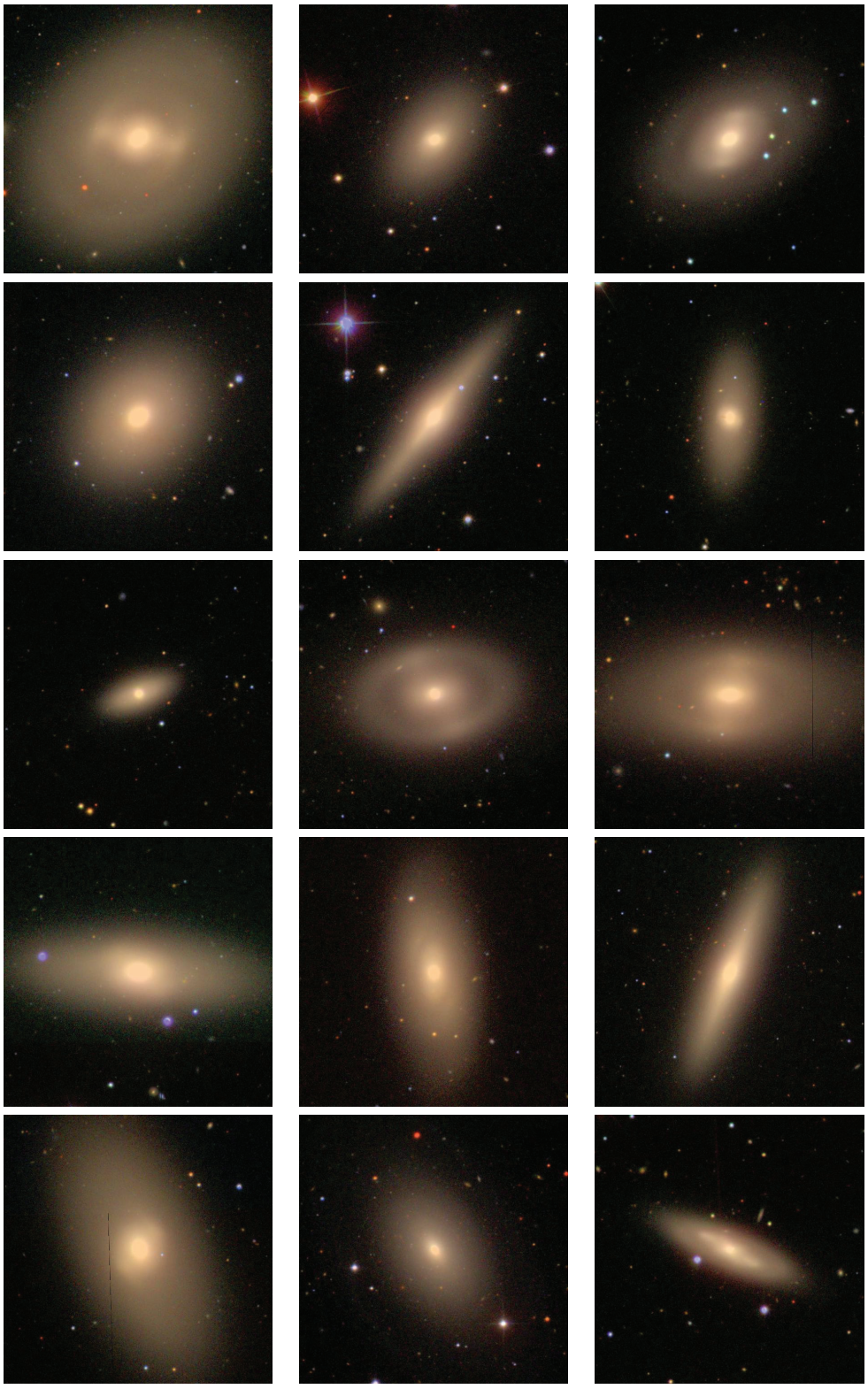

Figure 4.1: SDSS r-bans images (4.8 × 4.8 arcmin) of the 15 galaxies selected to set up initial conditions. From left to right and top to bottom : NGC0936 ; NGC2880 ; NGC2950 ; NGC3998 ; NGC4179 ; NGC4233 ; NGC4255 ; NGC4340 ; NGC4371 ; NGC4442 ; NGC4503 ; NGC4570 ; NGC4754 ; NGC5582 ; NGC5864.

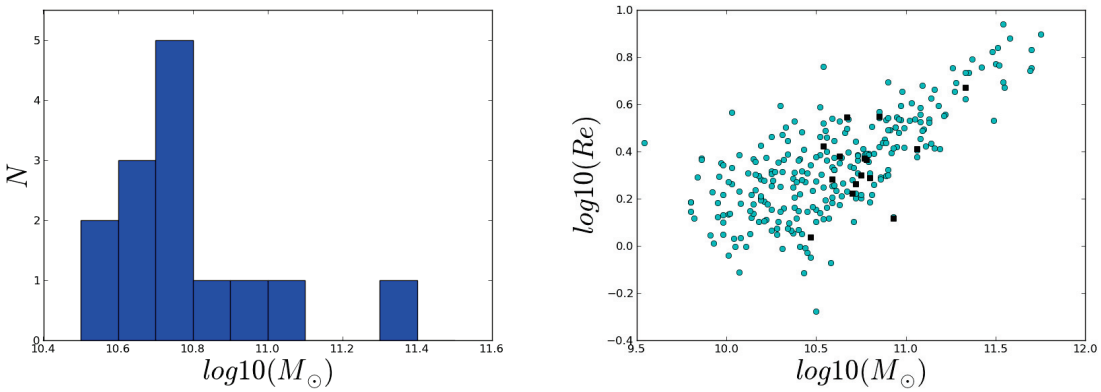

Figure 4.2: The left figure represents the distribution in mass of the MGE parametrization used to set up initial consitions. The right figure shows the position of the MGE models (black squares) in a Mass-Re diagram compared to the ATLAS^{3D}sample.

4.2.2 Dark Matter halo

To these MGE parametrization of the luminous matter, we added a dark matter halo with a spherical pseudo-isothermal density distribution :

$$\rho(r) = \frac{\rho_0}{1 + (r/r_c)^2} \tag{4.1}$$

where ρ_0 is the central density of the sphere and r_c is the core radius.
The shape and profile of the dark matter halo are usually constrained by using, e.g. kinematic tracers beyond the disk such as extended HI disks (e.g. Weijmans et al., 2008), the orbits of satellite galaxies, or weak lensing. None of the above constraints were available for our selected galaxies. We therefore decided to constrain the mass distribution of the dark matter halos with the two following empirical criteria :

- The circular velocity curve of the system beyond $2R_e$ shall remain roughly flat (e.g. Rubin et al., 1980).
- The dark matter mass fraction inside R_e shall not exceed 30% of the total mass (e.g. Cappellari et al., 2006).

Once the shape of the dark matter halo was defined, we built its a MGE parametrization and included the gaussians in the original parametrization (see Fig 4.3 for an overview). In simulations, the dark matter halos are made of particles and are therefore "live" dark matter halos. The number of particles in this halo has been calculated such that the ratio between the mass of a stellar particle and a dark matter particle is between 5 and 6. This is a good balance between saving computational time and preventing large effects from e.g. two-body interactions.

4.2.3 Simulations

All simulations have been performed using the *PM/sticky particle* code described in Chaper 2. The grid side size is 80kpc with two levels of refinement and in the central parts the resolution

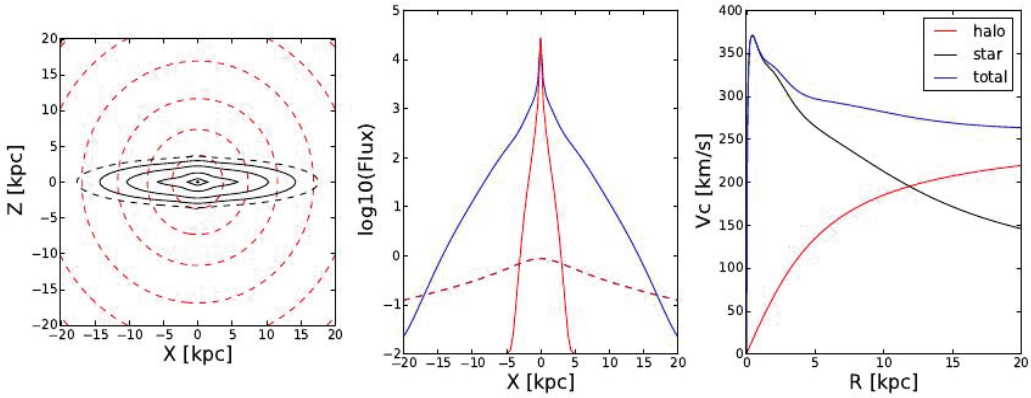

Figure 4.3: On the left panel the black solid lines correspond to stars isophotes while the dashed red lines represent the dark matter halor isodensities. On the middle panel blue and red lines represent the major-axis and minor-axis luminosity profiles respectively while the dashed line represent the halo profile. The right panel shows the circular velocity for the stellar component, the dark matter halo and the combination of both.

reaches 48pc. In order to save CPU time it was decided not to run simulations from two initial mass distributions which appeared too similar. Thus from the 15 MGE models we discarded 3 more galaxies and only 12 were then effectively used. From these latters we have performed two sets of numerical models.

The first one consists in high resolution simulations of the secular evolution of isolated galaxies containing only stars and dark matter. We also added to this set of models the simulations performed in Chapter 3 named N4179axi, N4442bar and N4754bar. In the second set, a gas component has been added in the initial conditions (in the disk) and star formation has been switched on. Both sets include numerical models which evolve in either axisymmetric or barred lenticulars. A quick analysis of the stability of the disk using Toomre's criterion allowed to distinguish MGE parametrizations which are likely to produce a bar or not. More details are given in the following section.

4.3 Models including stars and dark matter

As previously mentioned, in addition to the four models performed in Chapter 3, eleven simulations containing only stars and dark matter were run to make a sample of fifteen galaxies. Five are axisymmetric lenticular models while the ten left are barred lenticulars models. These models did not include any gas component and had (therefore) no star formation. For all simulations we used 4.10^6 particles to model the stellar component while the number of dark matter particles were set according to Section 4.2.2 which depend on the mass of each model dark matter halo. We simulated the evolution over 2 Gyr. The method to set up the initial particle positions and velocities is the same as in Chapter 3 and is applied to both the stellar and the dark matter components. A cut in the particle positions is performed at a radius of 50kpc.

Name	$M_\star$ $[10^{10} \cdot M_\odot]$	R_e [kpc]	halo
N2880axi	3.89	1.72	yes
N4179axi	5.25	1.70	yes
N4179axib	8.98	1.43	no
N4233axi	11.48	2.40	yes
N4255axi	5.01	1.41	yes
N4570axi	5.62	1.83	yes

Table 4.1: Table summarizing the stellar mass $M_\star$ and effective radius R_e of the axisymmetric numerical models without gas. N4179axib is included from a previous study (see Chapter 3).

4.3.1 Axisymmetric models

Initial conditions

Models labelled "axisymmetric" in the present study are models presenting no non-axisymmetric features in their final state. The MGE parametrization used to set up initial conditions are extracted from the SDSS r-band images of NGC2880, NGC4179, NGC4233, NGC4255 and NGC4570. The previous simulation of NGC4179 done in Chapter 3 has also been added even though it does not include a dark matter halo. From the mass distribution the initial velocities were computed assuming an isotropic velocity dispersion (i.e. $\sigma_R = \sigma_z = \sigma_\theta$).

Properties

From the final state of the simulation we have computed the effective radius R_e and the total mass of the system $M_\star$. This mass can differ a little from the mass of the original MGE distribution because of the radial cut when setting up initial positions but also because of particles escaping the grid during the simulations. We thus considered only particles inside a radius $R \leqslant 40$ kpc. Table 4.1 summarizes some properties of our five axisymmetric models in the final state.

Such simulations of S0s are used as references to interpret simulations of barred galaxies. Indeed, phenomena that would appear in both types of simulations should not be due to the presence of the bar and then could be attributed to physical processes present in both cases or to numerical issues.
We notice that N4255axi presents transient spiral arms during the first 1.25Gyr of evolution. Although this may influence some results concerning the stellar diffusion we did not exclude it from the axisymmetric sub-sample.

4.3.2 Barred models

Initial conditions

The MGE parametrization used for the barred models are extracted from the images of NGC0936, NGC3998, NGC4179, NGC4233, NGC4442, NGC4754, NGC5582, NGC5864. Except for NGC4179 and NGC4233, all MGE models are already subject to bar instability and then we set an initial isotropic velocity dispersion. NGC4179 and NGC4233 were initially aimed to produce axisymmetric models but we also forced the disk to be dynamically cold to force the formation of a bar. This

was done by applying the following velocity dispersion relations :

$$\frac{\sigma_R}{\sigma_\theta} = 2.0 \tag{4.2}$$

$$\frac{\sigma_z}{\sigma_R} = \sqrt{1-\beta_\epsilon} \tag{4.3}$$

$$\tag{4.4}$$

where $\beta_\epsilon = 0.6 \cdot \epsilon$ with ϵ the intrinsic galaxy ellipticity (Cappellari et al., 2007). The reason to force the bar formation for these two axisymmetric models is to compare the evolution of a S0 and a S0B from the same initial density distribution.

Properties

In all simulations of barred galaxies the bar forms during the first ∼150Myr. As for the axisymmetric numerical models we have computed the stellar mass $M_\star$ and the effective radius R_e for the final state of our simulations. In addition, we have also computed the bar length L_{bar} (actually the semi major-axis), its pattern speed Ω_p and its strength Q_{bar}.

The length of the bar has been computed as in Chapter 3 using an ellipse fitting of the face-on projected isophotes.

To compute the bar pattern speed we used the classical Tremaine-Weinberg method (Tremaine & Weinberg, 1984) :

$$\Omega_p = \frac{\int_{-\infty}^{\infty} \mathrm{d}x \Sigma v_y}{\int_{-\infty}^{\infty} \mathrm{d}x \Sigma x} \tag{4.5}$$

where $v_y = v_{los}/\sin(i)$ with v_{los} is the line-of-sight velocity, Σ is the surface brightness and x being the line of nodes. To apply this method to our simulations we created mock observations by projecting particles such that the galaxy is seen with an inclination $i = 45°$ and the bar has a position angle $PA_{bar} = 45°$ relative to the galaxy major-axis. Line-of-sight velocities are then computed for each pixel and the integral in previous equation becomes a discrete summation over the pixels.

The bar strength has been computed with the method described in Buta & Block (2001). This method uses the bar torque defined in Combes & Sanders (1981) to classify bar strengths; given the potential in the disk plane $\Phi(R, \theta)$:

$$Q_T(R) = \frac{F_T^{max}(R)}{\langle F_R(R) \rangle} \tag{4.6}$$

where $F_T^{max}(R) = [\partial\Phi(R,\theta)/\partial\theta]_{max}$ is the maximum amplitude of the tangential force at radius R and $\langle F_R(R) \rangle = R(\mathrm{d}\Phi_0/\mathrm{d}R)$ is the mean axisymmetric radial force with Φ_0 the axisymmetric average of Φ. In our numerical models we can compute directly the gravitational potential from the particle positions. We nonetheless restricted the computation to particles located $\pm 0.5kpc$ from the equatorial plane of the galaxy. Then as suggested in Buta & Block (2001), we divide the simulations in four quadrants defined by the bar major-axis and minor-axis. In the quadrant j we compute the bar torque Q_{bar}^j and then compute the final bar torque :

$$Q_{bar} = \frac{1}{4} \sum_{j=1}^{4} Q_{bar}^j \tag{4.7}$$

Name	$M_\star$ $[10^{10} \cdot M_\odot]$	R_e [kpc]	L_{bar} [kpc]	Q_{bar}	Ω_p [km.s^{-1}.kpc^{-1}]	halo
N0936bar	18.21	4.20	2.49	0.66	118.20	yes
N3998bar	8.51	1.18	2.23	0.28	87.893	yes
N4179bar	5.25	1.65	0.30	0.06	83.114	yes
N4233bar	11.48	2.28	0.76	0.24	100.56	yes
N4442bar	6.31	1.98	2.51	0.94	85.023	yes
N4442barb	21.26	2.30	2.95	0.20	113.74	no
N4754barb	12.17	2.76	2.38	0.27	72.518	no
N5582bar	7.08	3.68	2.40	0.31	54.455	yes
N5864bar	4.68	2.70	5.02	0.65	29.354	yes

Table 4.2: Table summarizing the stellar mass and effective radius of the barred numerical models without gas. N4442barb and N4754barb are included from a previous study. N4233 presents a double bar structure, so that values given here are for the inner structure.

Name	L_{bar}	IILR	OILR	UHR	CR	OLR
N0936bar	2.49	–	–	1.78	2.56	4.04
N3998bar	2.23	0.84	0.95	2.34	3.23	4.81
N4179bar	0.30	–	–	1.79	2.65	3.97
N4233bar	0.76	–	–	1.97	2.78	4.02
N4442bar	2.51	–	–	1.92	2.67	4.20
N4442barb	2.95	–	–	2.48	3.32	4.98
N4754barb	2.38	0.74	1.30	2.74	3.76	5.76
N5582bar	2.40	0.78	1.12	2.50	3.53	5.55
N5864bar	5.02	1.04	1.57	3.97	5.16	7.22

Table 4.3: Table summarizing the size of the bar semi major axis and the position of the ILRs, the UHR, the CR and the OLR in barred models. The unity for all values is the kiloparsec [kpc].

Properties of the barred numerical models are given in Table 4.2 It includes also the two models performed for the previous study of Chapter 3. It is important to notice that this sample of barred ETGs covers a range of bar length and strength. This should allow us to find correlations between the bar properties and its effect on the mass and metallicity distributions.

From the particle positions in the final state of the simulations we have computed the azimuthally averaged gravitational potential to derive the frequency Ω and the epicyclic frequency κ. Associated with the pattern speed we have extrapolated the position of the inner Lindblad resonances (ILRs) if any, the ultra harmonic resonance (UHR), the corotation (CR) and the outer Lindblad resonance (OLR). Positions of these resonances for all the barred models are given in Table 4.3. One notices that, we have two inner Lindblad resonances (which allows the existence of orbits from the x_2 family) in N3998bar, N5582bar, N5864bar and N4754barb.

A double barred case

While analysing our N-body simulations it appeared that N4233bar clearly presented a double-bar structure. A visual inspection of the snapshots revealed that the inner small bar formed first in $\sim 100Myr$ while the second and longer one appears around $\sim 1100Myr$. The result from the

Name	M_{tot}	R_e	initial gas fraction	final gas fraction	L_{bar}	Ω_p	Q_{bar}
N2880axisf	4.13	1.85	5.95	0.34	Ø	Ø	Ø
N4179axisf	5.60	1.81	6.32	0.19	Ø	Ø	Ø
N4233axisf	13.0	2.72	5.79	0.64	Ø	Ø	Ø
N5864axisf	5.26	3.47	5.76	0.91	Ø	Ø	Ø
N3998barsf	9.33	1.38	5.16	0.08	2.49	104.56	0.96
N4442barsf	6.71	1.97	6.04	0.25	2.55	88.78	0.87
N4570barsf	5.98	1.86	6.04	0.32	2.90	76.65	0.77
N4754barsf	6.48	2.60	7.00	0.45	2.43	68.69	0.93

Table 4.4: Table summarizing the basic properties of the numerical models including gas and star formation. The four first ones are the axisymmetric models while the four last ones develop a bar during their evolution. The total mass M_{tot} includes stellar and gas particles. Units are the same as in Table 4.2. The gas fraction is given in percent.

Tremaine-Weinberg is then biased as each bar has its own pattern speed. By restricting the field of view used to compute Ω_p we assumed that our estimate is valid for the smallest bar pattern speed. All values given in Table 4.2 for N4233 are then related to the inner small bar.
The presence of this double bar structure offers the opportunity to study its formation through secular evolution. Indeed, although this structure has often been observed (e.g. Wozniak et al., 1995; Friedli et al., 1996; Jungwiert et al., 1997; Laine et al., 2002) only few numercial studies have been conducted to study its formation and consequence on its host system (e.g. Debattista & Shen, 2007) (see Erwin, 2011, for a review on this topic). A more detailed study of the simulations is ongoing in collaboration with Dr Witold Maciejewski from the Astrophysics Research Institute in Liverpool John Moores University. The goal is to understand how the double bar formed and how we can recover properties for both bars when observing such structures.

4.4 Models including gas and star formation

4.4.1 Initial conditions

Even a small amount of gas can significantly affect the dynamics of a disk galaxy because of its dissipative nature. The star formation history will also obviously affect the metallicity distribution. It was then crucial, in addition to the previous simulations, to run a number of simulations including gas (and star formation).
We used the original MGE parametrization of NGC2880, NGC3998, NGC4179, NGC4233, NGC4442, NGC4570, NGC4754 and NGC5864, to which we added a gas component. The gas has been added as a disk represented by a single gaussian with $\sigma \sim R_e$ in our MGE models. The intensity of the gaussian was chosen such that the gas mass fraction does not exceed 6% of the total mass in the initial conditions. Details of the numerical models including gas and star formation are given in Table 4.4.

The method to set up initial gas particles positions is the same as for stellar and dark matter particles. The gas disk is rotating and its velocity dispersion is isotropic and very low (a few km/s at start).
Due to computational time constraints the number of particles has been revised and all simulations

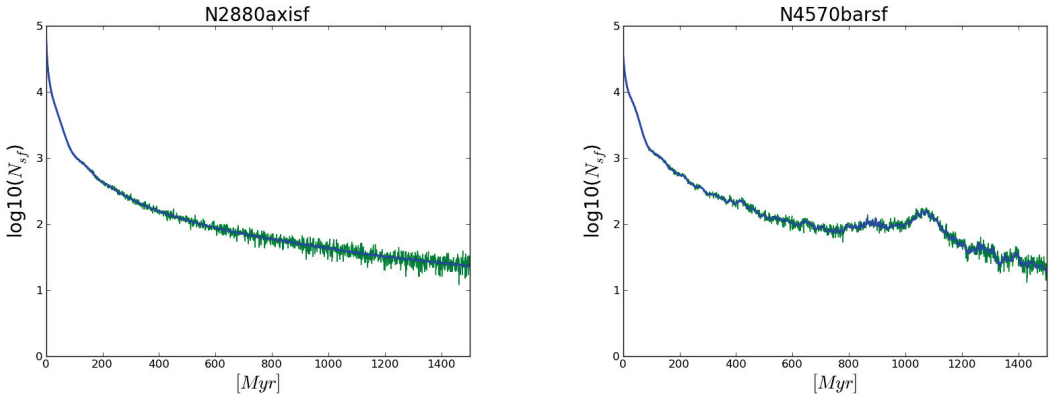

Figure 4.4: Star formation rate in N2880axisf (left) and in N4570barsf (right) with N_{sf} the number of stars formed between two time steps. The green line is an instant star formation rate and the blue line represents the smoothed value.

with gas have $3 \cdot 10^6$ stellar particles, $3 \cdot 10^6$ dark matter particles and $1 \cdot 10^6$ gas particles (initial conditions). Moreover, we limited the simulated evolution time to 1.5Gyrs for the same reason. This allowed us to run several simulations on a short time scale. Properties of the runs are given in Table 4.4.

4.4.2 Axisymmetric models

We classified as "axisymmetric" models simulations which do not show a bar structure even though transient spiral arms can appear. Four out of the eight runs fall into this category : N2880axisf , N4179axisf, N4233axisf and N5864axisf.
We observe in all cases the formation of weak transient spiral arms not present in their corresponding runs without gas (i.e. N2880axi, N4179axi, N4233axi and N5864bar). This is due to the dissipative property of the gas component which tends to make the disk more unstable. These spiral arms are also clearly seen in the new stellar population. Nonetheless, no bar appears in any of these numerical (axisymmetric) models.
The left panel in Fig 4.4 shows the star formation rate from T=0Gyr to T=1.5Gyr for N2880axi. We see that for typical axisymmetric lenticulars the star formation rate decreases regularly with time.

4.4.3 Barred models

At the end of the derived evolution N3998barsf, N4442barsf, N4570barsf and N4754barsf have developed a bar structure. Except for N4570barsf, the bar appears within the first $\sim$ 100Myr and lasts until the end of the simulation. For N4570barsf the disk remains stable over the first 925Myr and the bar only appears between 0.95Gyr and 1Gyr. When computing properties summarized in Table 4.4 we used all stellar particles at T=1.5Gyr, including the original $3 \cdot 10^6$ stellar particles and all the new ones formed during the evolution from gas.
As expected, in all runs, once the bar appears, gas in the bar region tends to be driven towards the central region of the galaxy. The star formation is then significantly enhanced in that region.

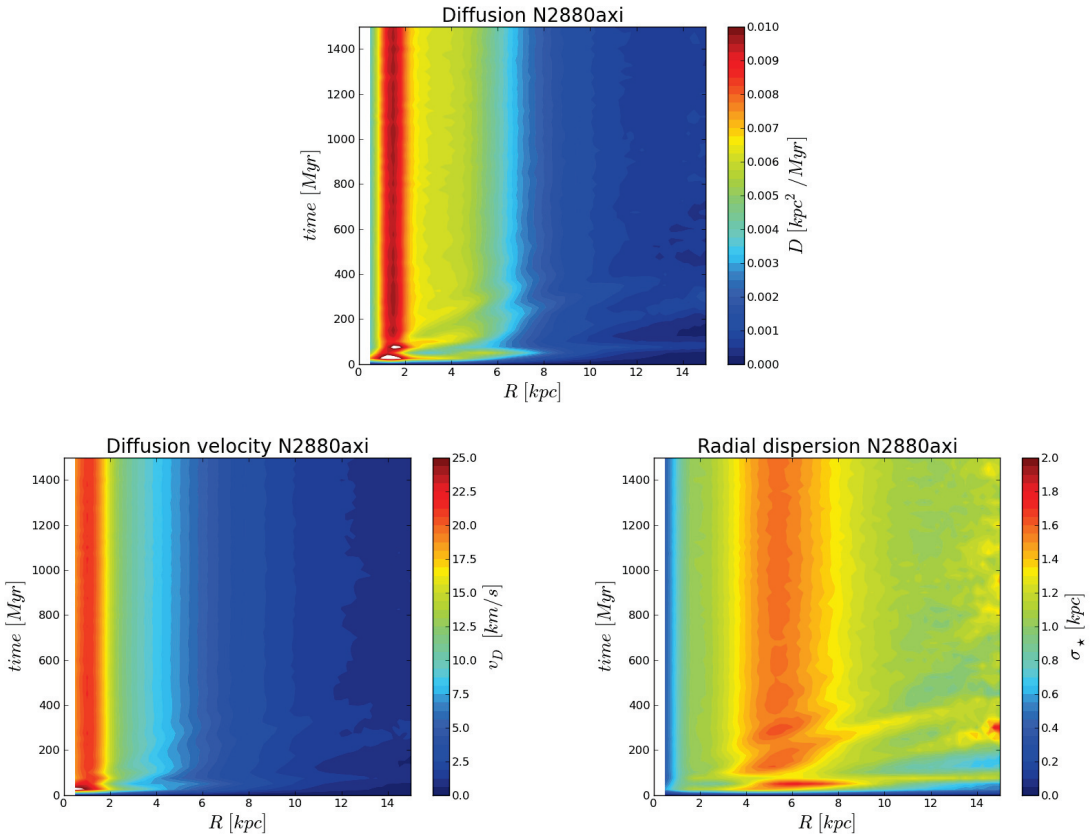

Figure 4.5: Time evolution of the diffusion coefficient D (top), the dispersion velocity v_D and the radial dispersion $\sigma_\star$ profiles.

A quick analysis confirms that, as expected, most of the star formation occurs in the bar region. Outside the corotation the gas exhibits spiral arms.
The formation of the bar has an influence on the star formation rate as shown in Fig 4.4 (right panel). We notice a significant increase of the star formation activity right after the bar formation (∼1 Gyr).

4.5 Mass and metallicity redistribution

4.5.1 Mass redistribution

The presence of a bar is an efficient driver of mass redistribution. To investigate the strict effect of the bar potential in this redistribution we have computed every 25Myr diffusion parameters which are the *diffusion coefficient* D, the *diffusion velocity* v_D and the *radial dispersion* $\sigma_\star$ along radius. We base our study on the previous work done by Brunetti et al. (2011) even though we adopt a different computational method.

We first compute $\sigma_\star(R)$ and then derived the other quantities. The radial dispersion is computed along radii every 25Myr in our simulations. At a given radius R at time t we select particles with

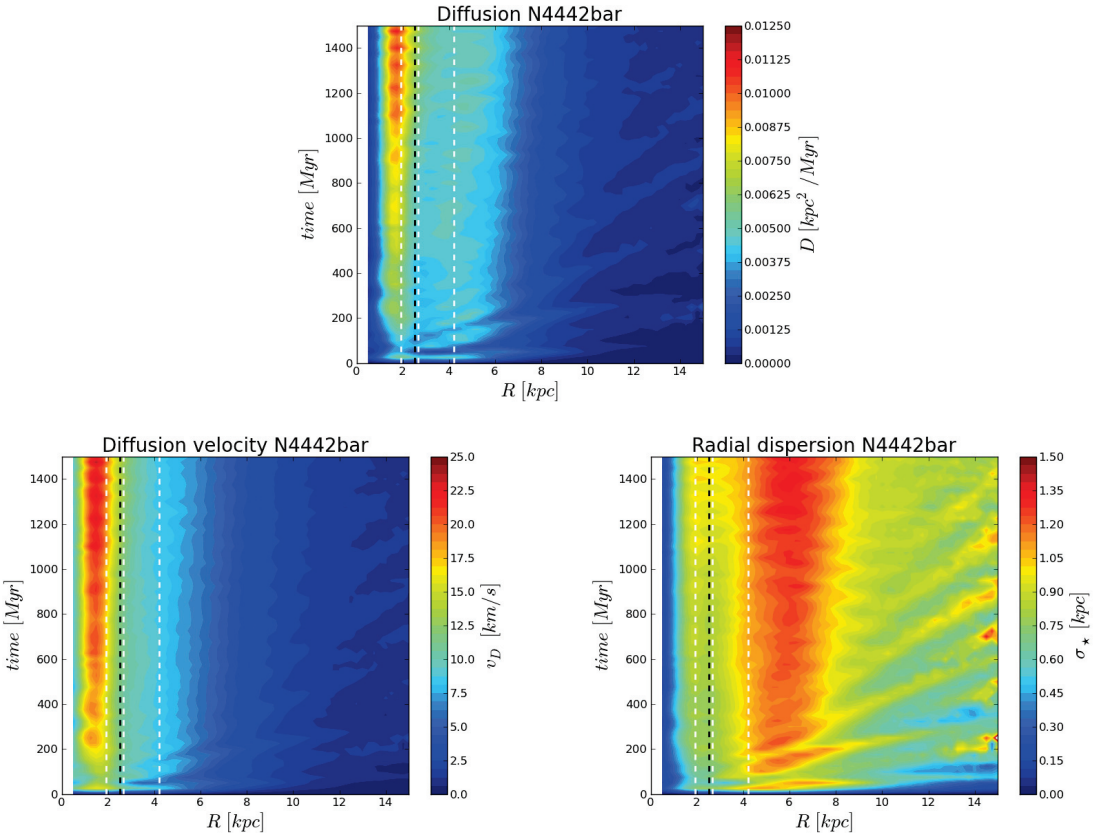

Figure 4.6: Same as Fig 4.5 for N4442bar. The black dashed line represents the end of the bar while the white dashed lines represent the UHR, CR and OLR (from left to right).

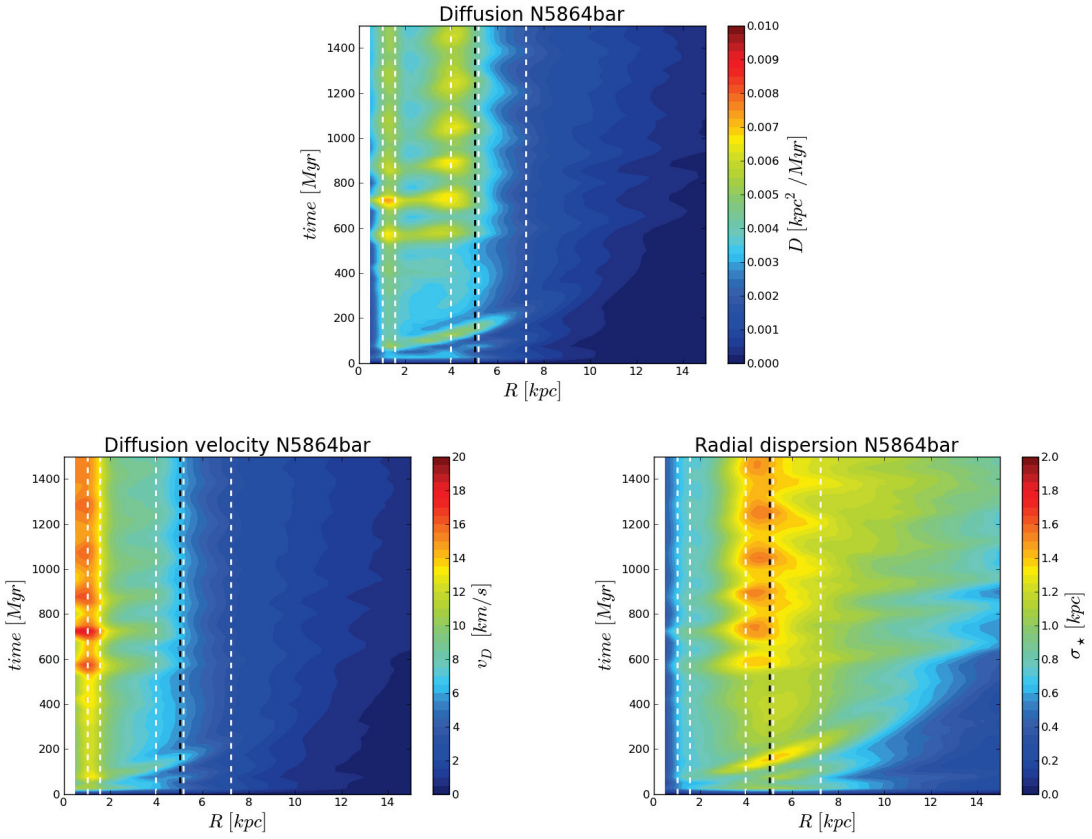

Figure 4.7: Same as Fig 4.5 for N5864bar. The black dashed line represents the end of the bar while the white dashed lines represent the IILR, OILR, UHR, CR and OLR (from left to right).

a position $R - 0.25 < r \leqslant R + 0.25$ in kpc and we calculate their radial standard deviation $\varsigma_{\star t}(R)$ from R. As particles can be followed through time in our simulations, we compute at $t + 25$Myr the radial standard deviation of the same previously selected particles. The radial dispersion at a time T is then given by $\sigma_{\star T}(R) = \sqrt{\varsigma_{\star T}(R)^2 - \varsigma_{\star (T-25)}(R)^2}$.
The diffusion coefficient D and the diffusion velocity v_D are then derived with :

$$D(R) = \frac{\sigma_\star(R)^2}{2 \cdot T_{rot}(R)} \tag{4.8}$$

$$v_D(R) = \frac{\sigma_\star(R)}{T_{rot}(R)} \tag{4.9}$$

where $T_{rot}(R)$ is the rotation period which is derived from the average axisymmetric gravitational potential $\Phi_0(R)$.

Figures 4.5, Fig 4.6 and Fig 4.7 shows the time evolution of D, v_D and $\sigma_\star$ with radius for one axisymmetric model (N2880axi) and two barred models (N4442bar and N5864bar). Similar figures can be found in Appendix C for all numerical models. Computated points are linearly spaced in radius every 0.25kpc and in time every 25Myr.
We first notice horizontal stripes in all figures during the first 100Myr in the diffusion maps. These features are actually due to the relaxation of the model. Indeed, initial conditions are not exactly at equilibrium and thus simulations need some time to reach it (typically $\sim$ 100 Myr). The consequence is a radial redistribution which affects the diffusion parameters in the early times of the simulations.
After this transient period one can notice that axisymmetric models reach a stationary regime where the different diffusion parameter profiles remain relatively constant through time. When a bar forms we have found a different behavior for the mass redistribution. First, the diffusion appears to rapidly increase during the first $\sim$ 500Myrs inside the corotation while outside it reaches more rapidly a stationary regime. After this time diffusion profiles are roughly constant through time. This is understandable as bars grow and slow down significantly during the first $\sim$ 500Myrs of our simulations while after that period their sizes and pattern speed do not dramatically change. We have also found that, most of the time, the maximum of D is correlated with the UHR position near the corotation region. Therefore, during the secular evolution of a barred galaxy one expects the diffusion to be more important at the ends of the bar. Nonetheless we have not found systematic differences between profiles of the diffusion D, the radial dispersion $\sigma_\star$ and the velocity diffusion v_D between bars and axisymmetric lenticulars.

To also have two-dimensional information on the mass redistribution we have computed maps of the relative mass evolution in the disk. It simply consists of dividing in bins the mass at a given time by the mass at a previous reference time. This allows us to investigate the local mass evolution. To produce the maps of Figure 4.8 we have used a polar grid with a central cylindrical cell of radius 50pc. Bins are linearly spaced azimuthally and in radius. We also have limited the study to particles in the disk by excluding the ones located $\pm 1 kpc$ from the (x,y) plan of the galaxy. The reference time is chosen at T=750Myr and the second one is the final state of the simulation, both are oriented such that the bar (if present) is along the horizontal axis. At T=750Myr the bar is already formed and its pattern speed remains roughly constant until the end of the run. We then assumed that the position of the resonances computed in the final state are the same ones from

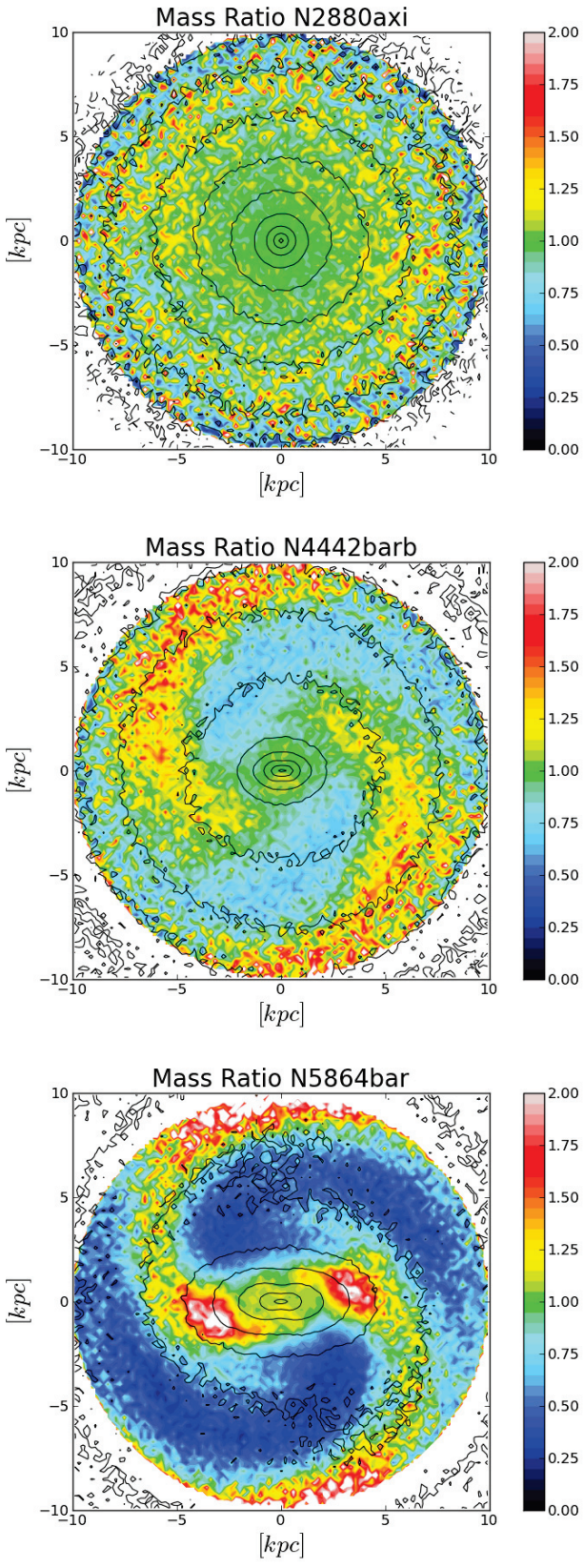

Figure 4.8: Maps of the relative mass evolution of N2880axi, N4442bar, N5864bar. On all figures isophotes of the final state are overplotted in thin black lines.

750Myr to the end of the runs.

In Figure 4.8 we give examples of the mass redistribution for N2880axi, N4442bar and N5864bar. We can see that the mass does not significantly vary for axisymmetric galaxies. The mass remains roughly constant in all bins.
For barred models, the orbital strucure induces a specific mass redistribution. We find in most of our barred models (such as N4442bar and N5864bar) a relative increase of the mass up to a factor two before the end of the bar and along the bar while a relative decrease also up to a factor two is found on their sides at the same radius. We presume that the x_1 orbits family is responsible for this effect, having elongated morphology along the bar major-axis.
For N5582bar and N3998bar it appears that the contrary is found in the most inner regions with a decrease of the mass along the bar major-axis. As in these two models the IILR and the OILR both exist x_2 orbits can be present. If we assume that it is the case it would explain this relative decrease of mass along the bar major axis as orbits are elongated along the bar minor axis. A more detailed study is required to confirm this interpretation.

4.5.2 Metallicity redistribution

Mock metallicity

A consequence of the matter redistribution under the influence of a bar is the subsequent metallicity redistribution. In order to study the influence of the bar driven influence we assume a metallicity gradient at a reference time. We use the average gradient found in observation in Kuntschner et al. (2010) for old galaxies $[Z/H](R) = -0.25 \log R + C$ where C is an arbitrary constant in our case. Thus particles at a reference time are given a metallicity as a function of their radial position. Once each particle has a metallicity we can follow the radial and two-dimensional redistribution. We used here the same reference time as previously (i.e. T=750Myr).

Metallicity gradient flatening

First, we have studied the metallicity radial redistribution and the influence of the bar on the metallicity gradients. Gradients are azimuthal average computed along radii in bins linearly spaced every 100pc. At the reference time when the metallicities are set, we compute the reference gradient $[Z/H]_{ref}(R)$ which is obviously linear in $\log(R)$. We then compute in the same bins the gradient in the final state of the simulation $[Z/H]_{final}(R)$. Metallicity in each bin is computed by averaging the metallicity of particles inside the bin.

As we only focussed on the relative evolution of metallicities, we set the constant C for our gradients such that we can make the ratio between the final gradient and the initial one without any discontinuity $\mathcal{R}_{met}(R) = [Z/H](R)_{final}/[Z/H](R)_{ref}$. We chose C such that $[Z/H]_{ref}(20 \cdot Re) = 0$. Figure 4.9 shows the metallicity gradient at the reference time T=750Myr and the final state and their ratio for N2880axi, N4442bar and N5864bar.

For axisymmetric models the metallicity gradient remains nearly constant at all times. A small radial mixing inherent to any galaxy evolution causes a decrease inside the most inner parsecs. In this region the metallicity is initially maximal and can only decrease. In the outer region the metallicity increase is mainly due to a numerical issue. Indeed in the outer parts only few particles are present and they have a low metallicity. Then if in the final state a particle from the central

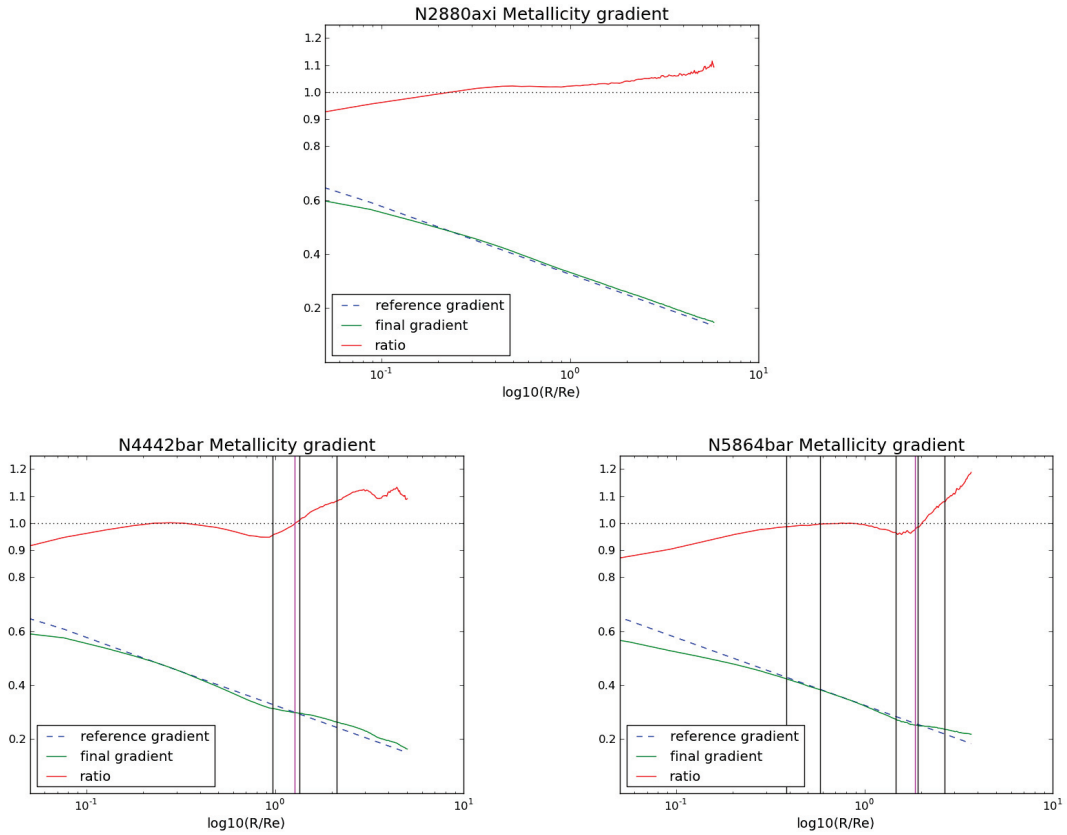

Figure 4.9: Metallicity gradients for N2880axi, N4442bar and N5864bar.The blue dashed line represents the reference metallicity gradient at T=750Myr, the green line is the metallicity gradient in the final state and the red line represent the ratio $\mathcal{R}_{met}$ between the last two gradients.

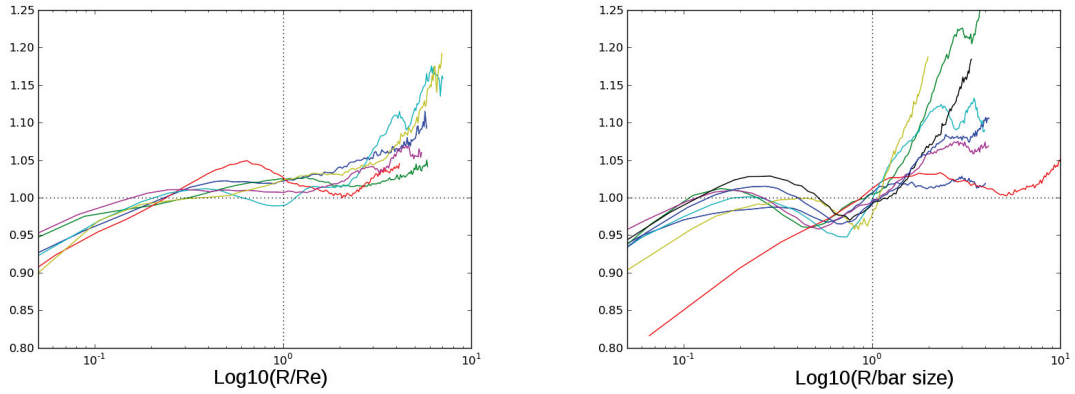

Figure 4.10: $\mathcal{R}_{met}$ as a function of the radius normalized by Re for axisymmetric models (left) and by L_{bar} for barred models (right).

part at the reference is present in the outer bins the computed metallicity is significantly increased. That is why we did not consider the most outer regions in our study. Moreover the dynamical influence of the presence of the bar does not significantly affect these regions. Apart from these two notes, metallicity gradients for axisymmetric models do not dramatically change with time and are monotonic as shown in Fig 4.10 (upper panel).

The presence of the bar has important consequences on metallicity gradients. First of all, as expected, a flattening of the $[Z/H]$ curve is observed in all barred models. We have found that this flattening is correlated with the length of the bar L_{bar} as shown in Fig 4.9. Figure 4.10 (right figure) shows the same effect through $\mathcal{R}_{met}$, indeed metallicity ratios all present minima before the end of the bar and a significant increase outside L_{bar}.
In order to better quantify the influence of the presence of a bar on existing metallicity gradients we have computed the average value AVG and the dispersion STD of $\mathcal{R}_{met}$ inside a given radius R. We have done this for four different radii : inside the bar L_{bar}, the corotation (CR), one effective radius Re and inside 20kpc (i.e. the whole galaxy). We then have compared these values to the bar torque (i.e. the bar strength) and the bar size L_{bar}. As presented in Fig 4.11 the most striking feature is the correlation between AVG and the bar torque and between STD and the bar size. In other words the stronger the bar the more the final gradient deviates from the original one and the longer the bar the more the metallicity varies inside the bar region.

This can be explained by the orbital structure. A long bar will trap particles far from the inner regions in x_1 orbits, thus it brings particles with a relatively lower metallicity in inner regions with high metallicity. A longer bar will mix metallicity within an important radius and metallicity range which explains the larger spread in metallicity inside the bar region.

local evolution

In a second stage, we have investigated the local evolution of metallicity. For that we have computed the relative evolution of the metallicity between T=750Myr and T=2Gyr in the same grid used to computed the relative mass evolution. Again we have excluded particles further than $\pm$1kpc from the equatorial plane. Figure 4.12 presents the relative metallicity evolution for N2880axi, N4442bar and N5864bar.

As we can see with N2880axi, the metallicity in axisymmetric models is not significantly redistributed. In addition with the mass evolution it means that no important radial mixing is present. We can assume that the metallicity profile of such systems remains unchanged all along its secular evolution.
As previously showed the mass redistribution is more important in barred systems and therefore metallicity is subsequently affected. N5864bar gives the clearest view of the influence of the bar on the metallicity distribution. We clearly see that the metallicity is higher just before the end of the bar and is lower on its sides at the same radius for all bar models. The presence of IILRs do not affect this signature of bars in the metallicity redistribution (see N3998bar and N5582bar in Appendix C). Moreover, in the case of a double bar structure (see N4233bar in Appendix C), the global metallicity redistribution appears to be the superimposition of this latter effect at the scales of both bars.

The local increase of metallicity can only occur if particles are brought from inside the studied region. In other words the higher metallicity found along the bar major axis is due to a spread of

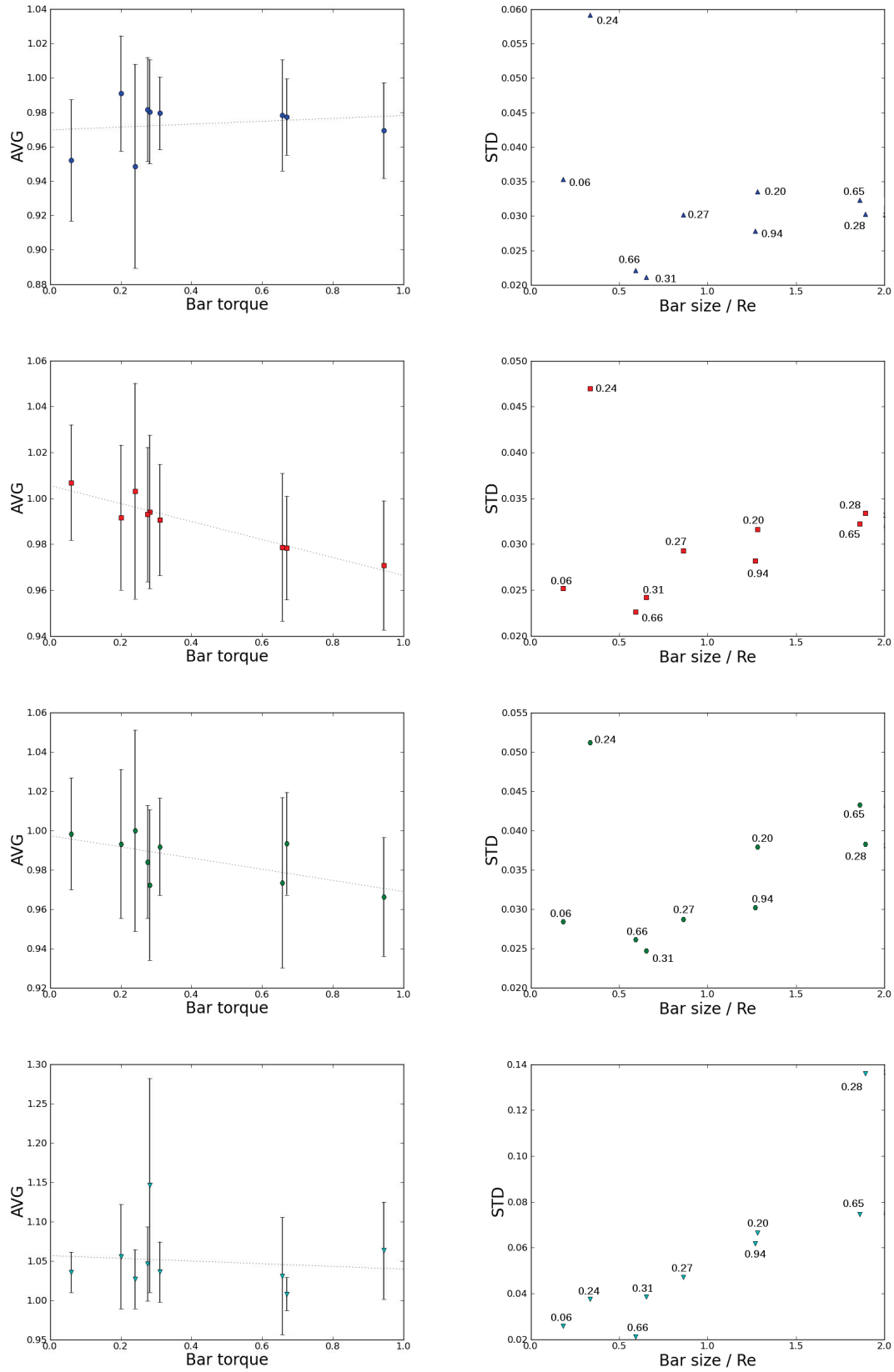

Figure 4.11: Correlation between AVG and the bar torque (left column) and correlation between STD and the bar size (right column). From top to bottom : inside L_{bar}, CR, Re and 20kpc. The bars for AVG represent STD. The numbers given on the figures of STD are the corresponding bar torques of the different models.

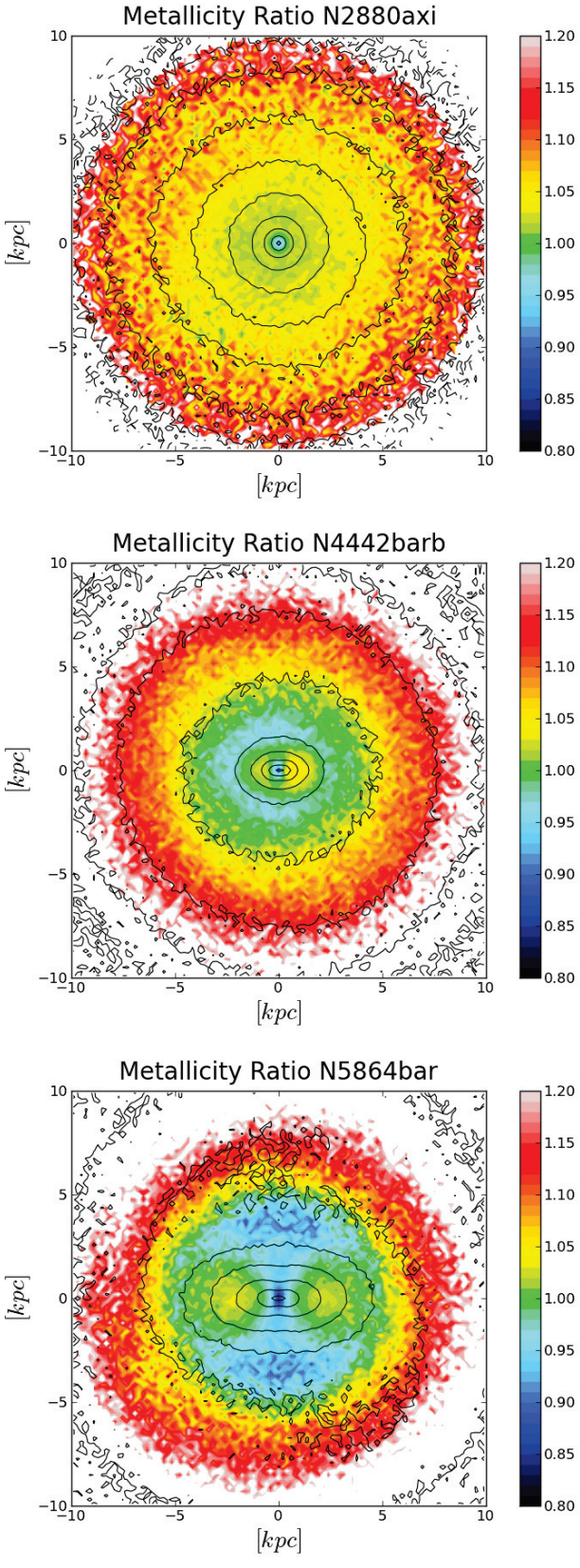

Figure 4.12: Maps of the relative metallicity evolution for N2880axi, N4442bar, N5864bar. On all figures isophotes of the final state are overplotted.

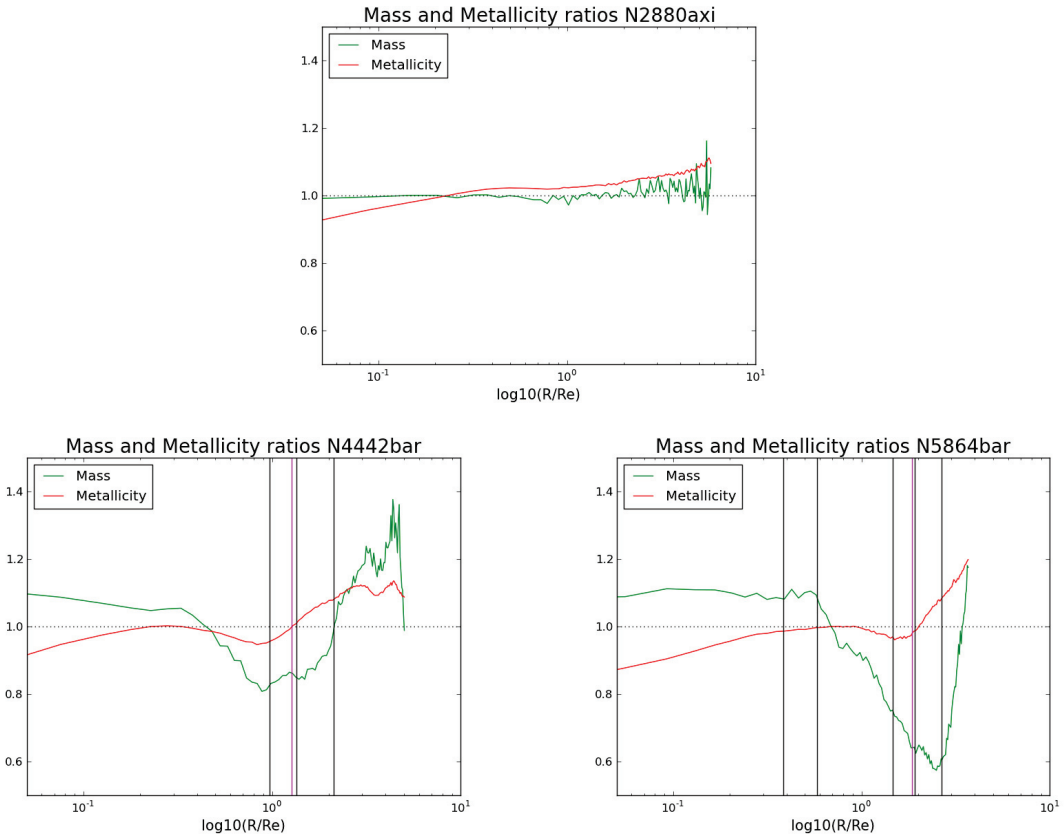

Figure 4.13: $\mathcal{R}_{mass}(R)$ (green line) and $\mathcal{R}_{met}(R)$ (red line) for N2880axi, N4442bar, N5864bar. For both barred models the magenta vertical line represent the bar end while the vertical black ones shows the location of dynamical resonances (IILR and OILR if they exist, UHR, CR and OLR from left to right).

central particles along this same axis. Again, this is naturally done by the existence of orbits from the x_1 family. Contrarily to mass redistribution which can locally increase/decrease the mass by a factor two, the metallicity is locally increased/decreased inside the bar regions by only up to 10% in the most extreme cases (see Fig 4.12).

4.5.3 Correlation between mass and metallicity redistribution

As the mass and metallicity redistribution are linked with the secular evolution of barred and unbarred galaxies we have compared the relative evolution of mass with radius to the relative metallicity evolution. We have computed the ratio between the radial mass distribution $\mathcal{M}(R)_{ref}$ at our reference time T=750Myr and the final radial mass distribution $\mathcal{M}(R)_{final}$: $\mathcal{R}_{mass}(R) = \mathcal{M}(R)_{final}/\mathcal{M}(R)_{ref}$. In Fig 4.13, $\mathcal{R}_{mass}(R)$ and $\mathcal{R}_{met}(R)$ are both shown for N2880axi, N4442bar and N5864bar (same figures for all numerical models can be found in Appendix C). Axisymmetric models such as N2880axi typically do not show any significant evolution of both their radial mass and metallicity distributions. For numerical models of barred galaxies (see N4442bar and N5864bar

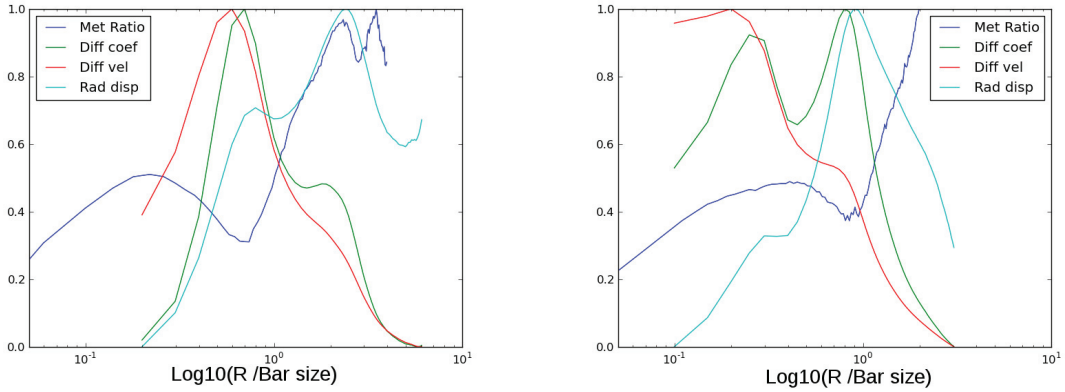

Figure 4.14: Superimposition of radial profiles of D, $\sigma_\star$, v_D and $\mathcal{R}_{met}$ for N4442bar, N5864bar. All profiles have been vertically scaled. The x-axis has been normalised by the bar size.

in Fig 4.13) we see that the radial mass distribution and the metallicity gradients are both affected as previously found. Nevertheless the consequence is much more important for the mass radial redistribution than for the subsequent metallicity redistribution. The important point is that the minimum of $\mathcal{R}_{mass}$ is correlated with L_{bar} and then also with $\mathcal{R}_{met}$.

We have also compared $\mathcal{R}_{met}$ with the profiles of all three diffusion parameters. We have only performed a brief qualitative comparison by superimposing radial profiles of the diffusion D, the radial dispersion $\sigma_\star$, the diffusion velocity v_D and $\mathcal{R}_{met}$. Figure 4.14 presents the profiles superimposition for N4442bar and N5864bar. On this latter figure curves have been vertically scaled such that they fully fit inside a unity range and the distance from the center is normalized by the bar size.
We confirm that the diffusion D presents a maximum at the end of the bar while $\mathcal{R}_{met}$ shows a minima. We have found this correlation between the diffusion maximum and the metallicity relative evolution minima in every barred numerical models. The decrease in the metallicity gradient in this region is then due to an important radial mixing.

4.6 Discussion

4.6.1 Observational guidelines

One goal of this work has also been to provide guidelines to better understand and interpret observational data. Interactions with observers inside the ATLAS^{3D}team has therefore been highly encouraged and led to the conclusions given hereafter.

The first conclusion of our study is that, in agreement with Friedli et al. (1994), the presence of a bar implies a flattening of pre-existing metallicity gradients. This flattening is linked with the exchange of angular momentum associated with the bar and increases with the length of the bar. One would expect to be able to observe such systematic signature.
The local increase/decrease of the metallicity due to the bar hardly exceeds 10% in the most extreme case for our set of simulations. Moreover we have found that this clear signature is found just before the end of the bar. This small deviation though systematic is hard to reveal in observations.

First of all, because data often do not allow to reach such a precision. A deviation of 10% is rather small and explain why we see so little in real observations. However, with good signal-to-noise and careful analysis this could be detected. Believing that the detection of such deviation is a significant signature of bar-driven evolution would then be a matter of interpretation.
Second, observations have to extend at least to the end of the bar in order to cover the region of the signature. IFU data used for the observational study of the metallicity of stellar populations in the ATLAS^{3D}sample did not allow to cover this region. Due to the proximity of galaxies and the size of the field-of-view, the region covered is most of the time inside one effective radius and also often do not extend beyond the end of the bar. Comparisons with observational data have then been often unfruitful in the ATLAS^{3D}sample although some cases can correspond to our conclusions. A more careful study is require here before any strong conclusion can be drawn.

Another possible interesting item to be discussed is the influence of the viewing angle. Indeed, it is reasonable to assume that the galaxy inclination and the position angle of the bar both influence metallicity measurements along galaxy major-axis and minor-axis. This issue should be the subject of further investigation.

4.6.2 Bar driven stellar formation - preliminary results

Our investigation has confirmed that the presence of a bar flattens existing metallicity gradients. Thus one can expect to find this signature in isolated ETGs which evolution has been bar-driven. Nonetheless the variety of metallicity gradients observed cannot be explain by the simple mass redistribution induced by the presence of a bar. As the stellar formation obviously affects the metal enrichment in a galaxy, it has to be considered. The second set of simulations we have run is aimed at investigating this issue with in-situ star formation.
More metal-rich young stars formed in the barred are expected to significantly modify metallicity gradients in the bar regions. A deep numerical study would require the elaboration of synthesis population model in order to calibrate the ages and metallicities of each particle (see e.g. Michel-Dansac & Wozniak, 2004; Wozniak, 2007). So far, we did not focus on this point but this is undoubtly the next step in our study of the metallicity and in addition ages distribution.
At the same time the presence of gas and new stars also influence the dynamics of barred galaxies. We have only very briefly investigated this last point and comparing the dynamics of gas-less and non gas-less barred ETGs. More precisely, we are focusing on N2880axisf and N4570barsf cases.

4.7 Conclusions

In this chapter we have presented promising preliminary results on the influence of a bar-driven evolution on the mass and metallicity distribution in ETGs. This investigation is based on the analysis of high resolution numerical models of barred and axisymmetric ETGs. Computing bar properties and simple quantification of the metallicity gradients and the mass redistribution we have found several correlations.

We have confirmed previous results from Friedli et al. (1994) that the dynamical influence of a bar tends to flatten existing metallicity gradients. In observations it appears as a "shoulder" in the metallicity curve as a function of radius. We have shown that this is a systematic signature of a secular bar-driven evolution of a pre-existing gradient. Moreover we have found a clear correlation between the signature radial location and the length of the bar. The amplitude of this "shoulder" effect being also linked to the bar size. The longer the bar the more important is the signature.

When investigating the local metallicity evolution in our numerical models we have also found that the most important evolution occurs at a radius coresponding to the bar semi major-axis. We have shown that a relative increase in the metallicity happens along the bar major-axis while the contrary is observed along its minor axis.
Nonetheless while trying to draw guidelines for observations it appeared that the data quality and S/N and the impact of the viewing angle may not permit to clearly find the "shoulder" signature in real observations of ETGs.

In addition we have studied the mass redistribution using the work done in Brunetti et al. (2011). In all our models we have computed diffusion parameters : the diffusion D, the radial dispersion $\sigma_\star$ and the dispersion velocity v_D. We have shown that the signature region in the metallicity distribution of barred models also correspond to the maximum in diffusion at a radius corresponding to the bar semi major-axis. Moreover at the end of the bar the mass is increased by up to a factor two and decreased by the same factor on the bar sides at the same radius.

A simple explanation is given through basic orbital structure of bars. The x_1 orbits family which is the backbone of bar structures is elongated along the bar major-axis. These orbits naturally mix mass inside the bar region and therefore the metallicity. As a consequence mass and metallicity are increased along the bar major-axis and decreased along bar minor axis.
Previous studies on bar evolution explain that bars lengthen by traping chaotic orbits around the corotation. The consequence of this would be a global decrease of the average metallicity inside the bar region during the bar growth. We can also assume that this decrease would depend on the final bar length. In our cases, bar lengths stayed nearly constant within the time range we have studied here; and this effect is not significant compared to the dynamical redistribution.

These previous results give some clues to better understand the consequence of the presence of a bar on the mass and metallicity redistribution. However, the dynamical influence of a bar simulated here cannot explain the variety of metallicity gradients observed. As it is known that the stellar formation history influences the metallicity enrichment in a galaxy the next step is to implement synthesis stellar population models in our simulations. We have already performed several high resolution simulations that are currently being analysed. All the work done in the present chapter is considered as a basis for the interpretation of this new set of simulations. We expect with the whole set of numerical models to bring important clues in the understanding of the stellar population ages and metallicity distributions of barred ETGs and therefore of the secular evolution of such systems.

Chapter 5

Summary and perspectives

The aim of the work presented in this thesis is to increase our understanding of the influence of a bar on ETGs evolution. I have thus, as a first step, investigated how biased is the dynamical modeling of barred systems under the assumption of axisymmetric mass distribution. In a second step, I have used numerical models to better understand the influence of bars on the mass and metallicity distribution in ETGs.

5.1 The dynamical modeling issue

The dynamical modeling of observed galaxies allows to determine some dynamical parameters such as the galaxy dynamical mass-to-light ratio M/L, the velocity anisotropy for instance. These quantities are important clues to understand galaxy evolution. Models require a number of assumptions such as the geometry of the mass distribution for instance.
I have demonstrated that the presence of a bar biases the recovering of dynamical parameters when assuming an axisymmetric mass distribution. While the inclination recovery is not influenced, the mass-to-light ratio M/L is significantly biased and the global anisotropy β_z seems unrecoverable. The introduced biased depends on the galaxy inclination and the bar position angle. We have also found that the bar size plays a role and one can expect that other properties can correlate with the observed overestimations (e.g. bar strengths).
However, results found give only an estimation on the introduced bias and do not allow to determine an accurate process to correct for this effect for all barred galaxies in the ATLAS^{3D}sample, the variety of bars length, strength and viewing angle being the main limitation.

5.2 Towards a better understanding of observed metallicity distributions in ETGs

In Chapter 4, I have investigated the mass and metallicity distributions in barred ETGs.
Previous results (see Friedli et al., 1994) of a flattening of existing metallicity gradients due to bars dynamics have been confirmed. With simple measurement we have found that the location of this signature is correlated with the bar length. Moreover, the amplitude appears to be also directly related to the bar size. Although small and hardly observable the dynamical signature is systematic and in a well defined region. This effect is linked to the radial mixing due to the presence of the bar and the study of diffusion in our numerical models shows an agreement between the location

of the diffusion maximum and the metallicity flattening.
However, the building of population ages and metallicity distributions depends on the stellar formation history of galaxies. A new set of simulations including gas and star formation has been build in order to investigate this point. The previous work will be used as a basis for the analysis and interpretation of these new runs. We expect, through the analysis of the new numerical models, to better understand the influence of a bar-driven evolution on ETGs ages and metallicity distributions associated with the bar characteristics.

5.3 Perspectives

Simulations, including both barred and axisymmetric models, presented in this thesis were aimed at answering specific questions. A lot of work with these numerical models still has to be done to bring more precise answers to issues developed in the previous chapters. Nonetheless, the variety of compositions, mass distribution, bars length and strength and dynamics presented in the numerical models performed in this thesis, provide a remarkable benchmark that can be used for several other studies. I give below an overview of investigations I expect to perform in the near future but also on a longer timescale.

5.3.1 Improving dynamical modeling

At the time of the study presented in Chapter 3, the sample of numerical models used was limited to four simulations (two bars and two axisymmetric). Adopting the same procedure with more numerical models presenting a variety of bar lengths and strengths would allow to investigate the influence of these latter parameters on the overestimation of M/L. From the quick study done on these points, one can expect to find a clear correlation between bar properties, the viewing angle and M/L bias. As a consequence, a quantitative correction could be applied to the M/L determined for barred galaxies in the ATLAS^{3D}sample, and more generally to broader sample of galaxies.

5.3.2 Ages and metallicity distribution

In Chapter 4 our study focus on the evolution of metallicity and mass distributions when the bar is settled in the disk and relatively stable through time. We did not include the formation period in this investigation because of the overlaping with processes such as the initial relaxation of the simulations. We can however imagine to force the axisymmetry of the system until the system is relaxed and then let the bar form. This would allow us to investigate the influence of the bar growth on the observed metallicity.

The investigation of the mechanism responsible for the various of metallicity profiles observed implies to consider the influence of star formation history in barred ETGs. Several numerical models have been performed and their detailed analysis is the next priority. In order to derive robust conclusions, stellar population models have to be included in order to calibrate particle ages and metallicities.
As already found, young more metal rich stars massively form along the bar major-axis and in the most inner regions. The consequence on the metallicity enrichment in this area is then expected to be important, probably more than the dynamical redistribution signature itself. Thus one can wonder if the "shoulder" effect can still be seen in star forming barred galaxy. Moreover,

it would be interesting to find if the addition of gas and the star formation allow to explain the variety of metallicity gradients observed in barred galaxies. If not, that would lead us to investigate for instance the influence of external factors such as galaxies encounters and mergers on metallicity.

5.3.3 Other potential avenues

The double bar formation

The fact that the model N4233bar naturally presents a double bar without any specific constraint on the initial kinematics offers a great opportunity to study its formation process. Moreover, one can expect to find more reliable methods to derive the pattern speed of both bars from observations. This is already the subject of a side project as mentioned in Chapter 4.

Dark matter halo

Recent studies focused on the relation between the bar formation and geometry and the dark matter halo triaxiality (e.g. Dubinski & Chakrabarty, 2009; Machado & Athanassoula, 2010). Considering that most of my simulations include a live dark matter halo, they then could be used to study the mutual influence between the bar geometry and the halo triaxiality.

5.3.4 Future Simulations

Although the variety of bars in my sample of simulations already covers an interesting range of shapes and strengths, it would be useful to extend the sample to have a broader representation of the bars variety. Building such a complete sample would allow us to derive statistically robust conclusions about correlations between bar properties and characteristics of the host systems. Besides, as the PM/sticky particle is no longer available, new simulations may be now run with the AMR code `RAMSES`. This would allow to significantly increase the number of particles used and the resolution.

Such a sample of very high resolution simulations would clearly allow us to probe dynamics of barred galaxies up to very small scales, revealing clues to better understand the evolution of such systems and the building of the presently observed galaxy zoo.

Appendix A

Side projects

Along my thesis I contributed to some projects by showing some of my simulations and their analysis. A brief summary on these "side-projects" is given here.

A.1 Intrinsic ellipticy in the ATLAS^{3D}sample

In the frame of the ATLAS^{3D}project, an issue arose while investigating intrinsic ellipticities of the 260 galaxies. If we assume that all galaxies in the sample are perfectly oblate systems, this means that when observing them face-on, we should see a perfectly round galaxy. When fitting an oblate intrinsic shape distribution to the galaxies in the ATLAS^{3D}sample, and then 'observing' this intrinsic shape distribution by randomly sampling viewing angles, the oblate model predicts a large number of round galaxies. This is not what is observed.

One possible explanation is that galaxies are not really oblate, they are slightly triaxial. However, triaxial systems are also kinematically misaligned, and that is something that we do not observe for fast rotators.
Another explanation, if we assume that the oblate model is correct, is that there can be a problem with observations or measurements. This can be due to :

- The influence of the observational conditions (atmosphere opacity, telescope movements).
- The fitting routine which is sensitive to small disturbances in the isophotes and then biased towards larger ellipticities.
- data is not deep enough and we are missing the outer-shape of the galaxy.
- bars which are obviously not round and can therefore bias measurements.

To investigate the last point I have provided simulation outputs to Dr Davor Krajnovic and Dr Anne-Marie Weijmans.
The first results confirm that the bar biases measurements but, it appears that it cannot fully explain the lack of round galaxies.

A.2 The cylindrical rotation figure

In collaboration with Dr Michael Williams, we have studied the influence of the presence of a bar and its orientation on IFU datas of edge-on galaxies. We focused on the typical kinematic signatures in the projected velocity V, velocity dispersion σ and third and fourth Gauss-Hermite moments h_3 and h_4 of a bar. The goal is to understand the "cylindrical rotation" (see Williams et al., 2011) figures observed in nearly edge-on seen barred galaxies and to understand to which extent this is related to the bar orientation and properties. This study has been done for only two of my models so far (N4754barb and N5864bar) but we have already found that the orientation of the bar influences the spatial extention of the cylindrical rotation figure. Indeed, when the bar is seen end-on the cylindrical rotation figure can hardly been found, while when the bar is seen side-on the extention of the cylindrical rotation figure is maximised.
Several other parameters have been investigated such as the influence of the vertical extension of the bar, the size of the field-of-view and the pixel size. We have obviously found that the cylindrical rotation figure cannot be observed when using pixels too big compared to the bar horizontal and vertical size.
This investigation must be extended to a larger number of simulations, and we expect to correlate systematic signatures in the kinematics with bar properties but also with the bar/disk ratio.

Appendix B

Chapter 3 appendix

B.1 JAM recovery summary

B.2 JAM fitting

Model	$i_{\rm SIM}$	$\rm PA_{bar}$	$i_{\rm JAM}$	$\beta_z^{\rm SIM}$	$\beta_z^{\rm JAM}$	$M/L_{\rm vir}$	$M/L_{\rm JAM}$	M/L Error in %
N4179axi	25	$\emptyset$	23.8	0.106	0.4	6.29	6.87	9.22
	45	$\emptyset$	43.1	0.106	0.2	6.29	6.36	1.11
	60	$\emptyset$	59.4	0.106	0.05	6.29	6.30	0.16
	87	$\emptyset$	84.9	0.106	0.1	6.29	6.26	0.48
N4570axi	25	$\emptyset$	22.4	0.145	0.25	16.93	18.43	8.86
	45	$\emptyset$	46.9	0.145	0.1	16.93	16.80	0.77
	60	$\emptyset$	60.7	0.145	0.1	16.93	17.10	1.00
	87	$\emptyset$	82.9	0.145	0.1	16.93	16.97	0.24
N4442bar	25	18	30.9	0.344	0.25	17.99	17.58	2.28
	25	45	27.3	0.344	0.55	17.99	21.82	21.29
	25	60	25.9	0.344	0.6	17.99	23.25	29.24
	25	87	24.3	0.344	0.35	17.99	22.51	25.13
	45	18	48.2	0.344	0.45	17.99	16.72	7.06
	45	45	45.6	0.344	0.1	17.99	17.67	1.78
	45	60	44.9	0.344	0.0	17.99	18.86	4.84
	45	87	44.3	0.344	0.0	17.99	19.93	10.78
	60	18	60.0	0.344	0.6	17.99	15.74	12.51
	60	45	59.3	0.344	0.2	17.99	17.63	2.00
	60	60	60.7	0.344	0.05	17.99	18.40	2.28
	60	87	60.6	0.344	0.0	17.99	19.16	6.50
	87	18	85.8	0.344	0.25	17.99	17.62	2.06
	87	45	84.7	0.344	0.25	17.99	17.94	0.28
	87	60	84.6	0.344	0.2	17.99	18.04	0.28
	87	87	85.1	0.344	0.1	17.99	18.21	1.22
N4754bar	25	18	30.1	0.343	0.0	11.04	9.82	11.05
	25	45	27.7	0.343	0.3	11.04	10.70	3.08
	25	60	25.4	0.343	0.3	11.04	12.18	10.33
	25	87	22.5	0.343	0.15	11.04	13.73	24.37
	45	18	51.4	0.343	0.0	11.04	10.42	5.62
	45	45	44.9	0.343	0.6	11.04	11.20	1.45
	45	60	44.6	0.343	0.6	11.04	11.98	8.51
	45	87	43.9	0.343	0.6	11.04	12.78	15.76
	60	18	65.8	0.343	0.0	11.04	10.50	4.89
	60	45	59.4	0.343	0.6	11.04	11.28	2.17
	60	60	59.6	0.343	0.05	11.04	11.68	5.80
	60	87	59.4	0.343	0.0	11.04	12.16	10.14
	87	18	86.2	0.343	0.2	11.04	11.05	0.09
	87	45	85.5	0.343	0.2	11.04	11.42	3.44
	87	60	84.7	0.343	0.2	11.04	11.64	5.43
	87	87	85.1	0.343	0.1	11.04	11.81	6.97

Table B.1: Table summarizing the values of i, $\rm PA_{bar}$, β_z and M/L of our mock observations and the values recovered by the JAM modelling method.

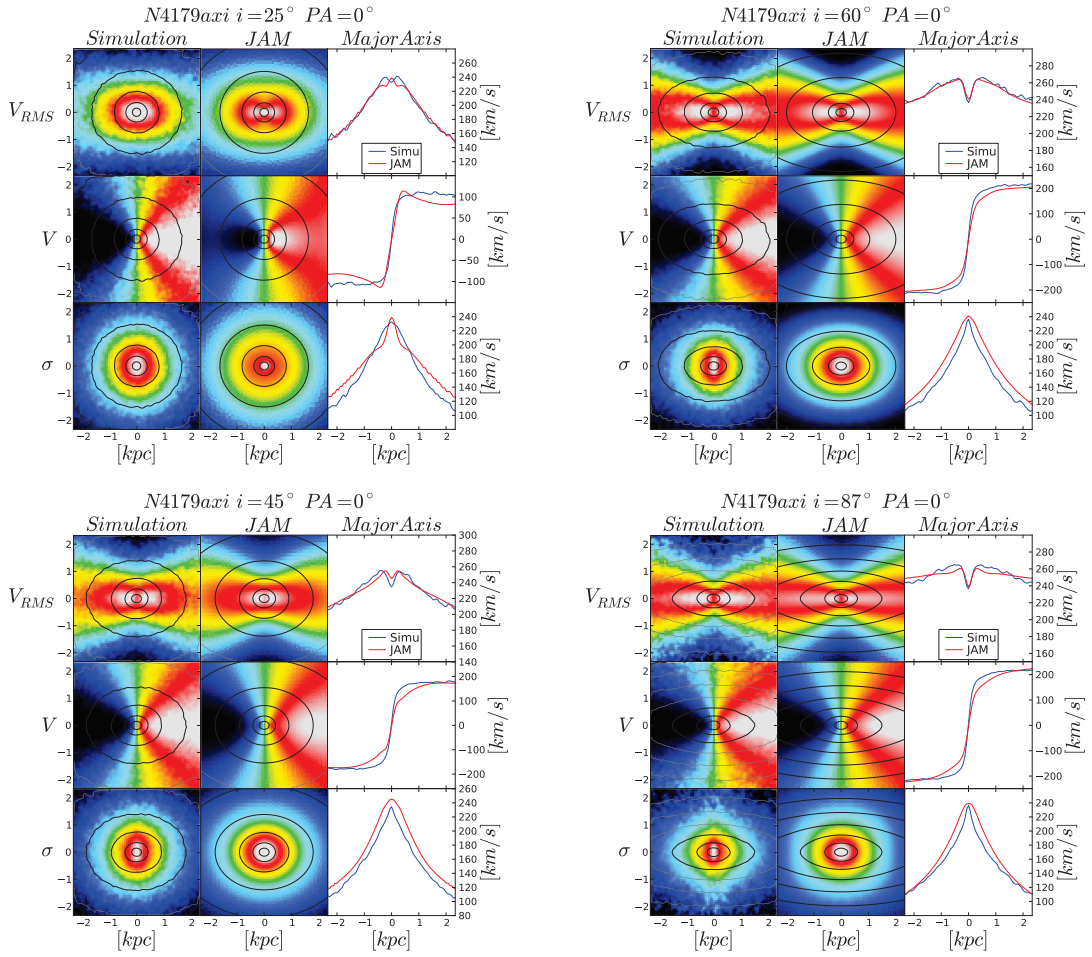

Figure B.1: Comparison between the simulations projected velocity maps and the best JAM fitting for $N4179axi$ for the four angles of projection.

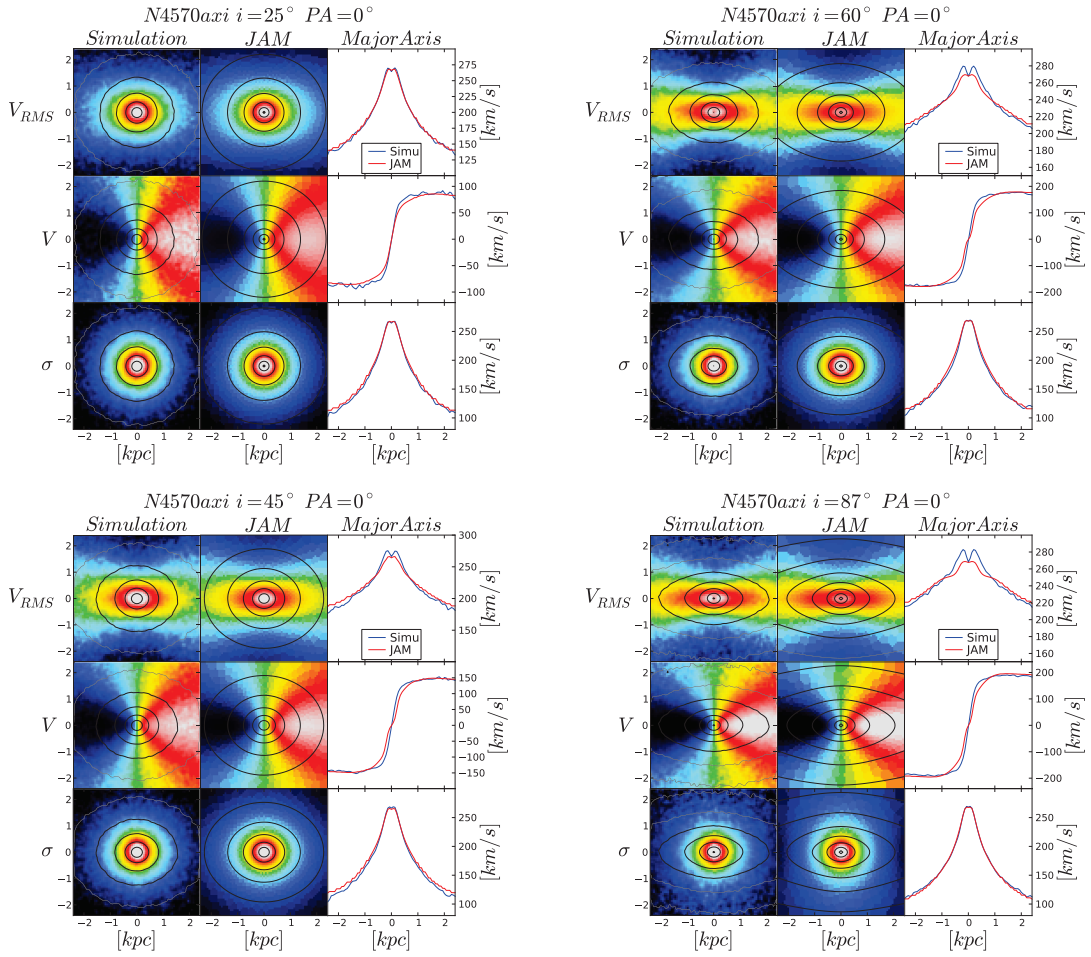

Figure B.2: Comparison between the simulations projected velocity maps and the best JAM fitting for $N4570axi$ for the four angles of projection.

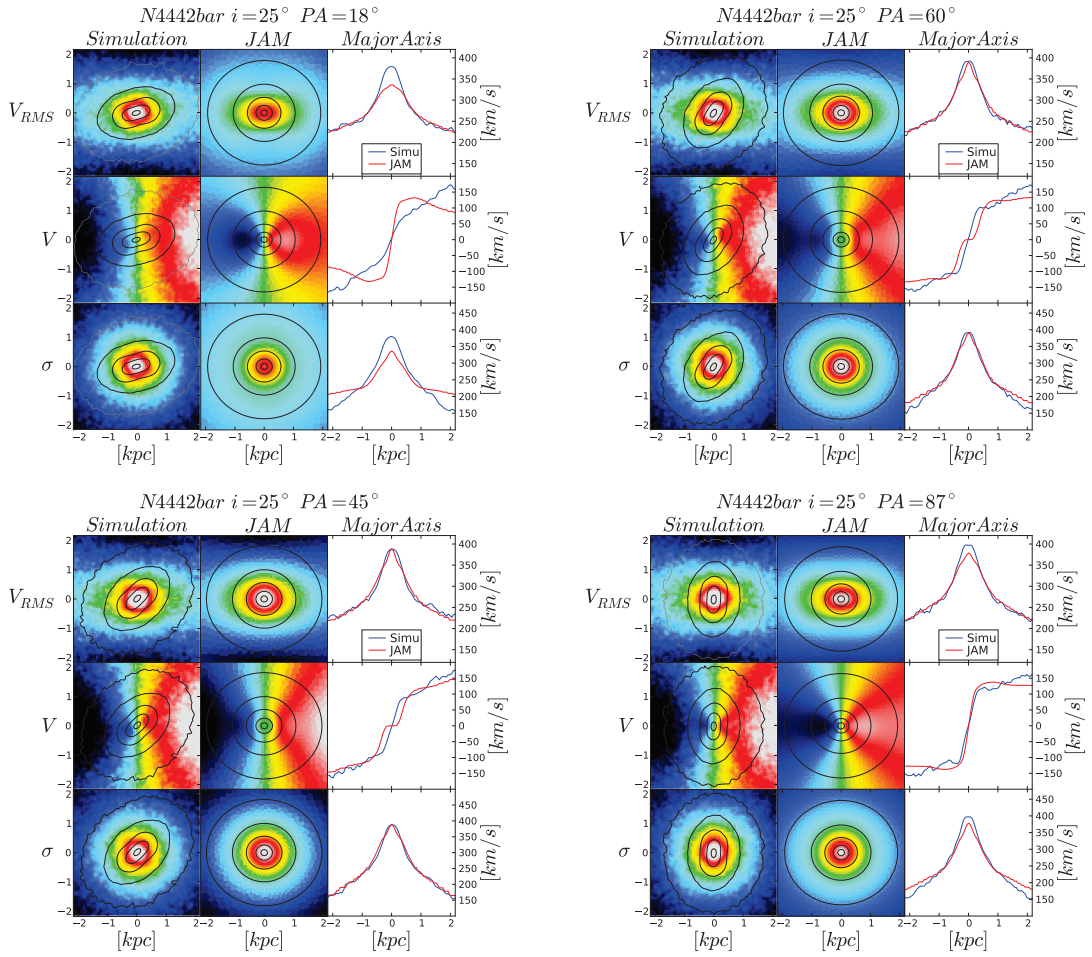

Figure B.3: Comparison between the simulations projected velocity maps and the best JAM fitting for $N4442bar$ for $i = 0.25°$ and the four $\mathrm{PA_{bar}}$.

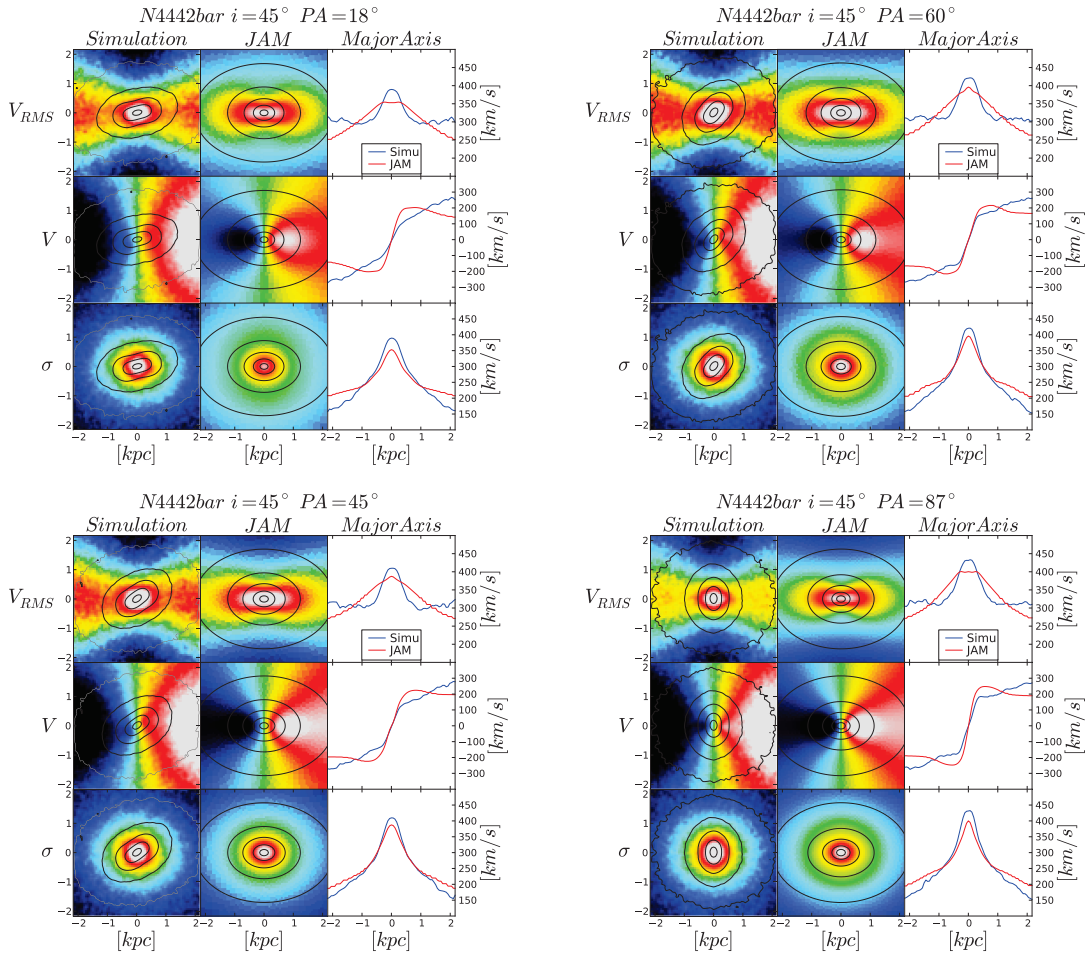

Figure B.4: Comparison between the simulations projected velocity maps and the best JAM fitting for $N4442bar$ for $i = 0.45°$ and the four $\mathrm{PA_{bar}}$.

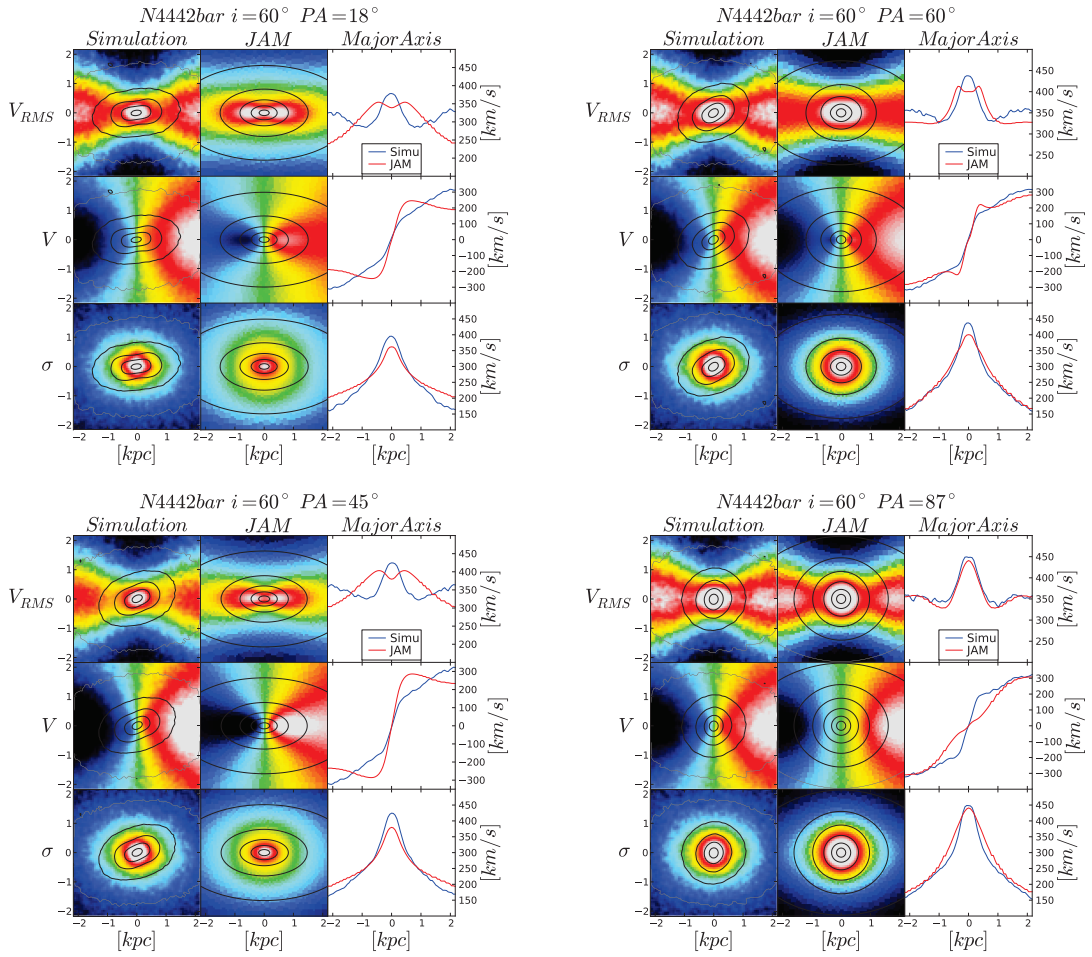

Figure B.5: Comparison between the simulations projected velocity maps and the best JAM fitting for $N4442bar$ for $i = 0.60°$ and the four $\mathrm{PA_{bar}}$.

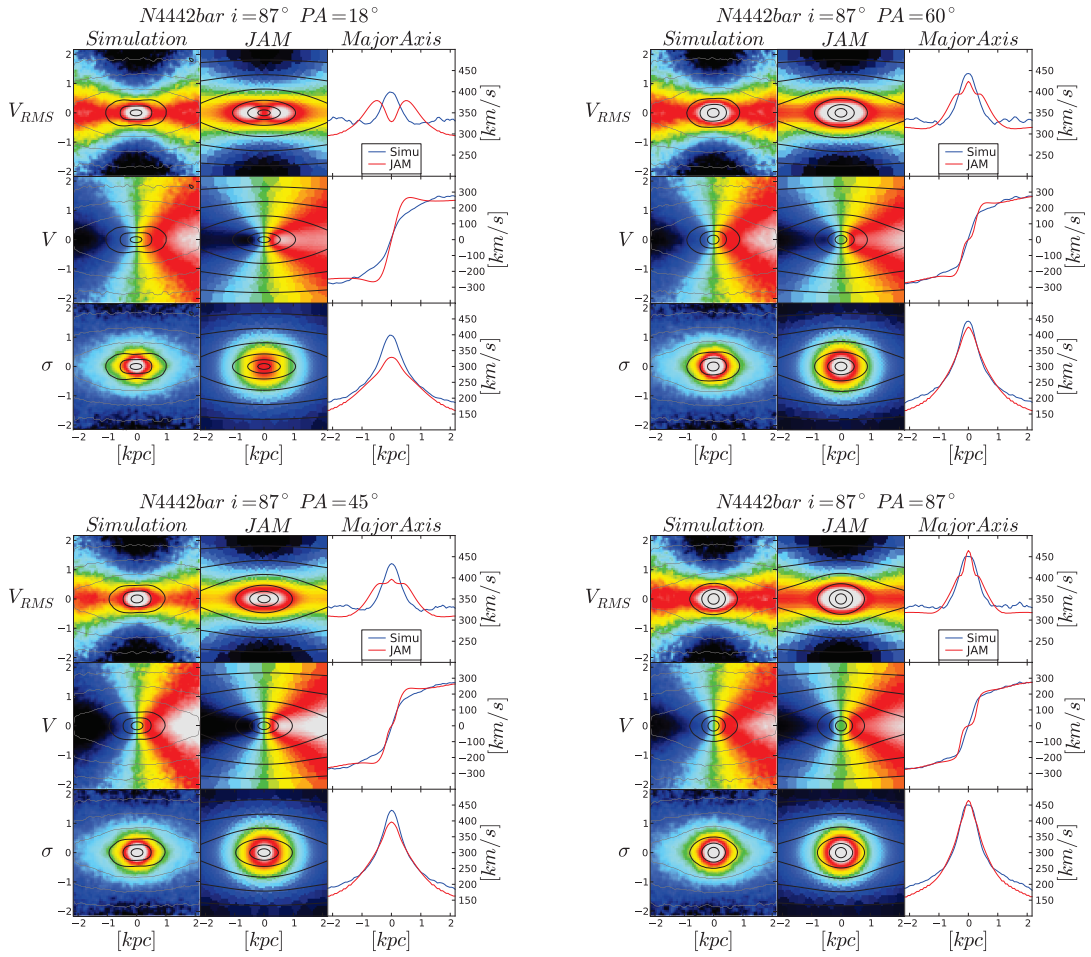

Figure B.6: Comparison between the simulations projected velocity maps and the best JAM fitting for $N4442bar$ for $i = 0.87°$ and the four $\mathrm{PA_{bar}}$.

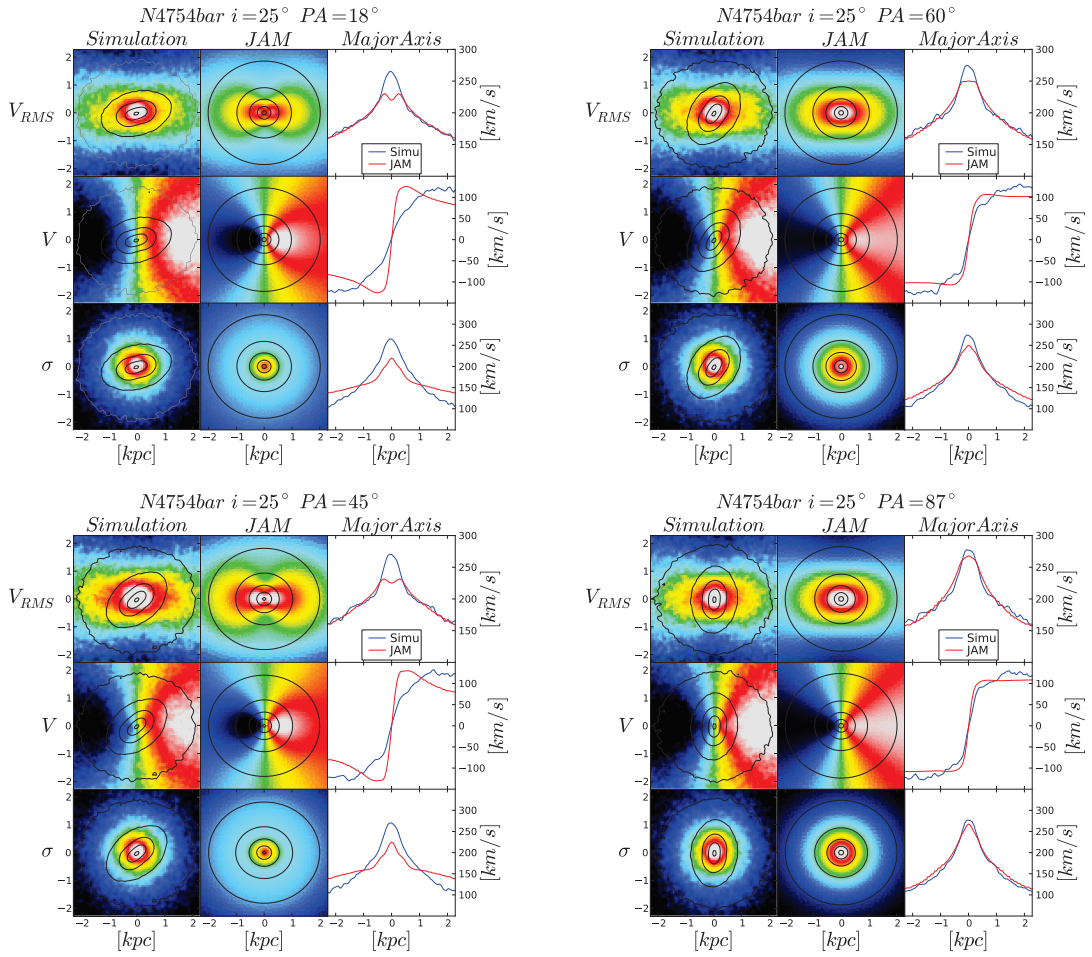

Figure B.7: Comparison between the simulations projected velocity maps and the best JAM fitting for $N4754bar$ for $i = 0.25°$ and the four $\mathrm{PA_{bar}}$.

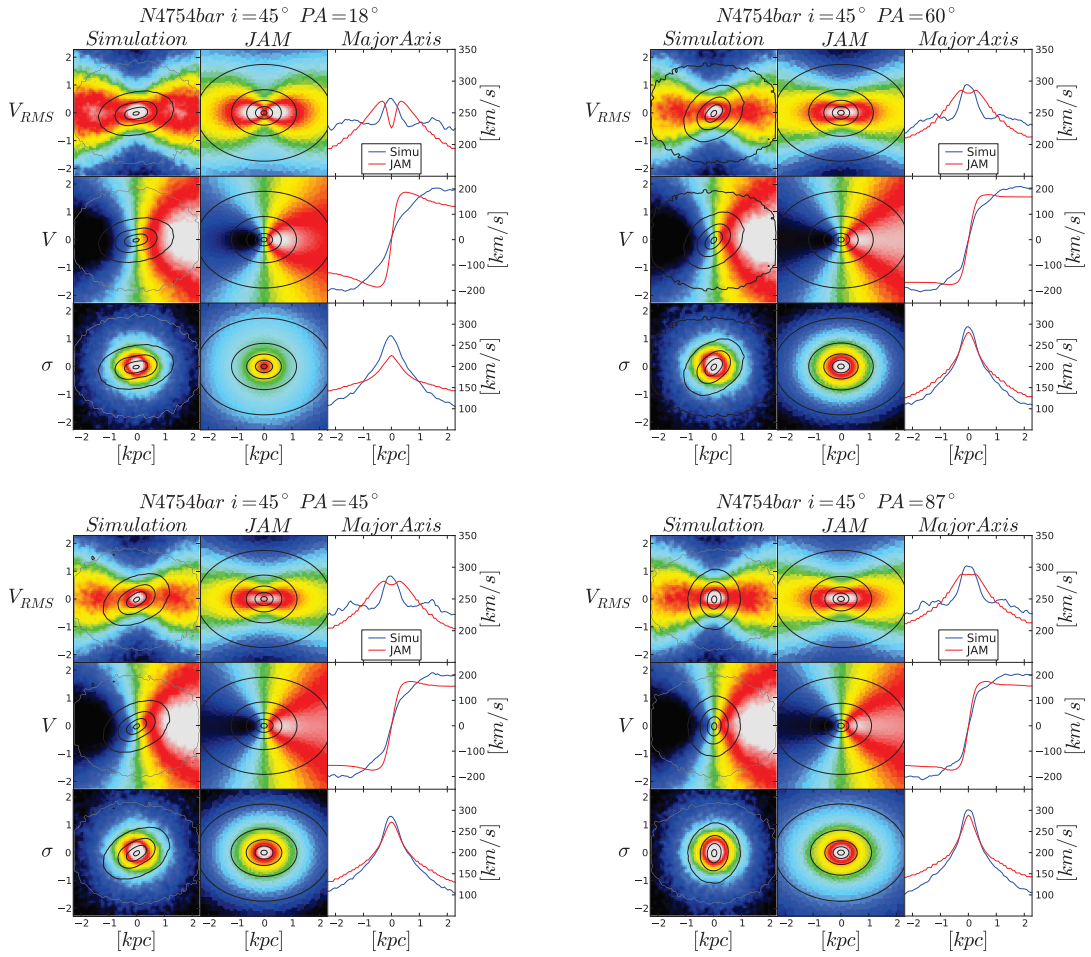

Figure B.8: Comparison between the simulations projected velocity maps and the best JAM fitting for $N4754bar$ for $i = 0.45°$ and the four $\mathrm{PA_{bar}}$.

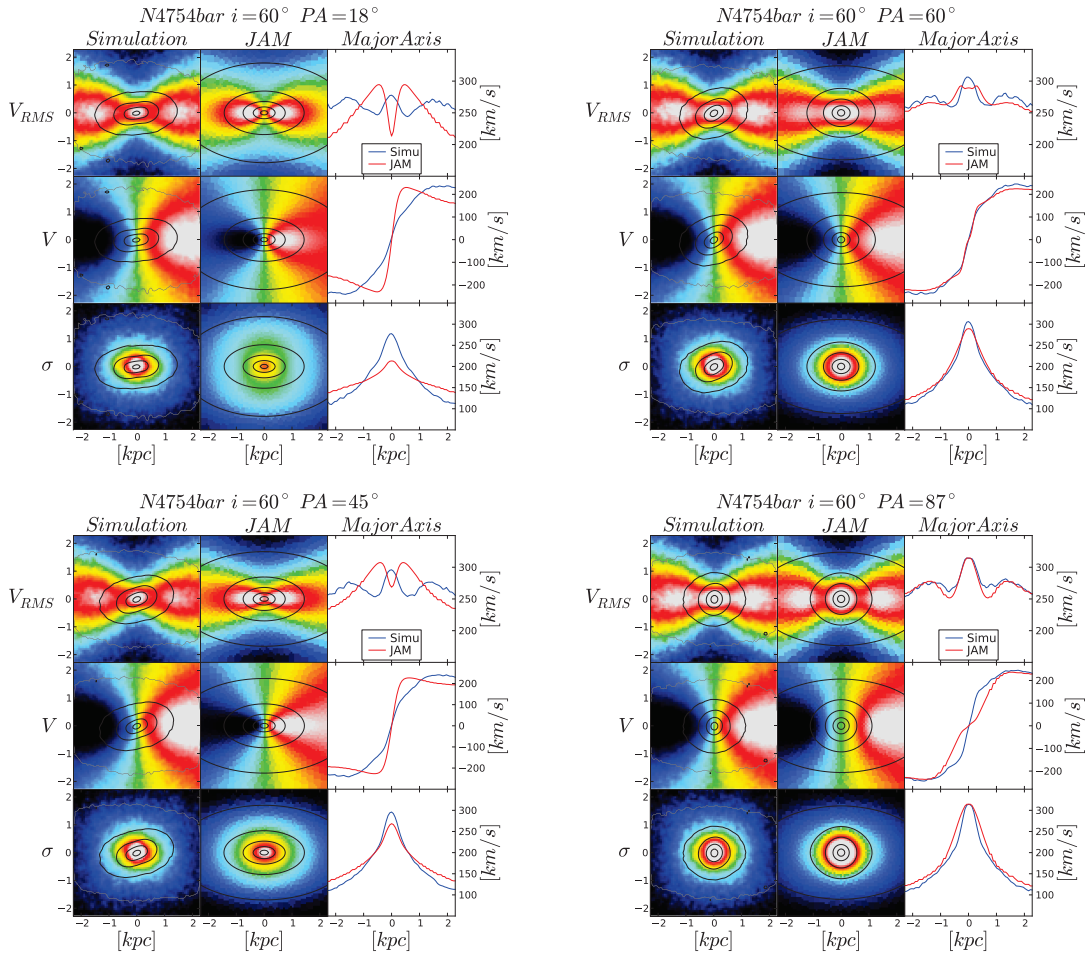

Figure B.9: Comparison between the simulations projected velocity maps and the best JAM fitting for $N4754bar$ for $i = 0.60°$ and the four $\mathrm{PA_{bar}}$.

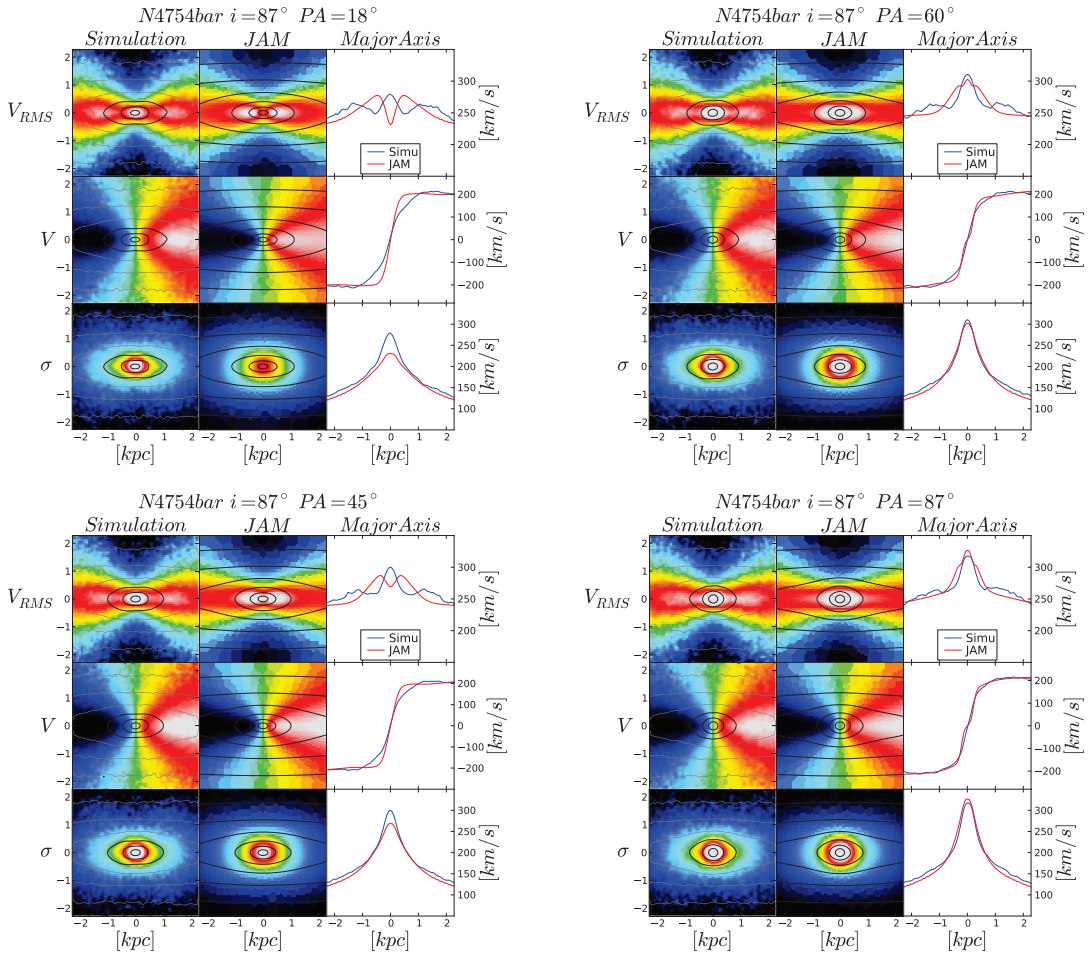

Figure B.10: Comparison between the simulations projected velocity maps and the best JAM fitting for $N4754bar$ for $i = 0.87°$ and the four $\mathrm{PA_{bar}}$.

Appendix C

Chapter 4 appendix

We present here for all simulations used in Chapter 4 (from left to right and from top to bottom) :

- The map of the local relative metallicity evolution.
- The map of the local relative mass evolution.
- Profiles of the reference (blue dashed line) and final (green line) metallicity gradients and also $\mathcal{R}_{met}(R)$ (red line).
- Profiles of $\mathcal{R}_{meass}(R)$ (green line) and $\mathcal{R}_{met}(R)$ (red line)
- Evolution of the diffusion coefficient D as a function of radius and time.
- Evolution of the diffusion velocity v_D as a function of radius and time.
- Evolution of the radial dispersion $\sigma_\star$ as a function of radius and time.
- Profiles of D, v_D, $\sigma_\star$ and $\mathcal{R}_{met}(R)$ scaled to unity and normalised by Re for axisymmetric models and by L_{bar} for barred models.

C.1 Axisymmetric models

C.1.1 N2880axi

C.1.2 N4179axi

C.1.3 N4179axib

C.1.4 N4233axi

C.1.5 N4255axi

C.1.6 N4570axi

C.2 Barred models

For barred models the location of dynamical resonances are represented by vertical lines on the figures. The size of the bar is also shown in a different color.

C.2.1 N0936bar

C.2.2 N3998bar

C.2.3 N4179bar

C.2.4 N4233bar

C.2.5 N4442bar

C.2.6 N4442barb

C.2.7 N4754barb

C.2.8 N5582bar

C.2.9 N5864bar

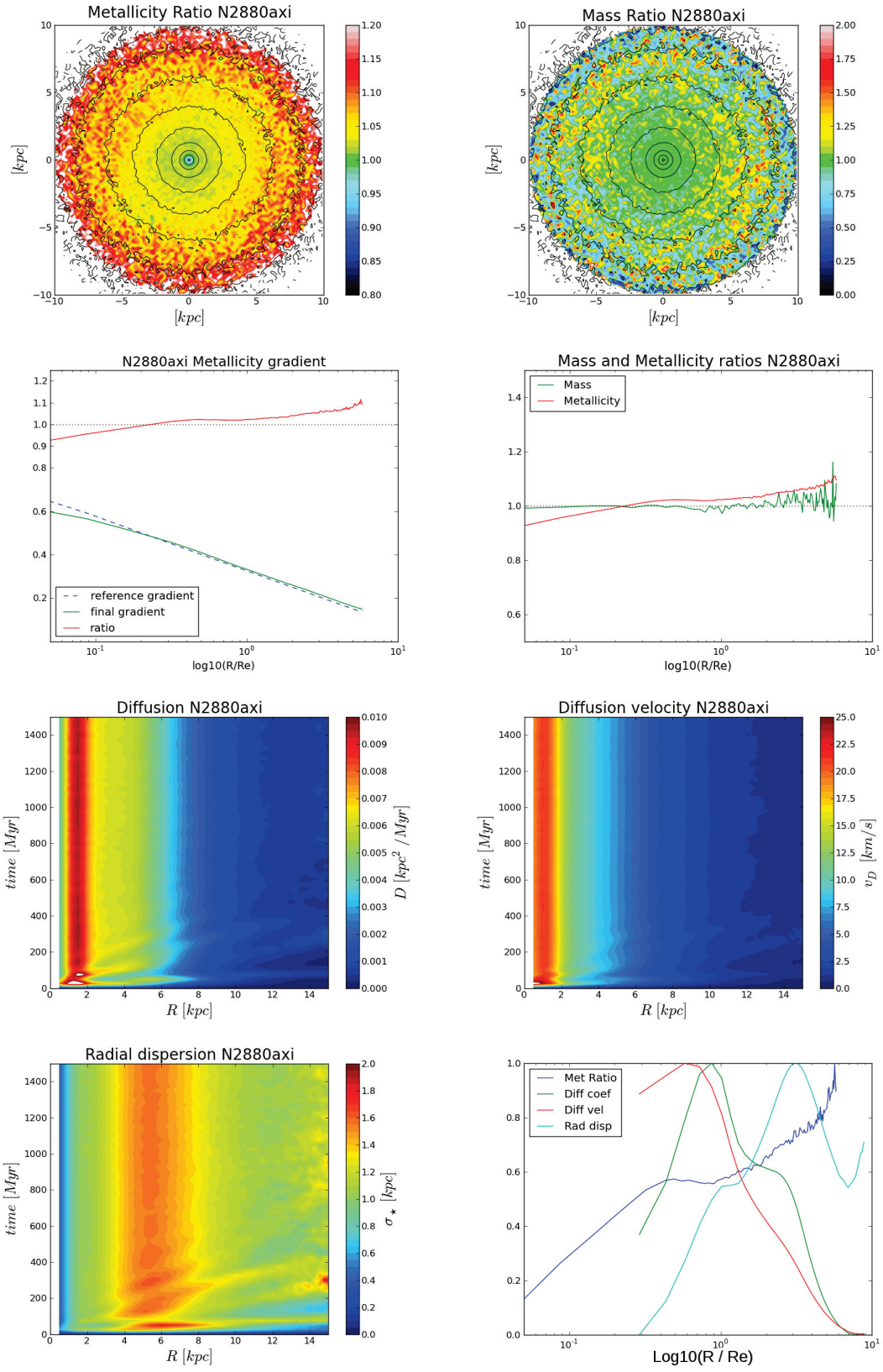

Figure C.1: N2880axi mass and metallicity redisitribution properties.

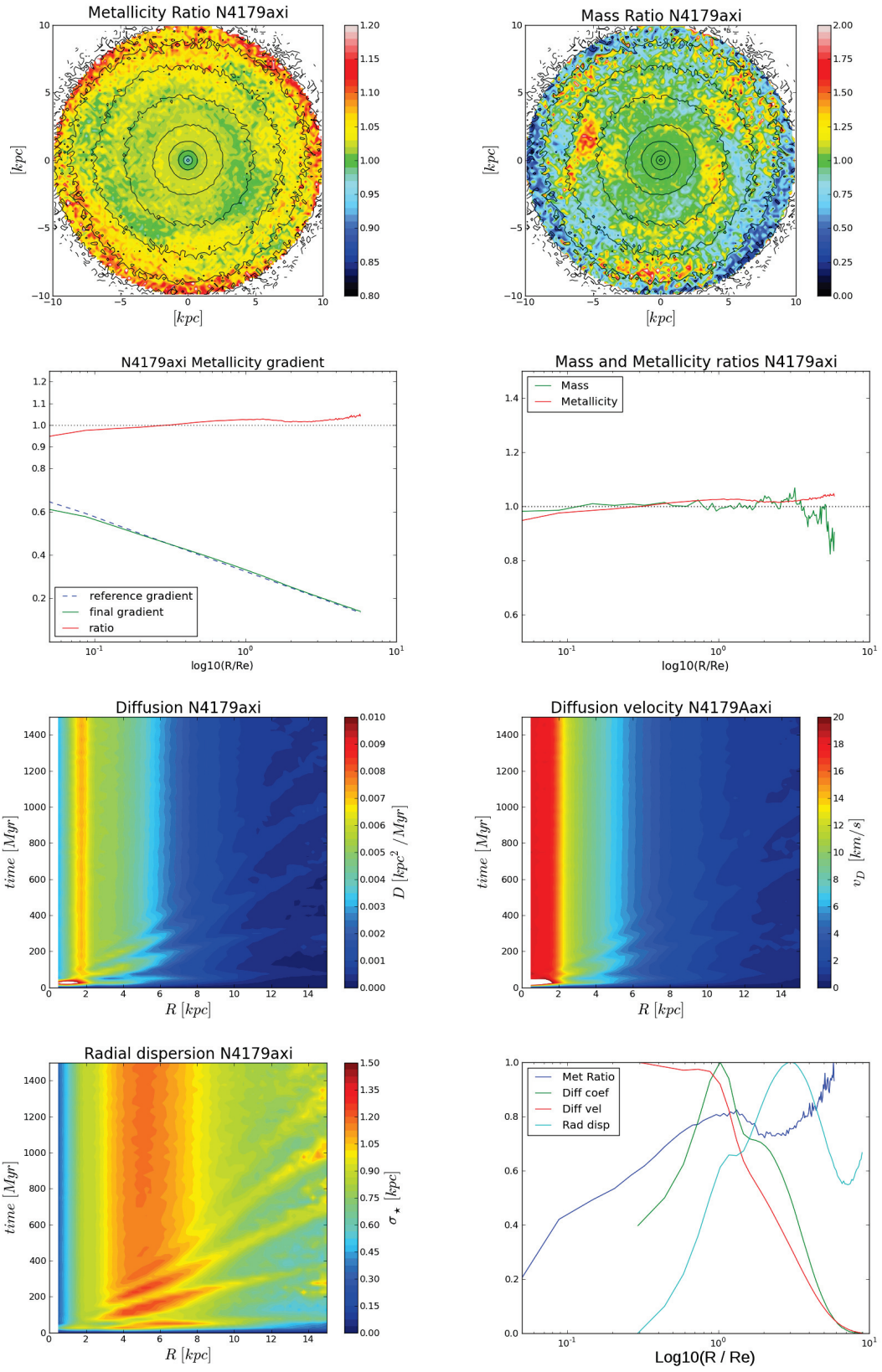

Figure C.2: Same as Fig C.1 for N4179axi.

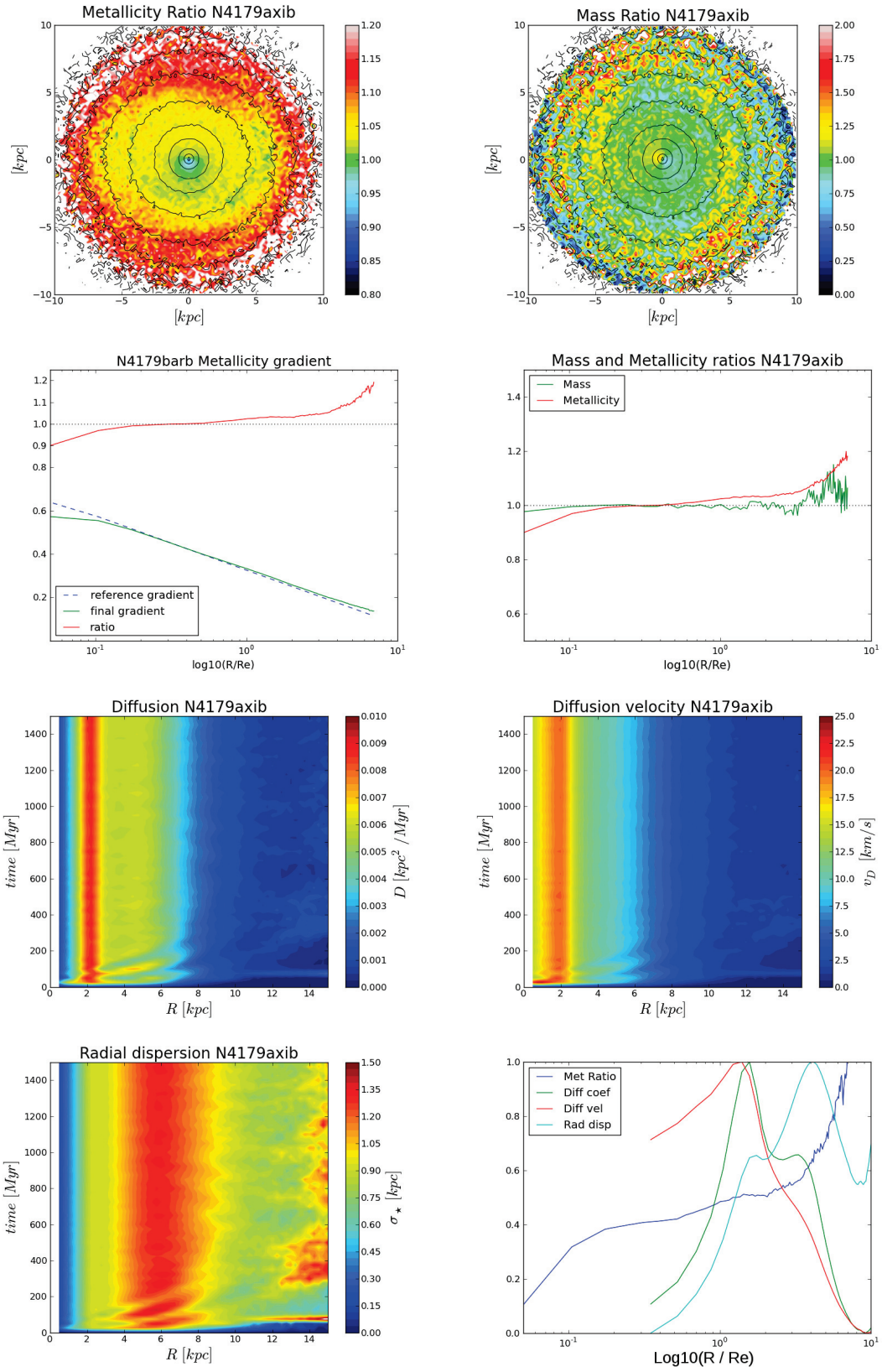

Figure C.3: Same as Fig C.1 for N4179axib.

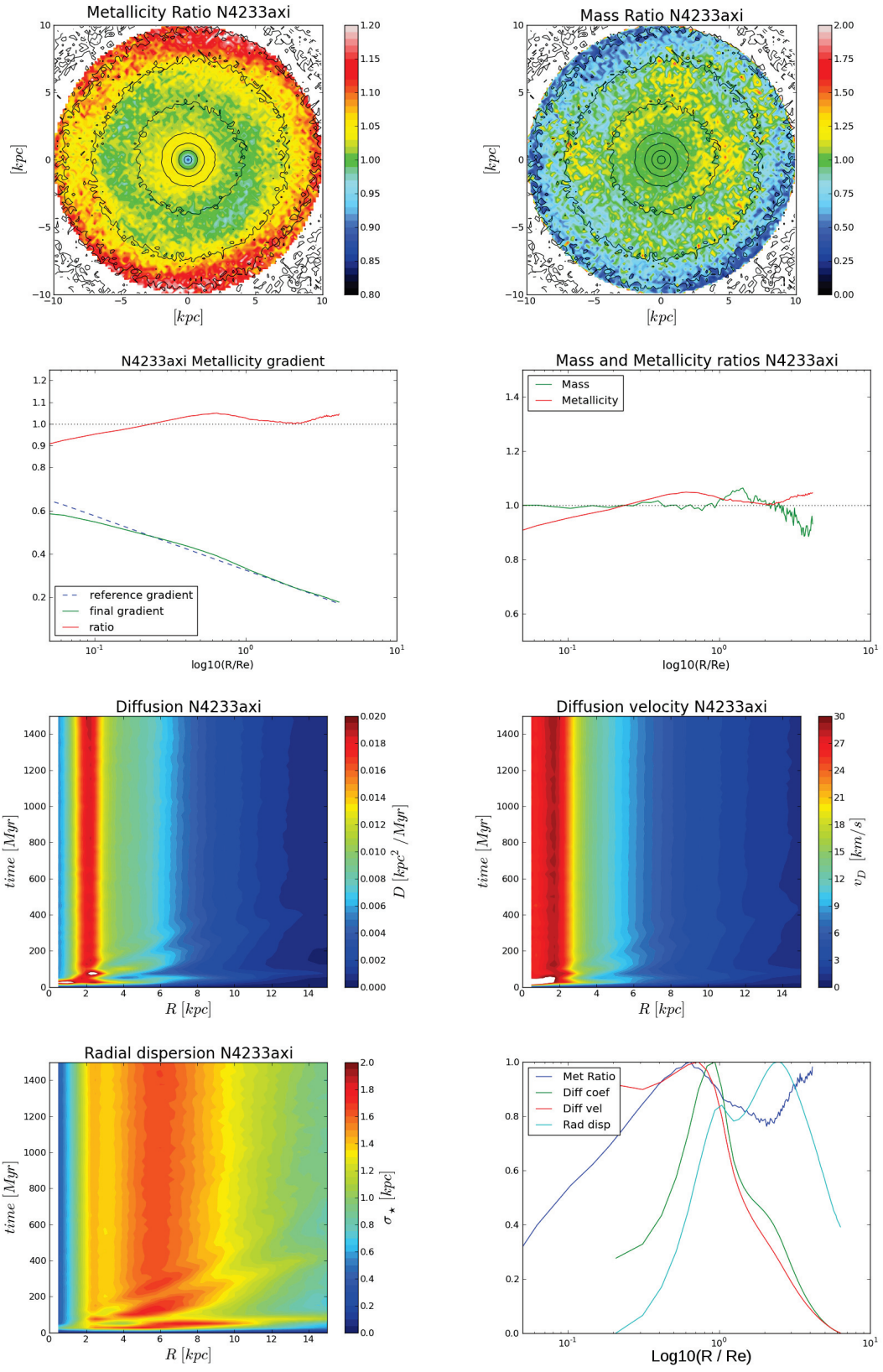

Figure C.4: Same as Fig C.1 for N4233axi.

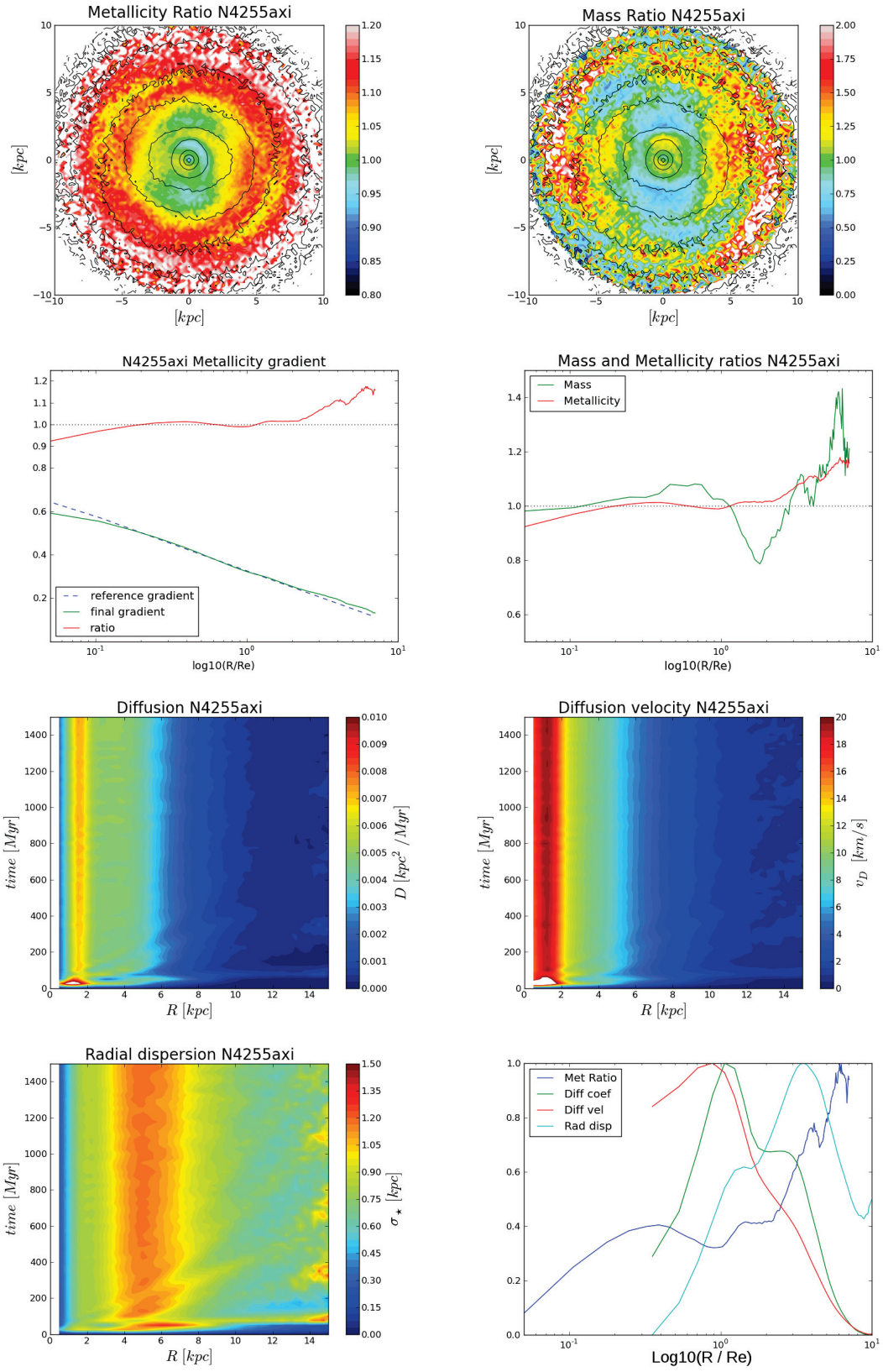

Figure C.5: Same as Fig C.1 for N4255axi.

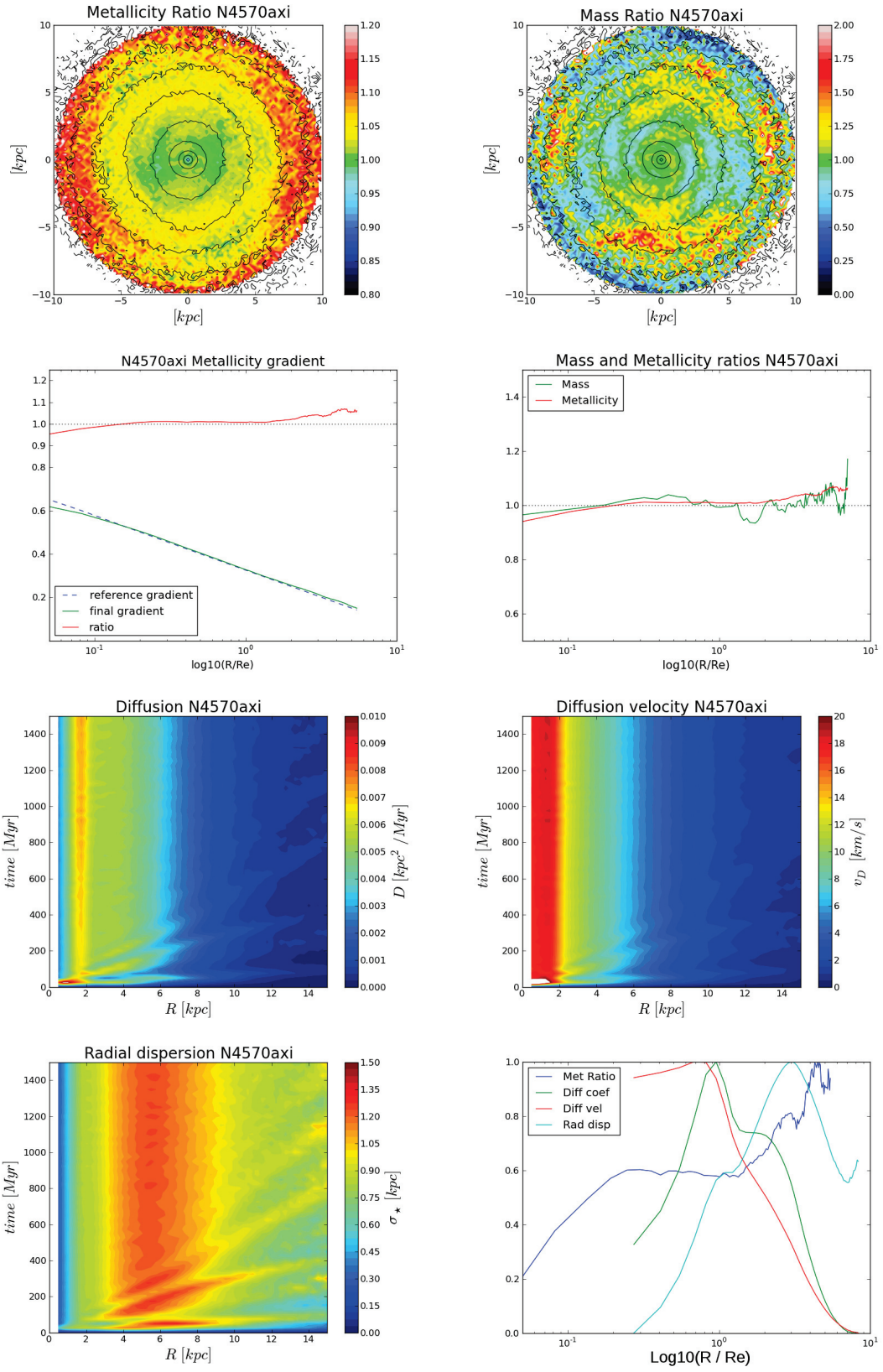

Figure C.6: Same as Fig C.1 for N4570axi.

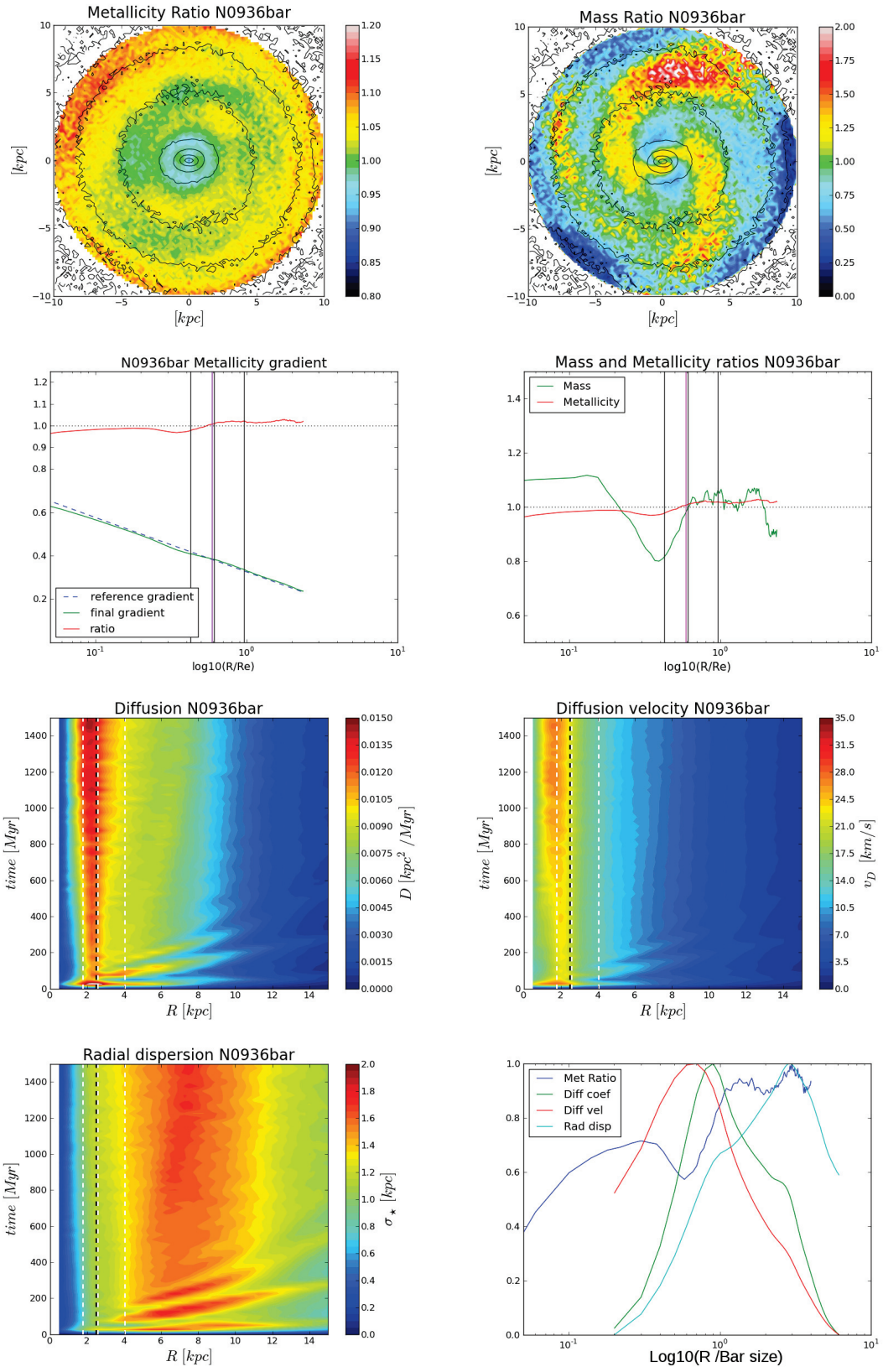

Figure C.7: Same as Fig C.1 for N0936bar.

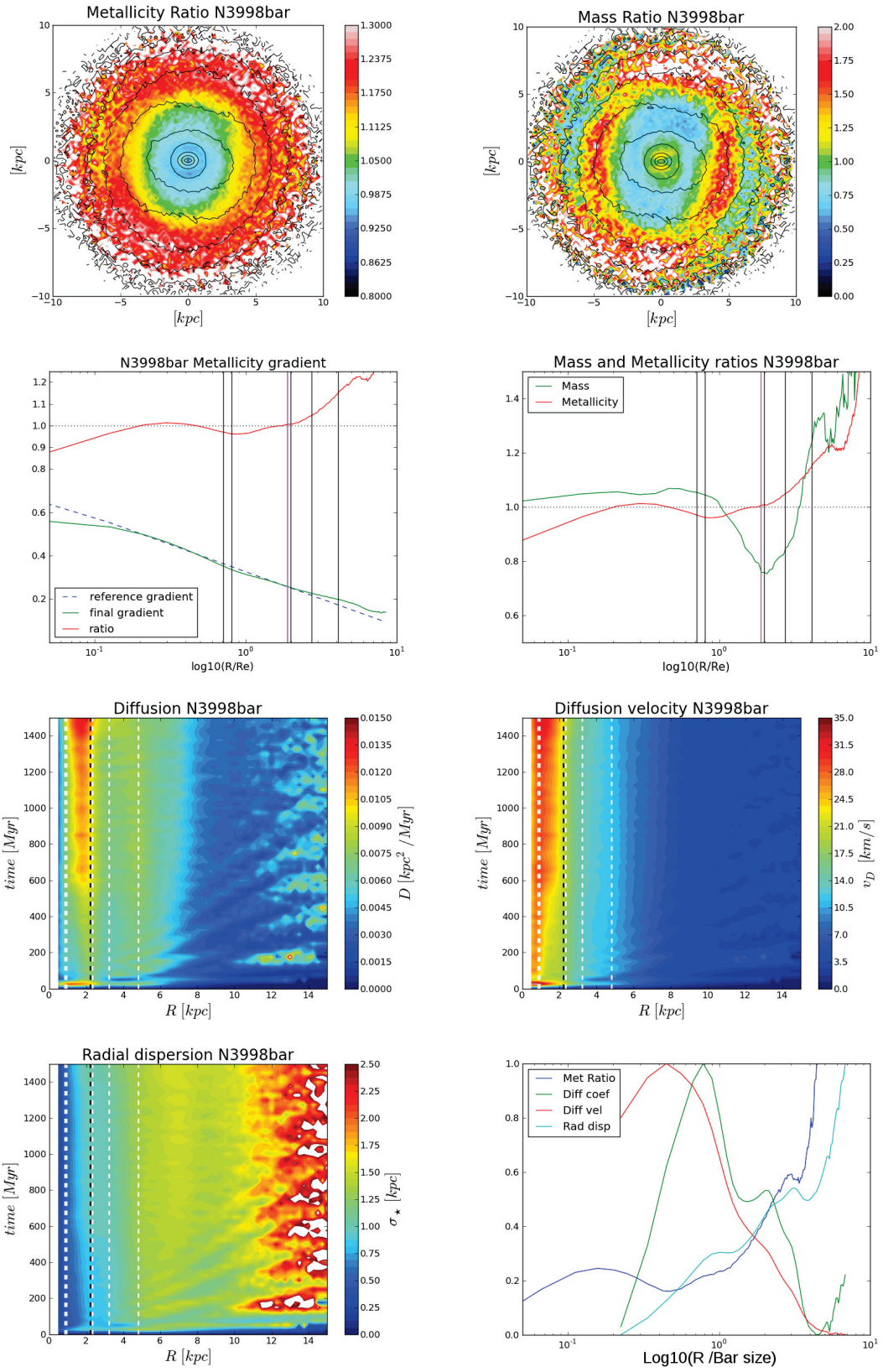

Figure C.8: Same as Fig C.1 for N3998bar.

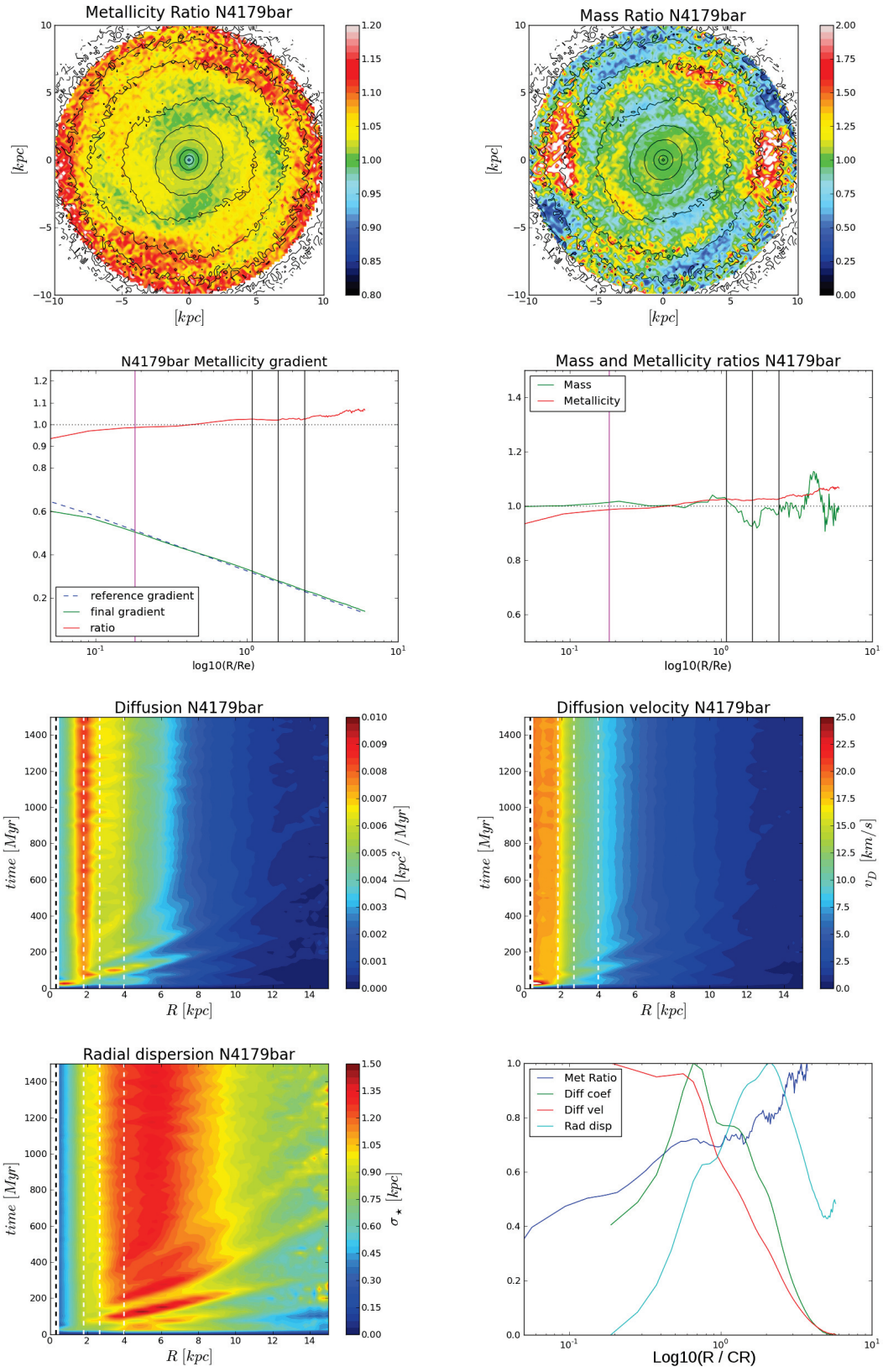

Figure C.9: Same as Fig C.1 for N4179bar. The bottom right figure is here normalised by the corotation radius just because the L_{bar} is too small to make the figure legible

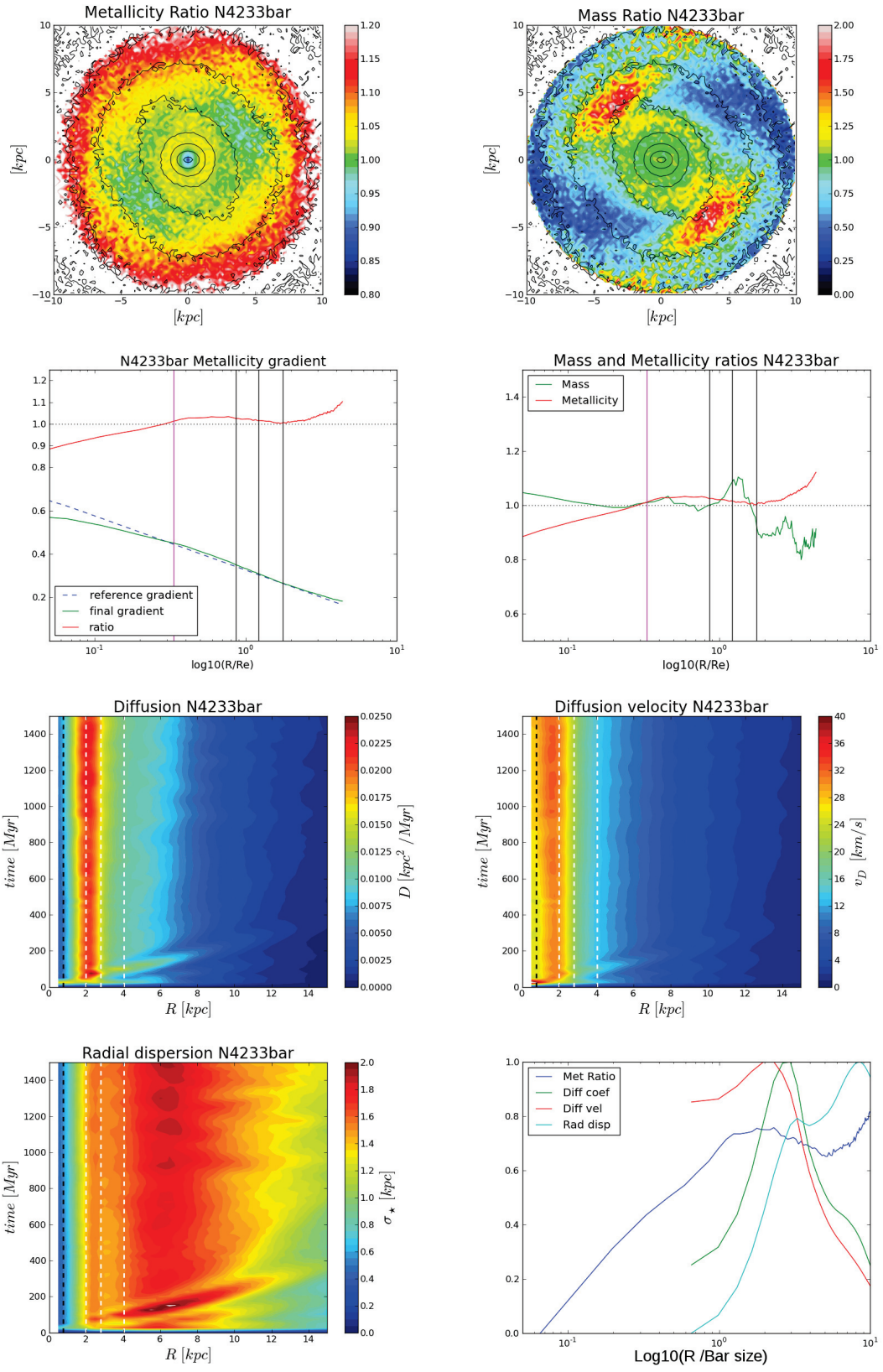

Figure C.10: Same as Fig C.1 for N4233bar.

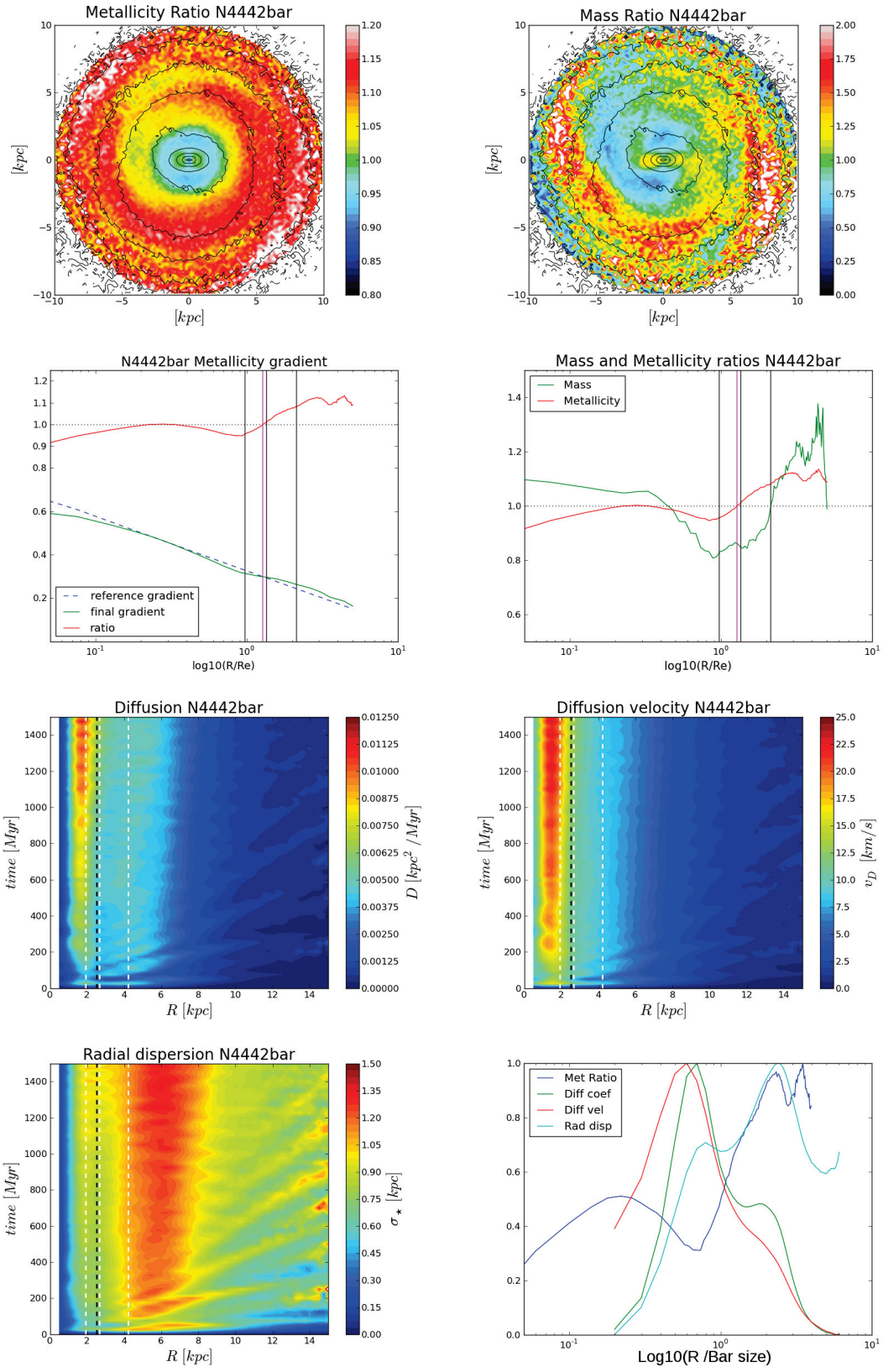

Figure C.11: Same as Fig C.1 for N4442bar.

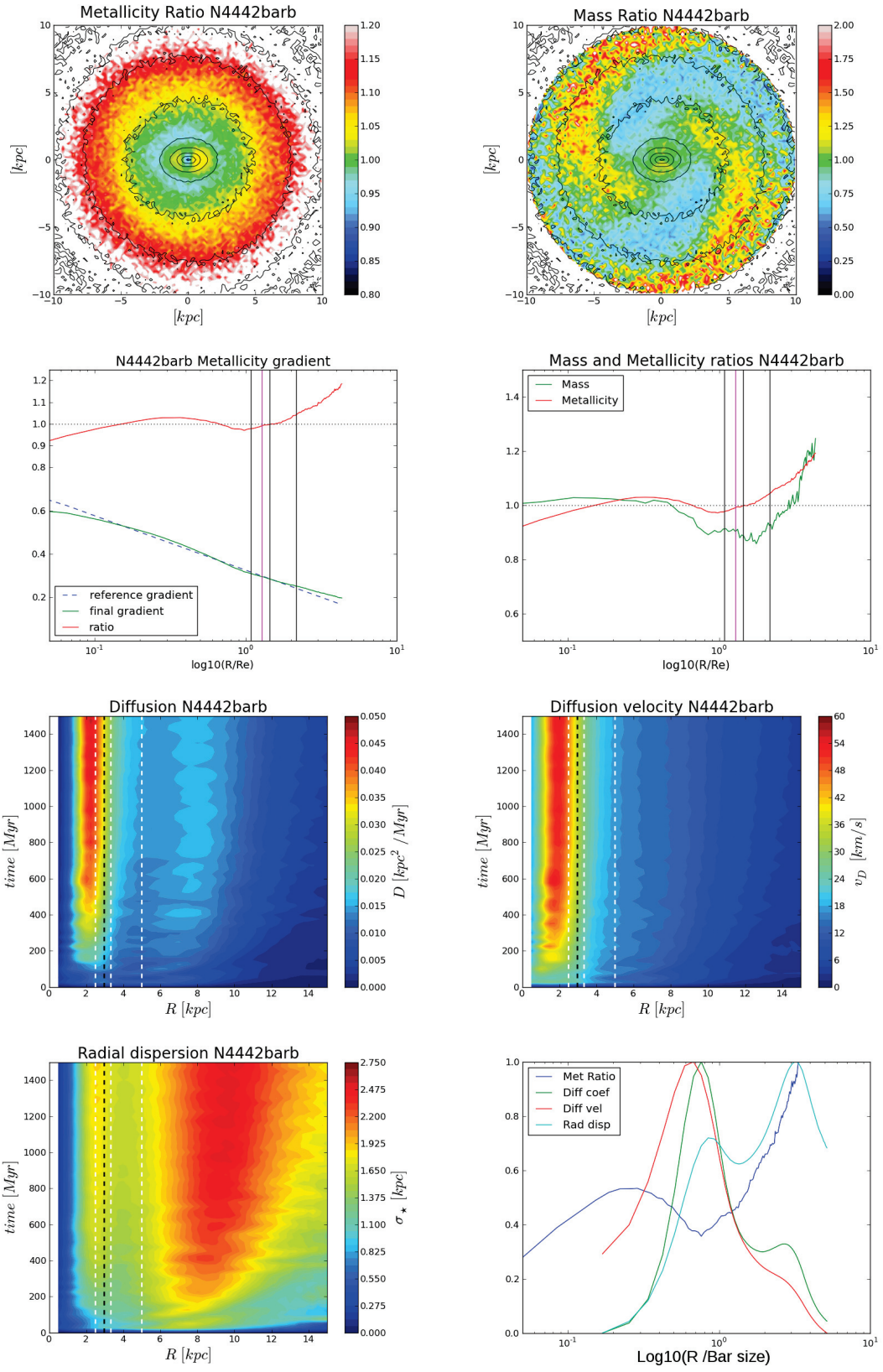

Figure C.12: Same as Fig C.1 for N4442barb.

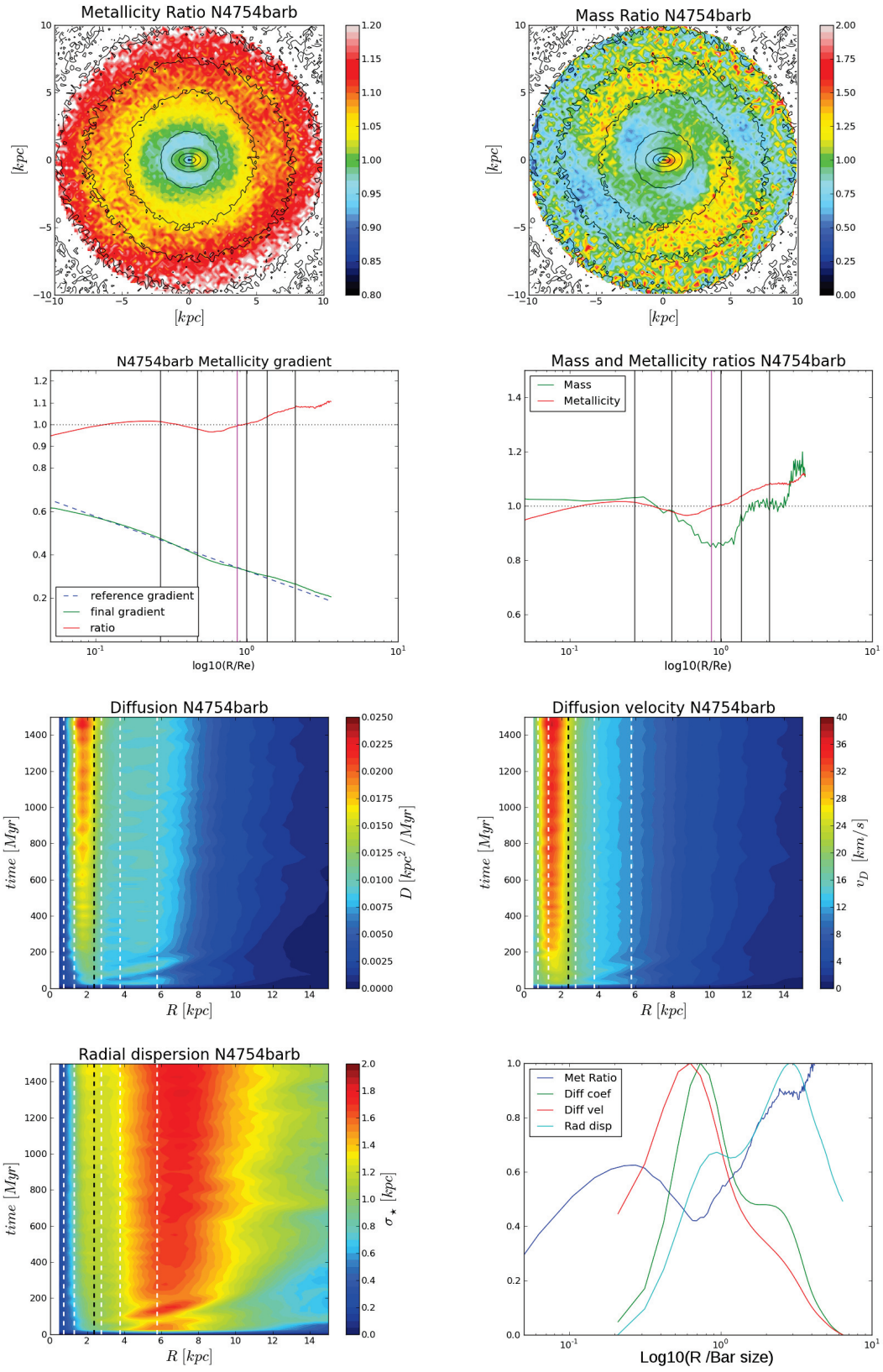

Figure C.13: Same as Fig C.1 for N4754barb.

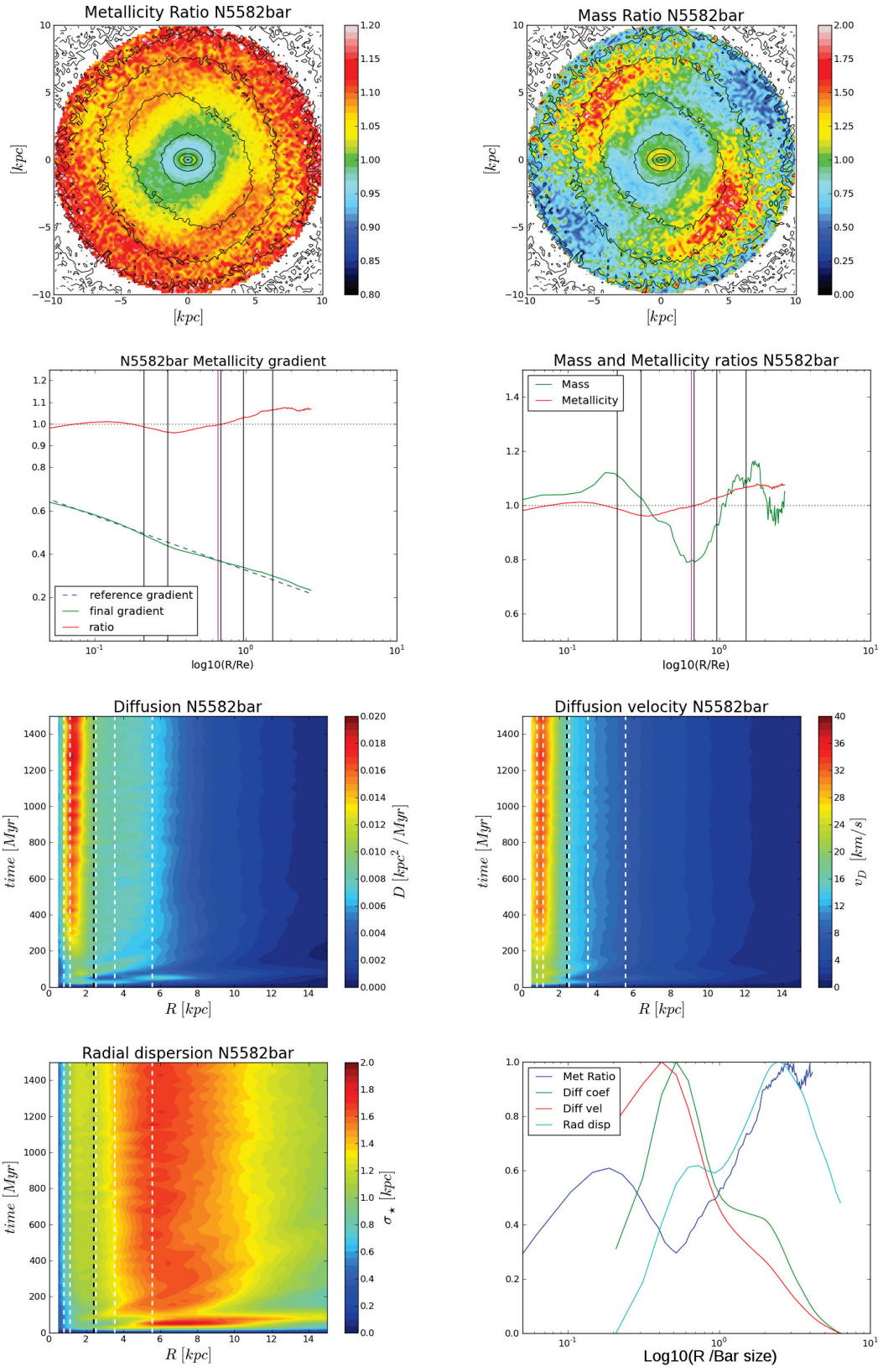

Figure C.14: Same as Fig C.1 for N5582bar.

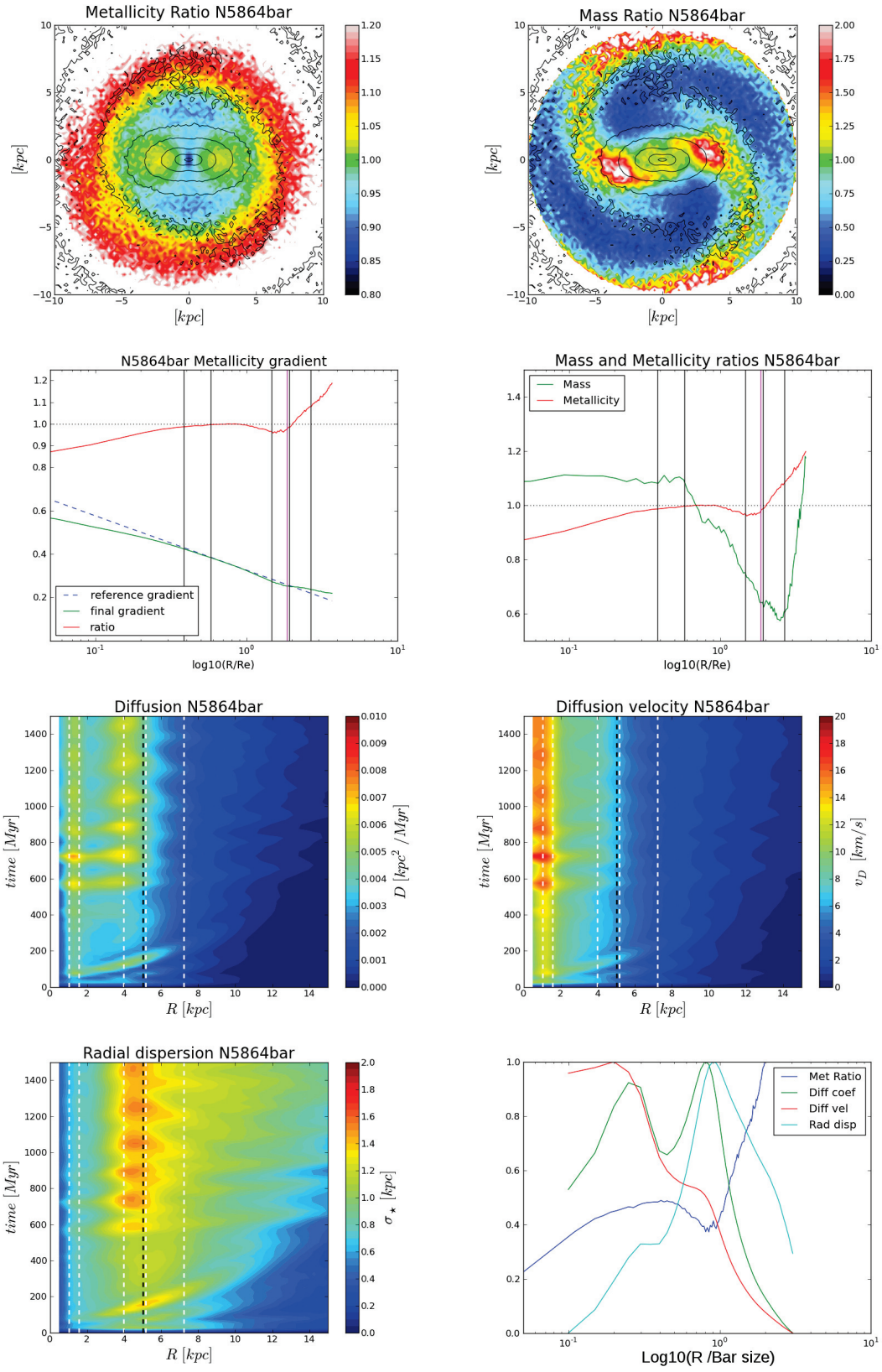

Figure C.15: Same as Fig C.1 for N5864bar.

Bibliography

Aarseth, S. J. 1963, MNRAS, 126, 223

Aguerri, J. A. L., Méndez-Abreu, J., & Corsini, E. M. 2009, A&A, 495, 491

Aoki, S., Noguchi, M., & Iye, M. 1979, PASJ, 31, 737

Athanassoula, E., & Sellwood, J. A. 1986, MNRAS, 221, 213

Athanassoula, E. 2003, MNRAS, 341, 1179

Bacon, R., Copin, Y., Monnet, G., et al. 2001, MNRAS, 326, 23

Baldry, I. K., Glazebrook, K., Brinkmann, J., et al. 2004, Apj, 600, 681

Baldry, I. K., Balogh, M. L., Bower, R., Glazebrook, K., & Nichol, R. C. 2004, The New Cosmology: Conference on Strings and Cosmology, 743, 106

Barazza, F. D., Jablonka, P., Desai, V., et al. 2009, A&A, 497, 713

Barnes, J., & Hut, P. 1986, Nature, 324, 446

Basu, S., Mouschovias, T. C., & Paleologou, E. V. 1997, Apj, 480, L55

Beck, R., Brandenburg, A., Moss, D., Shukurov, A., & Sokoloff, D. 1996, ARA&A, 34, 155

Beck, R., Ehle, M., Shoutenkov, V., Shukurov, A., & Sokoloff, D. 1999, Nature, 397, 324

Bell, E. F., Wolf, C., Meisenheimer, K., et al. 2004, Apj, 608, 752

Binney, J. J., Davies, R. L., & Illingworth, G. D. 1990, Apj, 361, 78

Binney, J. 2005, MNRAS, 363, 937

Binney, J., & Tremaine, S. 1987, Princeton, NJ, Princeton University Press, 1987, 747 p.

Binney, J., & Tremaine, S. 2008, Galactic Dynamics: Second Edition, by James Binney and Scott Tremaine. ISBN 978-0-691-13026-2 (HB). Published by Princeton University Press, Princeton, NJ USA, 2008.,

Binney, J. 2012, arXiv:1202.3403

Bois, M., Bournaud, F., Emsellem, E., et al. 2010, MNRAS, 406, 2405

Bois, M., Emsellem, E., Bournaud, F., et al. 2011, MNRAS, 416, 1654

Bode, P., & Ostriker, J. P. 2003, ApJS, 145, 1

Bournaud, F., & Combes, F. 2002, A&A, 392, 83

Bournaud, F., & Combes, F. 2003, A&A, 401, 817

Bournaud, F., Duc, P.-A., & Masset, F. 2003, A&A, 411, L469

Bournaud, F., Jog, C. J., & Combes, F. 2005, A&A, 437, 69

Bournaud, F., Combes, F., Jog, C. J., & Puerari, I. 2005, A&A, 438, 507

Bournaud, F., Combes, F., & Semelin, B. 2005, MNRAS, 364, L18

Bournaud, F., et al. 2007, Science, 316, 1166

Bournaud, F., Jog, C. J., & Combes, F. 2007, A&A, 476, 1179

Bournaud, F., Elmegreen, B. G., & Elmegreen, D. M. 2007, Apj, 670, 237

Brunetti, M., Chiappini, C., & Pfenniger, D. 2011, A&A, 534, A75

Buta, R., & Block, D. L. 2001, Apj, 550, 243

Cappellari, M. 2002, MNRAS, 333, 400

Cappellari, M., & Copin, Y. 2003, MNRAS, 342, 345

Cappellari, M., et al. 2006, MNRAS, 366, 1126

Cappellari, M., et al. 2007, MNRAS, 379, 418

Cappellari, M. 2008, MNRAS, 390, 71

Cappellari, M., et al. 2010, Highlights of Astronomy, 15, 81

Cappellari, M., Emsellem, E., Krajnović, D., et al. 2011, MNRAS, 413, 813

Cappellari, M., Emsellem, E., Krajnović, D., et al. 2011, MNRAS, 416, 1680

Combes, F., & Sanders, R. H. 1981, A&A, 96, 164

Combes, F., Debbasch, F., Friedli, D., & Pfenniger, D. 1990, A&A, 233, 82

Combes, F. 2008, Formation and Evolution of Galaxy Disks, 396, 325

Combes, F. 2011, IAU Symposium, 271, 119

Considère, S., Coziol, R., Contini, T., & Davoust, E. 2000, A&A, 356, 89

Contopoulos, G., & Papayannopoulos, T. 1980, A&A, 92, 33

Cox, T. J., Dutta, S. N., Di Matteo, T., et al. 2006, Apj, 650, 791

Cox, T. J., Jonsson, P., Primack, J. R., & Somerville, R. S. 2006, MNRAS, 373, 1013

Cretton, N., de Zeeuw, P. T., van der Marel, R. P., & Rix, H.-W. 1999, ApJS, 124, 383

Croton, D. J., Springel, V., White, S. D. M., et al. 2006, MNRAS, 365, 11

Debattista, V. P., & Shen, J. 2007, Apj, 654, L127

de Lorenzi, F., Debattista, V. P., Gerhard, O., & Sambhus, N. 2007, MNRAS, 376, 71

Dehnen, W., & Read, J. I. 2011, European Physical Journal Plus, 126, 55

de Vaucouleurs, G. 1959, Handbuch der Physik, 53, 311

de Zeeuw, P. T., Bureau, M., Emsellem, E., et al. 2002, MNRAS, 329, 513

Dubinski, J., Berentzen, I., & Shlosman, I. 2009, Apj, 697, 293

Dubinski, J., & Chakrabarty, D. 2009, Apj, 703, 2068

Duc, P.-A., Bournaud, F., & Masset, F. 2004, A&A, 427, 803

Duc, P.-A., & Bournaud, F. 2008, Apj, 673, 787

Efstathiou, G., Davis, M., White, S. D. M., & Frenk, C. S. 1985, ApJS, 57, 241

Ellison, S. L., Nair, P., Patton, D. R., et al. 2011, MNRAS, 416, 2182

Elmegreen, B. G. 2011, EAS Publications Series, 51, 3

Elmegreen, B. G. 2011, EAS Publications Series, 51, 19

Elmegreen, B. G. 2011, EAS Publications Series, 51, 31

Elmegreen, B. G. 2011, EAS Publications Series, 51, 45

Elmegreen, B. G. 2011, EAS Publications Series, 51, 59

Emsellem, E., Monnet, G., & Bacon, R. 1994a, A&A, 285, 723

Emsellem, E., Monnet, G., Bacon, R., & Nieto, J.-L. 1994b, A&A, 285, 739

Emsellem, E., et al. 2004, MNRAS, 352, 721

Emsellem, E., Fathi, K., Wozniak, H., et al. 2006, MNRAS, 365, 367

Emsellem, E., Cappellari, M., Krajnović, D., et al. 2007, MNRAS, 379, 401

Emsellem, E., Cappellari, M., Krajnović, D., et al. 2011, MNRAS, 414, 888

Erwin, P. 2011, Memorie della Societa Astronomica Italiana Supplementi, 18, 145

Eskridge, P. B., Frogel, J. A., Pogge, R. W., et al. 2000, Aj, 119, 536

Faber, S. M., Willmer, C. N. A., Wolf, C., et al. 2007, Apj, 665, 265

Friedli, D., Benz, W., & Kennicutt, R. 1994, Apj, 430, L105

Friedli, D., & Benz, W. 1995, A&A, 301, 649

Friedli, D. 1996, A&A, 312, 761

Friedli, D., Wozniak, H., Rieke, M., Martinet, L., & Bratschi, P. 1996, A&AS, 118, 461

Gebhardt, K., et al. 2003, Apj, 583, 92

Gerhard, O. 1996, Spiral Galaxies in the Near-IR, 138

Gingold, R. A., & Monaghan, J. J. 1977, MNRAS, 181, 375

Häfner, R., Evans, N. W., Dehnen, W., & Binney, J. 2000, MNRAS, 314, 433

Hao, L., Jogee, S., Barazza, F. D., Marinova, I., & Shen, J. 2009, Galaxy Evolution: Emerging Insights and Future Challenges, 419, 402

Hawarden, T. G., Huang, J. H., & Gu, Q. S. 1996, IAU Colloq. 157: Barred Galaxies, 91, 54

Hernandez, O., Wozniak, H., Carignan, C., et al. 2005, Apj, 632, 253

Hernquist, L. 1990, Apj, 356, 359

Herschel, W. 1786, Royal Society of London Philosophical Transactions Series I, 76, 457

Herschel, W. 1789, Royal Society of London Philosophical Transactions Series I, 79, 212

Herschel, W. 1802, Royal Society of London Philosophical Transactions Series I, 92, 477

Hockney, R. W., & Eastwood, J. W. 1981, Computer Simulation Using Particles, New York: McGraw-Hill, 1981,

Hohl, F. 1971, Apj, 168, 343

Holmberg, E. 1941, Apj, 94, 385

Hopkins, P. F., Hernquist, L., Cox, T. J., et al. 2006, ApJS, 163, 1

Hopkins, P. F., Cox, T. J., Younger, J. D., & Hernquist, L. 2009, Apj, 691, 1168

Huang, J. H., Gu, Q. S., Su, H. J., et al. 1996, A&A, 313, 13

Hubble, E. P. 1926, Apj, 64, 321

Hubble, E. P. 1936, Realm of the Nebulae, by E.P. Hubble. New Haven: Yale University Press, 1936.

Hummel, E., van der Hulst, J. M., Kennicutt, R. C., & Keel, W. C. 1990, A&A, 236, 333

Hunt, L. K., & Malkan, M. A. 1999, Apj, 516, 660

Hut, P., Makino, J., & McMillan, S. 1995, Apj, 443, L93

Jalali, M. A. 2007, Apj, 669, 218

Jeans, J. H. 1922, MNRAS, 82, 122

Jogee, S., Barazza, F. D., Rix, H.-W., et al. 2004, Apj, 615, L105

Jogee, S., Scoville, N., & Kenney, J. D. P. 2005, Apj, 630, 837

Jungwiert, B., Combes, F., & Axon, D. J. 1997, A&AS, 125, 479

Jungwiert, B., Combes, F., & Palouš, J. 2001, A&A, 376, 85

Kalnajs, A. J. 1978, Structure and Properties of Nearby Galaxies, 77, 113

Kennicutt, R. C., Jr. 1998, Apj, 498, 541

Kereš, D., Katz, N., Fardal, M., Davé, R., & Weinberg, D. H. 2009, MNRAS, 395, 160

Khoperskov, A. V., Just, A., Korchagin, V. I., & Jalali, M. A. 2007, A&A, 473, 31

Kim, W.-T., & Ostriker, E. C. 2002, Apj, 570, 132

Knapen, J. H. 2010, Galaxies and their Masks, 201

Korchagin, V., Orlova, N., Kikuchi, N., Miyama, S. M., & Moiseev, A. V. 2005, arXiv:astro-ph/0509708

Kormendy, J., & Bender, R. 1999, Apj, 522, 772

Kormendy, J., & Kennicutt, R. C., Jr. 2004, ARA&A, 42, 603

Krajnović, D., Cappellari, M., Emsellem, E., McDermid, R. M., & de Zeeuw, P. T. 2005, MNRAS, 357, 1113

Krajnović, D., Emsellem, E., Cappellari, M., et al. 2011, MNRAS, 414, 2923

Kuntschner, H., Emsellem, E., Bacon, R., et al. 2010, MNRAS, 408, 97

Laine, S., Shlosman, I., Knapen, J. H., & Peletier, R. F. 2002, Apj, 567, 97

Laurikainen, E., Salo, H., Buta, R., & Knapen, J. H. 2009, Apj, 692, L34

Li, C., Gadotti, D. A., Mao, S., & Kauffmann, G. 2009, MNRAS, 397, 726

Lin, C. C., & Shu, F. H. 1964, Apj, 140, 646

Lin, C. C., & Shu, F. H. 1966, Proceedings of the National Academy of Science, 55, 229

Lucy, L. B. 1977, Aj, 82, 1013

Lynden-Bell, D. 1979, MNRAS, 187, 101

Lynden-Bell, D. 1996, Lecture Notes in Physics, Berlin Springer Verlag, 474, 7

Machado, R. E. G., & Athanassoula, E. 2010, MNRAS, 406, 2386

Marinova, I., & Jogee, S. 2007, Apj, 659, 1176

Martig, M., Bournaud, F., & Teyssier, R. 2009, IAU Symposium, 254, 429

Martig, M., Bournaud, F., Teyssier, R., & Dekel, A. 2009, Apj, 707, 250

Martin, P., & Friedli, D. 1997, A&A, 326, 449

Menéndez-Delmestre, K., Sheth, K., Schinnerer, E., Jarrett, T. H., & Scoville, N. Z. 2007, Apj, 657, 790

Michel-Dansac, L., & Wozniak, H. 2004, A&A, 421, 863

Michel-Dansac, L. & Wozniak, H., 2006, A&A, 452, 97

Miller, R. H., Prendergast, K. H., & Quirk, W. J. 1970, Apj, 161, 903

Monaghan, J. J., & Lattanzio, J. C. 1985, A&A, 149, 135

Monaghan, J. J. 1992, ARA&A, 30, 543

Monaghan, J. J. 2005, Reports on Progress in Physics, 68, 1703

Monnet, G., Bacon, R., & Emsellem, E. 1992, A&A, 253, 366

Moster, B. P., Macciò, A. V., Somerville, R. S., Johansson, P. H., & Naab, T. 2010, MNRAS, 403, 1009

Naab, T., & Burkert, A. 2003, Apj, 597, 893

Naab, T., Jesseit, R., & Burkert, A. 2006, MNRAS, 372, 839

Naab, T., Johansson, P. H., Ostriker, J. P., & Efstathiou, G. 2007, Apj, 658, 710

Navarro, J. F., Ludlow, A., Springel, V., et al. 2010, MNRAS, 402, 21

Oey, M. S., & Kennicutt, R. C., Jr. 1993, Apj, 411, 137

Pasha, I. I. 2004, arXiv:astro-ph/0406142

Pasha, I. I. 2004, arXiv:astro-ph/0406143

Patsis, P. A., Skokos, C., & Athanassoula, E. 2002, MNRAS, 337, 578

Pérez, I., Sánchez-Blázquez, P., & Zurita, A. 2009, A&A, 495, 775

Pérez, I., & Sánchez-Blázquez, P. 2011, A&A, 529, A64

Pfenniger, D. 1984, A&A, 134, 373

Pfenniger, D. 1986, A&A, 165, 74

Pfenniger, D., & Friedli, D. 1991, A&A, 252, 75

Pfenniger, D., & Friedli, D. 1993, A&A, 270, 561

Pichon, C., & Cannon, R. C. 1997, MNRAS, 291, 616

Polyachenko, E. V. 2005, MNRAS, 357, 559

Poveda, A. 1958, Boletin de los Observatorios Tonantzintla y Tacubaya, 2, 3

Rubin, V. C., Ford, W. K. J., & . Thonnard, N. 1980, Apj, 238, 471

Rybicki, G. B. 1987, Structure and Dynamics of Elliptical Galaxies, 127, 397

Sánchez-Blázquez, P., Ocvirk, P., Gibson, B. K., Pérez, I., & Peletier, R. F. 2011, MNRAS, 415, 709

Sandage, A. 1961, Washington: Carnegie Institution, 1961,

Sawamura, M. 1988, PASJ, 40, 279

Schmidt, M. 1959, Apj, 129, 243

Schwarz, M. P. 1981, Apj, 247, 77

Schwarzschild, M. 1979, Apj, 232, 236

Scott, N., et al. 2009, MNRAS, 398, 1835

Sellwood, J. A. 1981, A&A, 99, 362

Sellwood, J. A., & Wilkinson, A. 1993, Reports on Progress in Physics, 56, 173

Sellwood, J. A., & Binney, J. J. 2002, MNRAS, 336, 785

Sellwood, J. A. 2010, arXiv:1006.4855

Skokos, C., Patsis, P. A., & Athanassoula, E. 2002, MNRAS, 333, 847

Sparke, L. S., & Sellwood, J. A. 1987, MNRAS, 225, 653

Spitzer, L., Jr. 1969, Apj, 158, L139

Springel, V. 2005, MNRAS, 364, 1105

Springel, V., White, S. D. M., Jenkins, A., et al. 2005, Nature, 435, 629

Strateva, I., Ivezić, Ž., Knapp, G. R., et al. 2001, Aj, 122, 1861

Teyssier, R. 2002, A&A, 385, 337

Teyssier, R., Pires, S., Prunet, S., et al. 2009, A&A, 497, 335

Thomas, J., Saglia, R. P., Bender, R., Thomas, D., Gebhardt, K., Magorrian, J., & Richstone, D. 2004, MNRAS, 353, 391

Thomas, J., Jesseit, R., Naab, T., Saglia, R. P., Burkert, A., & Bender, R. 2007, MNRAS, 381, 1672

Thomas, J., et al. 2009, MNRAS, 393, 641

Toomre, A. 1981, Structure and Evolution of Normal Galaxies, 111

Tremaine, S., & Weinberg, M. D. 1984, Apj, 282, L5

Valluri, M., Merritt, D., & Emsellem, E. 2004, Apj, 602, 66

van den Bergh, S. 1960, Apj, 131, 215

van den Bosch, R. C. E., van de Ven, G., Verolme, E. K., Cappellari, M., & de Zeeuw, P. T. 2008, MNRAS, 385, 647

van den Bosch, R. C. E., & van de Ven, G. 2009, MNRAS, 398, 1117

van der Marel, R. P., Binney, J., & Davies, R. L. 1990, MNRAS, 245, 582

van der Marel, R. P., Cretton, N., de Zeeuw, P. T., & Rix, H.-W. 1998, Aapj, 493, 613

Vauterin, P., & Dejonghe, H. 1996, A&A, 313, 465

Vila-Costas, M. B., & Edmunds, M. G. 1992, MNRAS, 259, 121

Villalobos, Á., & Helmi, A. 2008, MNRAS, 391, 1806

von Hoerner, S. 1960, ZAp, 50, 184

Weijmans, A.-M., Krajnović, D., van de Ven, G., et al. 2008, MNRAS, 383, 1343

Williams, M. J., Zamojski, M. A., Bureau, M., et al. 2011, MNRAS, 414, 2163

Wozniak, H., Friedli, D., Martinet, L., Martin, P., & Bratschi, P. 1995, A&AS, 111, 115

Wozniak, H., Combes, F., Emsellem, E., & Friedli, D. 2003, A&A, 409, 469

Wozniak, H., & Champavert, N. 2006, MNRAS, 369, 853

Wozniak, H. 2007, A&A, 465, L1

Wozniak, H., & Michel-Dansac, L. 2007, IAU Symposium, 241, 531

Wozniak, H., & Michel-Dansac, L. 2009, A&A, 494, 11

Zang, T. A., & Hohl, F. 1978, Apj, 226, 521

Zhao, H. 1996, MNRAS, 283, 149